République Algérienne Démocratique et Populaire
وزارة التعليم العالي و البحث العلمي
Ministère de l'enseignement supérieur et de la recherche scientifique

Université Mohamed Khider – Biskra
Faculté des Sciences et de la technologie
Département : Génie Electrique
Ref :……

جامعة محمد خيضر بسكرة
كلية العلوم و التكنولوجيا
قسم :الهندسة الكهربائية
المرجع : .....

Thèse présentée en vue de l'obtention

du diplôme de

Doctorat LMD en Electrotechnique

Spécialité (Option) : **Contrôle et Diagnostic des Systèmes Electriques**

Intitulé :

Commande Sans Capteur de Vitesse du Moteur Synchrone à Reluctance

Présentée par :

Mohamed Essalih Boussouar

Devant le jury composé de :

SAHRAOUI Mohamed	**Professeur**	**Président**	**Université de Biskra**
YAHIA Khlaed	**Professeur**	**Rapporteur**	**Université de Biskra**
CARDOSO A.J.Marques	**Professeur**	**Co-Rapporteur**	**Université de Beira Interior ,Portugal**
HAMMOUDI Mohamed Yacine	**Professeur**	**Examinateur**	**Université de Biskra**
ACHOUR Djaloul	**MCA**	**Examinateur**	**Université de Chlef**

Soutenue le : 28/10/2024

République Algérienne Démocratique et Populaire
وزارة التعليم العالي و البحث العلمي
Ministère de l'enseignement supérieur et de la recherche scientifique

Université Mohamed Khider – Biskra
Faculté des Sciences et de la technologie
Département : Génie Electrique
Ref :……

جامعة محمد خيضر بسكرة
كلية العلوم و التكنولوجيا
قسم :الهندسة الكهربائية
المرجع : .....

Thèse présentée en vue de l'obtention

du diplôme de

Doctorat LMD en Electrotechnique

Spécialité (Option) : **Contrôle et Diagnostic des Systèmes Electriques**

Title:

Speed Sensorless Control of Synchronous Reluctance Motor

Presented by:

Mohamed Essalih BOUSSOUAR

Board of Examiners:

SAHRAOUI Mohamed	**Professor**	**Chairman**	**University of Biskra**
YAHIA Khlaed	**Professor**	**Supervisor**	**University of Biskra**
CARDOSO A.J.Marques	**Professor**	**Co-Supervisor**	**University of Beira Interior ,Portugal**
HAMMOUDI Mohamed Yacine	**Professor**	**Examiner**	**University of Biskra**
ACHOUR Djaloul	**MCA**	**Examiner**	**University of Chlef**

Thesis defended in 28/10/2024

Acknowledgement

First of all, praise is to Almighty God who has given me the strength, faith, health, courage, guidance at every step, and patience to complete this present thesis. It has been a long journey finishing this thesis, and it would have been much more difficult without the help of many excellent people.

I would like to express my sincerest gratitude to my supervisor ***Pr. Khaled Yahia***, and co-supervisor ***Pr. Antonio J. Marques Cardoso***, for their continuous support and critical guidance throughout my PhD period. Without their careful reading and constructive comments, the completion of this work would not have been possible.

Next, I would like to thank the director of the Laboratory of Energetic Systems Modeling (LMSE) ***Pr. Boumahraz Mohamed***, for the best conditions he has reserved for us to finish this work and for having accepted the presidency of the jury.

Furthermore, my appreciation and thanks are extended to the rest of my thesis committee Pr **.** ***Mohamed Sahraoui ,Pr. Hammoudi M.Y , Dr.Achour Djaloul*** , who honored me with their acceptance to examine and read my thesis.

My greatest gratitude goes to ***Dr. Chelihi Abdelghani*** at the University of Constantine 1, for his valuable advice and contributions to the publication of my articles.

Obviously, I cannot close these lines without addressing my thanks to all the Electrical Engineering department staff and my colleagues.

Finally, I thank my parents, my wife, my sisters and my friends for their endless love and support that have made the hard times so much easier, as well as to everyone who helped me without exception, with a smile, with encouragement, with information, to everyone who had confidence in me and this gave me the energy to assume myself and succeed.

Dedication

This thesis is dedicated to the wonderful persons who deserve a lot of love and respect:

To my dear parents,

To my wife, my sons D & S,

To my sisters,

To all my teachers and administrative staff,

To all those who supported me and helped me to get my PhD without hesitation,

Thank you very much indeed

ملخص

يساهم البحث المقدم في هذه الأطروحة، في التحكم وتحسين الأداء لآلة الممانعة المتزامنة (Syn-RM) ، وهي تكنولوجيا واعدة وغير معروفة بشكل واسع. تتمحور هذه الرسالة حول أربعة جوانب رئيسية. أولاً، تقدم ملخصًا للأبحاث المنجزة حول تقنيات التحكم وتقدير السرعة لهذه الآلة. ثانيًا، تقدم شرحا شاملاً لنموذجها الديناميكي، ويتم دراسة أداء التحكم من خلال المحاكاة باستخدام استراتيجيات التحكم المثبتة. ثالثًا، تتناول التحكم في السرعة بدون استخدام مستشعر، باستخدام أساليب المراقبة التي تدمج نموذج Syn-RM الديناميكي مع تقنية التقدير. أخيرًا، تركز الرسالة على تقنية التحكم المتقدمة من خلال تنفيذ تقنية التحكم الحالي التنبئي بدون نموذج (MF-PCC).

الكلمات المفتاحية: آلة الممانعة المتزامنة، التحكم المباشر للعزم، تموج العزم، تحكم بدون حساس، التحكم التنبئي في التيار، التحكم بدون نموذج، التقدير عن طريق تأخر الزمن

Abstract

The research presented in this thesis, contribute to the Synchronous Reluctance Machine (SynRM) control and performance improvement, a lesser-known but promising technology. This thesis is structured around four main aspects. First, it gives a literature review about the control and speed estimation techniques of this machine. Second, it provides a comprehensive exploration of its dynamic model, and furthermore the control performances are investigated through simulations using established control strategies. Third it delves into sensorless speed control, employing observation method incorporating the SynRM dynamic model for estimation. Lastly, the thesis focus on an advanced control technique through the implementation of Model Free Predictive Current Control (MF-PCC).

Key words: SynRM, DTC, Torque ripple, Sensorless control, PCC, MFC, TDE

Résumé

Les recherches présentées dans cette thèse contribuent au contrôle et à l'amélioration des performances de la machine à réluctance synchrone (SynRM), une technologie moins connue mais prometteuse. Cette thèse est structurée autour de quatre aspects principaux. Tout d'abord, elle propose un résumé de la littérature sur les techniques de commande et d'estimation de vitesse de cette machine. Ensuite, elle offre une exploration approfondie de son modèle dynamique, et les performances de contrôle sont étudiées à travers des simulations utilisant des stratégies de contrôle établies. En troisième lieu, elle se penche sur la commande de vitesse sans capteur, en utilisant une méthode d'observation incorporant le modèle dynamique de Syn-RM pour l'estimation. Enfin, la thèse se concentre sur une technique de commande avancée grâce à la mise en œuvre de la commande prédictive de courant sans modèle (MF-PCC).

Mots clés: Syn-RM, DTC, Ondulation de couple, Commande sans capteur, PCC, MFC, TDE

Table of Contents

List of figures

List of tables

List of acronyms

Abbreviation	Explanation
AC	Alternative Current
DC	Direct Current
DSC	Direct Self Control
DSP	Digital Signal Processing
DTC	Direct Torque Control
EEMF	Extended Electro-Motive Force
EKF	Extended Kalman Filter
EMF	Electro-Motive Force
FCS	Finite Control Set
FOC	Field Oriented Control
FW	Flux Weakening
HFSI	High Frequency Signal Injection
IM	Induction Machine
IPMSM	Interior Permanent Magnet Synchronous Machine
LPS	Low Pass Filter
LQR	Linear Quadratic Regular
MBC	Model Based Control
MFC	Model Free Control
MFPCC	Model Free Predictive Current Control
MPC	Model Predictive Control
MRAS	Model Reference Adaptive System
MTPA	Maximum Torque Per Amper
PCC	Predictive Current Control
PI	Proportional Integrator
PMSM	Permanent Magnet Synchronous Machine
PSO	Particle Swarm Optimization
PWM	Pulse Width Modulation

SMC	Sliding Mode Control
SPWM	Sinusoidal Pulse Width Modulation
SRM	Switched Reluctance Machine
SVD	Space Vector Diagram
SVM	Space Vector Modulation
SVPWM	Space Vector Pulse Width Modulation
TDE	Time Delay Estimation
THD	Total Harmonic Distortion
VSI	Voltage Source Inverter

List of symbols

ε	Angle between i_s and D-Axis	degree°
p	Number of pole pairs	-
J	Coefficient of inertia	Kg.m/s
$\wp$	Permeance of the magnetic circuit	H
ω_m^*	Rotor speed reference	RPM
ω_m	Actual rotor speed	RPM
ψ_s^*	Flux reference	Wb
ψ_s	Actual flux	Wb
$\psi_{d,}^*\psi_q^*$	D-Axis , Q-Axis flux references	Wb
ψ_{abc}	Three phase a,b,c flux	Wb
θ_s	Electrical angle	degree °
θ_m	Mechanical angle	degree °
v_α^*, v_β^*	α-Axis , β-Axis voltage references	V
v_d^*, v_q^*	D-Axis , Q-Axis voltage references	V
$v_{a,b,c}$	Three phase a,b,c actual voltages	V
m_a	Modulation index	-
i_α, i_β	α-Axis , β-Axis actual currents	A
i_s	Stator current	A
i_{dm} , i_{qm}	D-axis , Q-axis currents with iron losses consideration	A
i_d, i_q	D-axis , Q-axis currents	A
i_a, i_b, i_c	Three phase a,b,c actual currents	A
V_{dc}	DC bus voltage	V
T_s	Samling time	S
T_e^*	Electromagnetic torque reference	N.m
T_e	Electromagnetic actual torque	N.m
T_L	Load torque	N.m
R_s	Stator resistor	Ω

P_w	Variations of the magnetic energy stored in the machine.	Watt
P_j	Joule effect losses in the stator windings	Watt
P_e	electrical power	Watt
$N_n i_n$	Magnetomotive sources from the material denoted by "n"	A.t
$N_m i_m$	Magnetomotive sources from the material denoted by "m"	A.t
$M_{nm}, n, m \in \{a, b, c\}$	Mutual inductance of phase "n" and "m"	H
M_2	Second harmonic component of the mutual-inductance	H
M_0	Constant term of the mutual-inductance	H
$L_{\alpha,\beta,h}$	α-Axis, β-Axis inductances	H
L_f	Leakage inductance of a phase	H
L_d, L_q	D-axis , Q-axis inductances	H
L_2	Second harmonic component of the self-inductance	H
L_0	Constant term of the self-inductance	H
K_p	Proportional gain	-
K_i	Integrator gain	-
$I^*_{d\|k}, I^*_{q\|k}$	Discrete D-axis Q-axis current references	A
$I_{d\|k}$, $I_{q\|k}$	Discrete D-axis Q-axis actual currents	A
F_{em}	Electromechanical force	V
B_m	Viscous friction coefficient	-
$\widehat{f_d}$	Estimated D-Axis lumped uncertainties	-
$\widehat{f_q}$	Estimated Q-Axis lumped uncertainties	-
$\widehat{\omega_m}$	Estimated rotor speed	RPM
$\widehat{\theta_m}$	Estimated rotor angle	RPM
$\cos(\varphi)$	Power factor	-
w_d	LPS Cut-off frequency of D-axis lumped uncertainties	Hz
w_q	LPS Cut-off frequency of Q-axis lumped uncertainties	Hz
α_d	D-axis lumped uncertainties Gain	-
α_q	Q-axis lumped uncertainties Gain	-
β_d	D-axis lumped uncertainties Gain	-
β_q	Q-axis lumped uncertainties Gain	-

GENERAL INTRODUCTION

General Introduction

Electric machines play a pivotal role in the majority of variable-speed drive systems, found commonly in industrial plants as well as in everyday applications that influence our daily lives. These electric drives are employed in a wide range of applications operating at both fixed and variable speeds. They are typically equipped with either direct current (DC) machines or alternating current (AC) machines. The DC machine has historically been the most widely used actuator. One of its notable advantages lies in its ease of control, as the torque directly correlates with the armature current. Nonetheless, it is not without drawbacks, primarily associated with its structural characteristics. The presence of a brush-collector system necessitates regular maintenance to address issues like graphite wear. Furthermore, it imposes limitations on rotational speed and restricts its utilization in explosive environments. AC machines can be either asynchronous such as induction machines (IM) or synchronous like Permanent Magnet Synchronous Machine (PMSM). The development of power semiconductors has enabled the creation of voltage or current inverters, paving the way for variable speed in AC machines (synchronous and asynchronous). These machines have numerous advantages over direct current machines. The absence of the commutator increases reliability and allows the production of machines with lower manufacturing and maintenance costs. Technological advances in microelectronics have facilitated the development of highly efficient controls for AC machines (vector control and direct torque control). Many manufacturers now offer drives using these control principles [1], [3].

The principle of electromechanical energy conversion using reluctance variation dates back to the late 19th century. It is even reported that the earliest constructed machines were of the variable reluctance type, referred to as "electromagnetic motors". The Synchronous Reluctance Machine (Syn-RM) is fundamentally a stepper motor and has found numerous applications, particularly in watchmaking [1]. The idea of using the SynRM configuration in a continuous mode (as opposed to step-by-step) with power semiconductor control was introduced by Nasar, French, Koch, and Lawrenson in the 1960s.

In the past two decades, there has been a significant resurgence of interest in the Syn-RM. This machine offers several benefits that make it a viable option for electric drives and servomechanisms. Firstly, it is robust because its cageless version does not have any conductors on the rotor. Secondly, it is easy to construct in its cut-side version, which makes it cost-effective

to manufacture and maintain. Thirdly, the smooth structure of its stator is similar to that of an induction machine, which allows for mass production. However, like other AC machines, the Syn-RM also has notable disadvantages. In addition to its low power factor ($\cos \varphi \cong 0, 6$), the rotor saliency, responsible for electromagnetic torque, leads to torque ripple that manifests as vibrations and acoustic noise [1], [2]. This machine is highly sensitive to magnetic saturation, especially concerning the strongly dependent average torque it produces [4]. It can easily operate in field-weakening mode for increasing speed at constant power. Additionally, sensorless speed control is simpler to implement compared to an asynchronous machine, thanks to its inherent saliency. These advantages suggest promising prospects for its future development.

In this thesis, our work consists of investigating the performance of the Syn-RM through simulations utilizing the control strategies outlined in existing literature. Moreover, it involves developing a set of techniques to enhance the performance of Syn-RM control employing the Direct Torque Control (DTC) and Predictive Current Control (PCC), and elaborating a sensorless speed control by using an observation method that incorporates the Syn-RM dynamic model within the estimation process.

This work is structured into four chapters, organized as following:

Chapter I, dedicated to a literature review is divided in two parts: the first one exposes generalities about the Syn-RM, and the second part encompasses the state-of-the-art in control techniques, with a focus on senssorless speed control techniques available in literature. The mathematical model of a Syn-RM is described and analyzed in Chapter II. Then, the machine is simulated with DTC and FOC control techniques, and the results were presented for comparative discussion. An enhanced version of DTC (E-DTC) was proposed, and simulation results of the new scheme of DTC were compared with the ones obtained through the conventional one.

In Chapter III, a simple structure of Extended Kalman Filter (EKF) observer is incorporated with Space Vector Modulation based DTC (DTC-SVM) , in order to developpe a speed sensorless control scheme , where both speed and position are estimated . Chapter IV develops a novel non-linear Model-Free Predictive Current Control (MF-PCC) based on Time Delay Estimation (TDE), where the Syn-RM parameters-dependent current equations were replaced by model-free expressions, aiming to get rid of the drawbacks related to conventional Model-Based Predictive Current Control (MB-PCC).

Chapter I : State of Art: AC drives and sensorless speed control

I.1 Introduction

An exploration of the state-of-the-art regarding generalities and various structures of synchronous reluctance machine (Syn-RM) will be presented in the first part of this chapter. The second part is then dedicated to exploring the control strategies for Syn-RM. These control strategies are designed to ensure robustness against parametric variations and various disturbances that may affect the performance of the machine. The goal is to achieve stable and accurate control of the Syn-RM under different operating conditions.

Furthermore, delving into the existing sensorless control schemes for Syn-RM reveals their advantage in eliminating the need for a speed sensor, thereby reducing the complexity and cost of the overall system. Sensorless control techniques rely on advanced algorithms and signal processing methods to estimate the rotor position and speed of the Syn-RM based on measured electrical quantities.

Part 1: Generalities on the Syn-RM

I.2 Different structures of Syn-RM

The purpose of this section is to provide a concise summary of the various types of Syn-RM based on their rotor geometry and materials. This is significant because there is a wide range of structures available for Syn-RMs. Numerous researchers and designers have proposed optimized rotor concepts with saliency maximization as a main criterion.

I.2.1 Flux barriers Syn-RM

In order to increase the saliency ratio of the motor, empty spaces of material have been added into the rotor. These gaps are called flux barriers. Their purpose is to restrict the flux in the q-axis direction without hindering it in the d-axis.

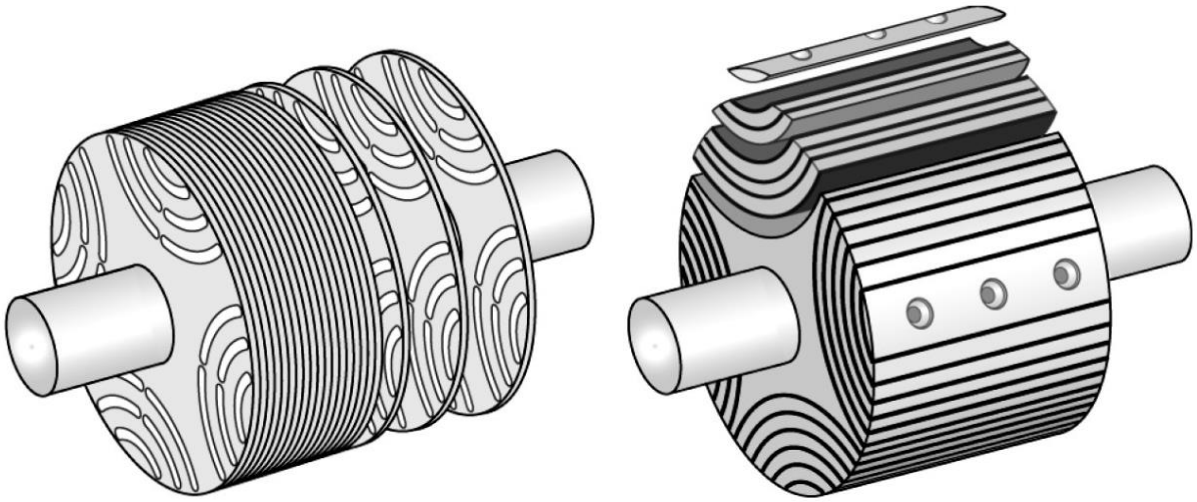

Figure I-1: Radially laminated (a) and axially laminated (b) flux barriers type Syn-RM rotors [60].

Figure I-1 depicts two distinct types of motors that have flux barriers. The first one (**Figure I-1(a))** is radially laminated and its manufacturing process is complicated. This type of rotor has limited mechanical strength, so it is only suitable for low-speed aplications, and its power output is restricted to 2 kW. Nevertheless, it is noteworthy that the saliency ratio in a two-pole motor can reach values as high as 20 [3] and 10 for a four-pole motor [4].

The second rotor shown in **Figure I-1(b)** is an axially laminated motor. It is easier to manufacture compared to the radially laminated rotor and has superior mechanical strength. However, the saliency ratio of this rotor type is not as high as that of the radially laminated motor, with a maximum value of 13 for a two-pole rotor according to [5]. While the flux barriers are typically just air, it is also possible to use a non-magnetic material instead to boost the rotor's mechanical durability.

I.2.2 Permanent magnet assisted Syn-RM

Recently, there has been growing interest in considering Permanent Magnet Assisted Synchronous Reluctance Motors (PMa-SynRM) as a potential alternative motor drive in applications demanding high performance. This interest is particularly notable in the context of electric vehicle traction systems, where the electric motor needs to operate effectively over a wide range of speeds [6], [7]. The Interior PMSM (IPMSM) employs a combination of magnets and

reluctance torque outputs to achieve high efficient drives. Additionally, the utilization of flux-weakening control techniques enables consistent power output or operation within high-speed flux-weakening ranges. Nonetheless, certain drawbacks, such as the relatively substantial *d*-axis current at high speeds and the motor's uncontrollable transition to generator mode following unexpected inverter shutdowns, significantly constrain the motor's use in high-speed electric vehicles [8-10].

On the other hand, akin to the IPMSM , the PMa-SynRM, offers a promising solution to these challenges. Furthermore, the application of the flux-weakening control technique permits the establishment of extended operational zones with constant power output. **Figure I-2** illustrates a configuration of a 4-pole PMa-SynRM featuring a ferrite magnet and reference *d,q*-axis. As depicted in the figure, the main difference between the conventional IPMSM

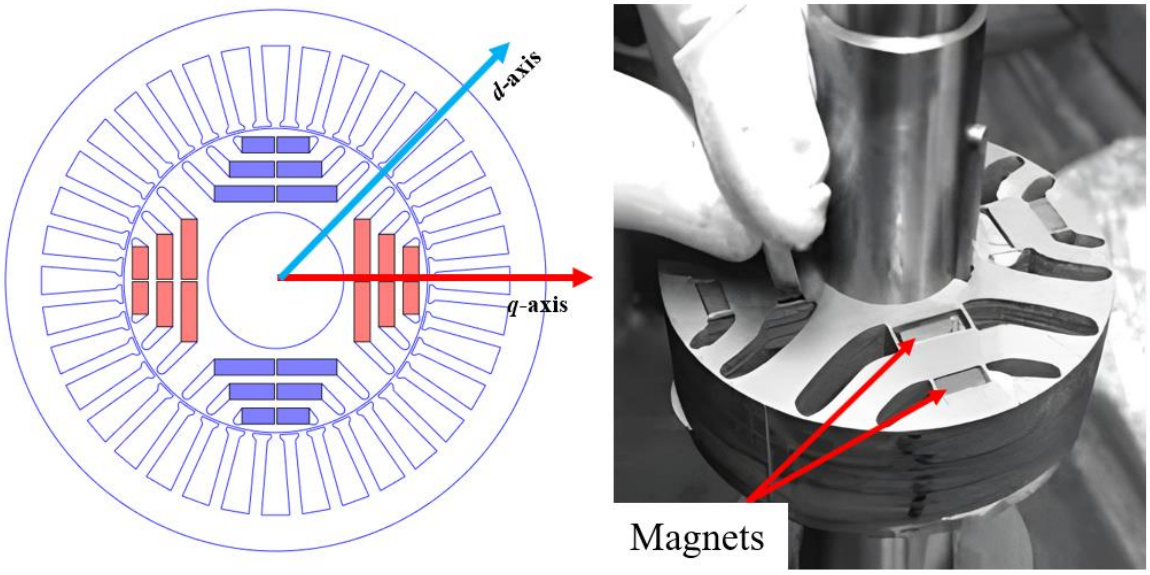

Figure I-2: PMa-SynRM rotor structure view[8].

and the showcased PMa-SynRM lies in the magnetization of the bar magnets along the negative q-axis [10-12].

I.2.3 Switched reluctance machine

The origin of the switched-reluctance machine (SRM) can be traced back to the 19’th century, with records of its application found in a locomotive propulsion system built by Davison in 1838 [13]. The research on reluctance machines began even earlier in 1824 [14]. However, the modern

research on SRM started with the development of modern power electronics in the late of 1960s [15].

SRM's are a promising alternative to AC drive systems that do not require permanent magnets, although their use has been limited compared to other types of machines. The SRM uses a step-by-step control system to generate torque and has shown to have high specific power and high-speed capabilities. Its rotor is made solely of steel, making it a sturdy option. However, the SRM's complex control system, high noise level, and unusual power electronics architecture have posed challenges in some application systems. As depicted in **Figure I-3** ,the stator and rotor of a typical SRM have a salient geometry, and the winding on the stator pole is often single-toothed, making it difficult to analyze the torque performance due to its highly nonlinear electromagnetic behavior [15].

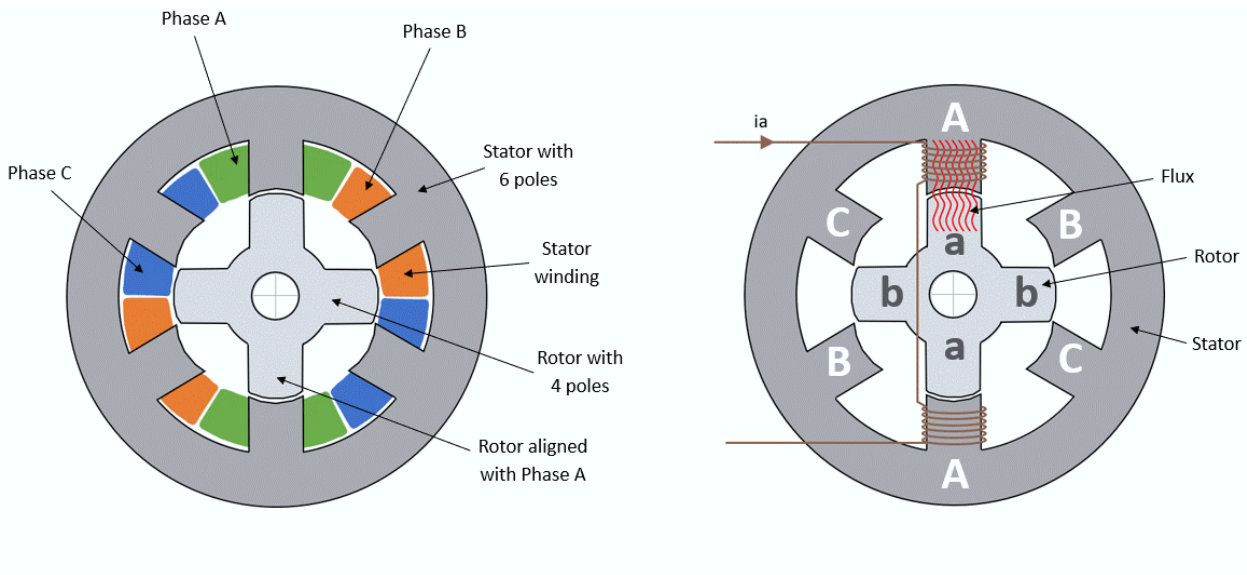

Figure I-3: 6/4 type switched reluctance machine (SRM)[2].

I.3 Impact of the Ld/Lq ratio on the machine performance

A detailed study of the influence of the Ld/Lq ratio on the performance of the Syn-RM machine is given in [16] and [17].

This type of machine produces steady-state electromagnetic torque in the rotor reference frame, which can be expressed using the first space harmonic. The equation for this torque is given as follows:

$$T_e = \frac{3}{2} p\left(L_d - L_q\right) i_d i_q \quad \text{(I. 1)}$$

where:

- p is the number of pole pairs;
- i_d and i_q are, respectively, the stator currents of direct and quadrature axes, expressed in the rotor reference frame.
- L_d and L_q are, respectively, the direct and quadrature stator inductances. In **Figure I-4**, the angle ε marks the position of the stator current vector i_s with respect to the d-axis. In steady state, this vector is fixed.

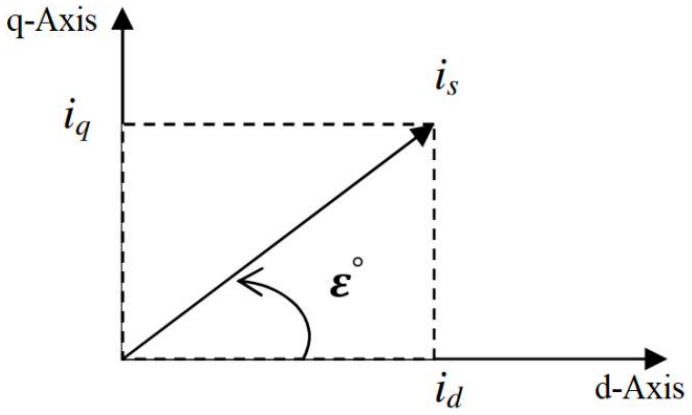

Figure I-4:Position of the stator current in the d, q reference frame.

The value of the stator current magnitude is given by the following equation:

$$i_s = \sqrt{i_d^2 + i_q^2} \quad \text{(I. 2)}$$

The electromagnetic torque can be expressed as a function of ε and the stator current i_s:

$$T_e = p\left(L_d - L_q\right) i_s^2 \sin(2\varepsilon) \quad \text{(I. 3)}$$

It is shown from the two previous relations that for a given value of the stator current, the torque is maximum when $\varepsilon = \pi/4$, which corresponds to impose $i_q = i_d$. This mode of operation corresponds to a particular control strategy called Maximum Torque Per Ampere (MTPA). By putting $\varepsilon = \pi/4$ in equation (I.3), we obtain equation (I.4):

$$T_e = pL_d i_s \left(1 - \frac{1}{\left(\frac{L_d}{L_q}\right)} \right) \quad \text{(I. 4)}$$

We can define the power factor of the machine which corresponds to the phase shift between the fundamental of the line current and the corresponding simple voltage. This factor also represents the ratio between the active power and the apparent power absorbed by the machine. It is important that this ratio is as close as possible to 1 to limit the electrical power of the source supplying the machine. By neglecting the losses in the machine model, we obtain a simple expression for the power factor:

$$\cos(\varphi) = \frac{\left(\frac{L_d}{L_q} - 1\right)\sin(\varepsilon)}{\sqrt{\left(\frac{L_d}{L_q}\right)^2 + \tan^2(\varepsilon)}} \quad \text{(I. 5)}$$

We have given in **Figure I-5**, the variations of the power factor according to the inductance ratio L_d/L_q .We can observe in this figure that the power factor starts to become interesting for saliency ratios higher than 6. Taking into account the electrical losses (Joule losses and iron losses) this power factor slightly increases [16], [17]. Equations (I.4) and (I.5) show that to optimize the performance of the machine, it is necessary to design a rotor structure such that the inductance L_d has the largest possible value and such that the ratio (L_d/L_q) is as large as possible.

Figure I-5*:* Power factor versus saliency ratio of Syn-RM [98].

Part 2: Control and speed estimation techniques for the Syn-RM

I.4 Different techniques used for the control of a Syn-RM: state-ofthe-art

The control of electrical machines has been the subject of many researches and works for a long time. In order to take advantage and exploit their best performances, different control techniques have been developed to control the Syn-RM. The main controls and their derivatives belong to the same category, so in this section we will focus on the most well-known techniques that have been the subject of numerous publications.

I.4.1 Field oriented control

The vector control of AC machines is now well-known. Many industrial companies market speed drives for synchronous and asynchronous machines using this control method. The principle of vector control is identical to that of separately excited DC machine control. However, it is necessary to use a specific reference frame where the electromagnetic torque is expressed simply based on the components of currents along two axes (*d*-axis and *q*-axis). Typically, the *d*-axis component of the stator current acts as the excitation and allows for adjusting the flux value in the machine. The *q*-axis component serves as the armature current and enables torque control. With this type of control, high-performance drive systems are achieved, capable of delivering the rated torque at the rated speed even during startup.

The use of the vector control technique for synchronous motor drive systems is becoming more popular due to the rapid development of microprocessors and digital signal processors (DSP's). The vector control method, which was first introduced in the 1960's by Blaschke, Hasse, and Leonhard in Germany, has gained popularity due to advancements in technology [18-20].

The underlying principle of FOC is to separate the torque and magnetic field components of the motor and control them independently. This is achieved by transforming the stator currents from a stationary reference frame (*abc*) to a rotating reference frame (*d,q*) using Park's transformation. The *d*-axis is aligned with the rotor flux, while the *q*-axis is perpendicular to it. By controlling the current in the d-axis, which produces the torque, and the current in the q-axis, which produces the magnetic field, the torque and magnetic field components can be decoupled. The Park's transformation concept was introduced by Park in 1929, and FOC controllers are based on the reference frame theory, maintaining a 90-degree angle (electrical) between the stator and rotor field components. [19]. It can control the current individually along *d-q* axes in the machine. A typical FOC structure for Syn-RM is shown in **Figure I-6**.

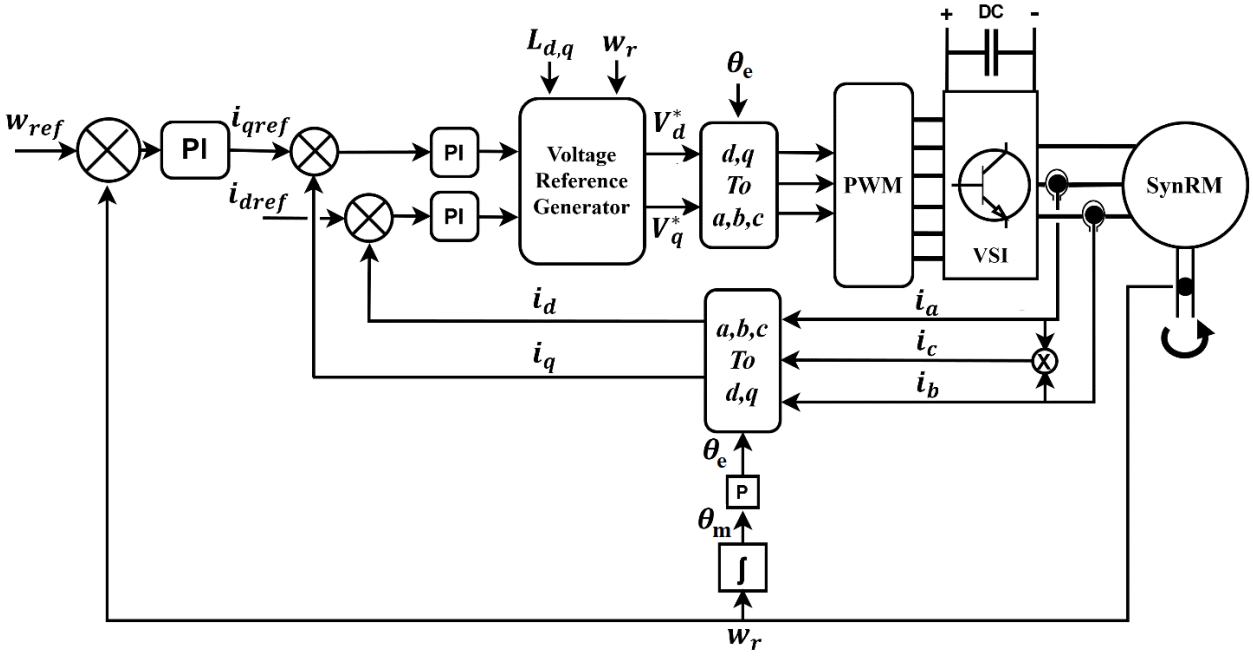

Figure I-6 *:* Schematic block of Filed Oriented Control (FOC).

I.4.2 Direct torque control

As depicted in **Figure I-7,** the direct torque control (DTC) principle involves selecting voltage vectors directly based on the difference between the desired and actual values of torque and flux. This is done by comparing torque and flux errors using hysteresis comparators **(Figure I-8)**. These comparators help choose a voltage vector from a predefined set without needing pulse width modulation. Instead, one of six voltage vectors is used consistently for a specific sampling period [21]. DTC offers benefits like indirect control of stator current and voltage, achieving nearly sinusoidal stator flux and currents, and fast dynamic response from the machine. However, the DTC has some drawbacks such as high torque ripple and variable switching frequency caused by the variable errors generated by hysteresis comparator. Thus, the settings of these comparators (bandwidths) have a direct effect on the switching frequency and the steady state error of torque and flux [22].

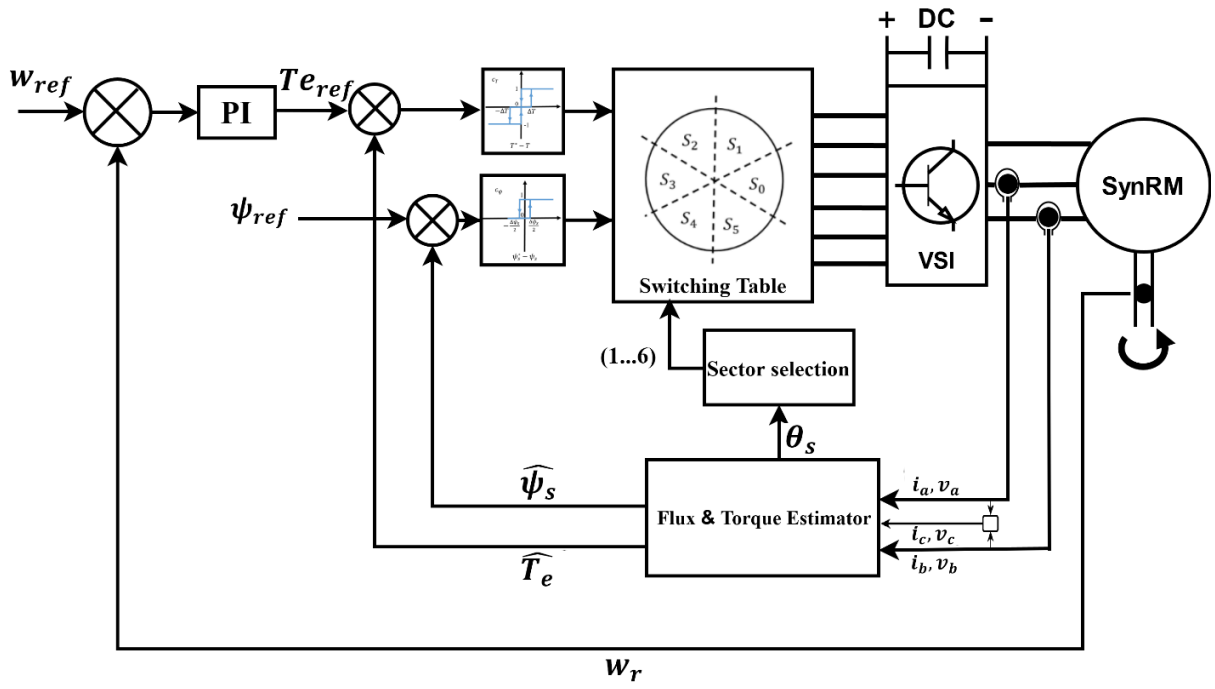

Figure I-7*:* Schematic block of Direct Torque Control (DTC).

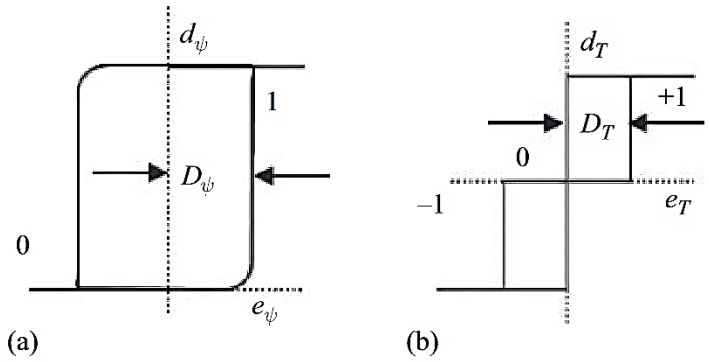

Figure I-8: Flux and torque comparators.

I.4.3 Space vector modulation based direct torque control

Direct Torque Control - Space Vector Modulation (DTC-SVM) is a control technique used in electric motor drives to achieve high-performance torque and speed control. It combines the principles of Direct Torque Control (DTC) and Space Vector Modulation (SVM) to achieve superior performance [23]. As shown in **FigureI-9** ,The objective of SVM is to choose suitable switching vectors to minimize the distortion caused by current harmonics. By carefully selecting the voltage vectors within each sampling period, a constant switching frequency is maintained. As a result, the DTC-SVM technique reduces torque fluctuations and effectively manages the stator flux and torque. Furthermore, it offers several advantages over other control techniques such as fast dynamic response, reduced torque ripple, and simplified control structure. It is widely used in industrial applications such as electric vehicles, wind turbines, and robotics [24].

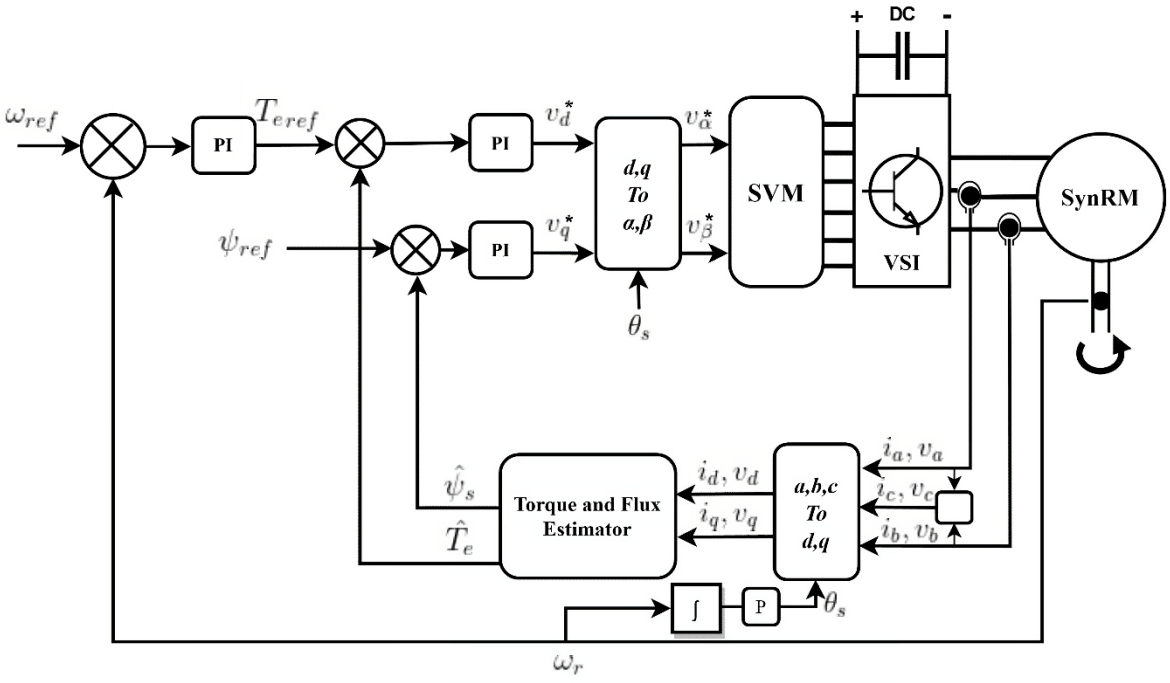

Figure I-9: Schematic block of SVM based Direct Torque Control (DTC-SVM).

I.4.4 Model predictive control

Model Predictive Control (MPC) is a type of advanced control technique that predicts the future behavior of a system and determines the optimal control action to achieve a desired outcome. In the context of Syn-RMs, MPC is a control strategy that can be used to optimize the machine's performance by adjusting the stator currents to achieve the desired torque and speed. As depicted in **Figure I-10** MPC of Syn-RMs involves creating a current model of the machine and its associated power electronics which is why this approach is referred to as Predictive Current Control (PCC), and then using this model to predict the future behavior of the system. The control algorithm then computes an optimal control action that minimizes a cost function based on the predicted future quantities [25]. This cost function can be designed to optimize a range of performance criteria, such as minimizing torque ripple, maximizing efficiency, or achieving a desired speed trajectory [26].

MPC of Syn-RMs has been shown to provide superior performance compared to traditional control techniques such as field-oriented control (FOC) and direct torque control (DTC). This is because MPC can take into account the non-linear behavior of Syn-RMs, which can result in better accuracy and stability of the control system. However, MPC requires a more complex control

algorithm and higher computational power, which may limit its applicability in some real-time control applications [27]. The standard schematic diagram of Syn-RM is depicted in **Figure I-10**, where Maximum Torque Per Ampere (MTPA) is employed to optimize the i_d and i_q current references.

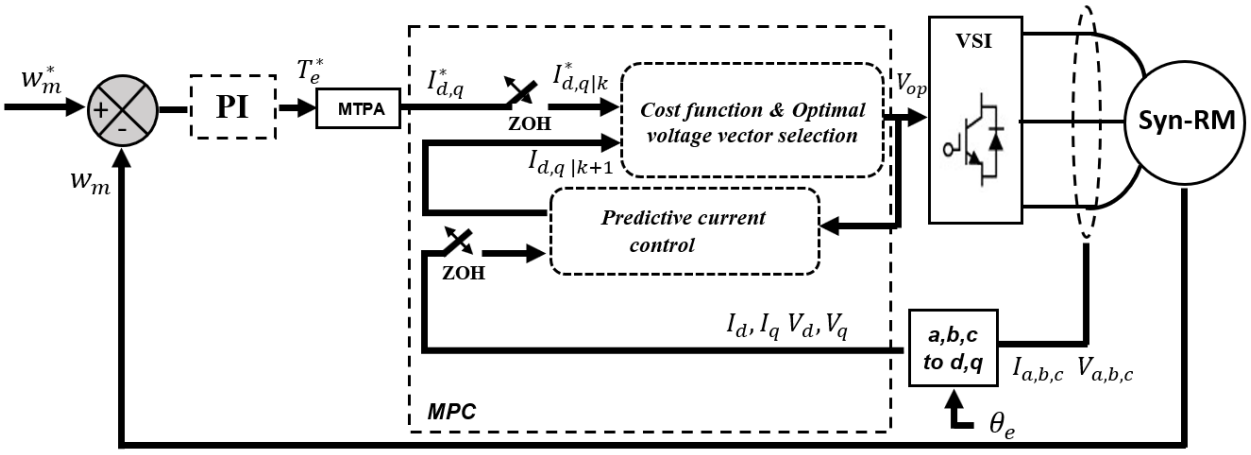

Figure I-10: Schematic block of Model Predictive Control (MPC).

I.5 Sensorless control of Syn-RM: state-ofthe-art

Sensorless control of Syn-RM is a technique that eliminates the need for a sensor to measure the rotor position and speed of a Syn-RM. Sensorless control can reduce the cost, complexity and maintenance of Syn-RM drives, and improve their reliability and performance. Various approaches exist for sensorless control of Syn-RM, including those relying on rotor saliency, back ElectroMotive Force (EMF), and model-based techniques. One of the model-based methods is the Extended Kalman Filter (EKF), which can estimate the rotor position, speed and parameters of Syn-RM using a mathematical model and the measured stator currents. Another method is the High-Frequency Signal Injection (HFSI), which injects a high-frequency current signal with random frequency and phase to induce a saliency effect in Syn-RM and detect the rotor position from the resulting voltage response. Sensorless control of Syn-RM can improve the efficiency, torque quality and dynamic response of Syn-RM drives, especially at low- and zero-speed regions. Obviously, industrialists are looking for solutions to increase reliability and reduce costs. For these reasons, several sensorless control techniques have been developed in recent years. We can mention in particular:

- Speed and position estimation in dynamic conditions based on extended electromotive force [28-31];
- The estimation in dynamic region based on the injection of a high frequency signal [25] [32-37] ;
- The estimation of the position in dynamic region using the extended Kalman filter [38-43];

I.5.1 Speed estimation based on extended electromotive force

The speed and position information of the machine is contained in its electromotive force (EMF). Since the EMF is proportional to the speed of rotation, it becomes impossible to extract the EMF waveform at low speeds because it is buried in the measurement noise. EMF-based algorithms are suitable for smooth pole machines and require approximations when adopted for salient pole machines. However, these approximations deteriorate the performance of the estimator and can make the system unstable. A variant of the EMF method, known as the Extended EMF (EEMF) technique, estimates the position and speed of the machine from the EMF with the consideration of the saliency of the machine [30]. Thus, the estimation of the speed and position of the Syn-RM based on the EEMF has been proposed by many researchers. This method can be used for all synchronous machines. However, it cannot be used at low speed or at standstill.

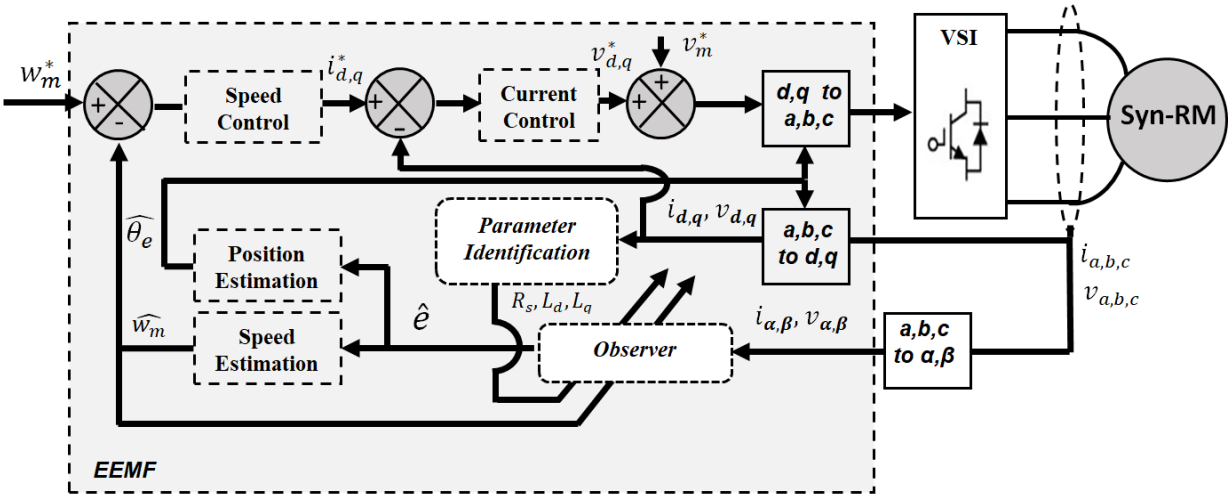

Figure I-11: Sensorless control scheme based on EEMF.

In [44], Schroedl and Weinmeier studied two different algorithms to calculate the rotor position of a Syn-RM. In the low-speed region, the d- and q-axis inductances were identified online using the measured currents and voltages. The rotor position was deduced from these inductances. At

high speeds, the EMF was employed to estimate the rotor position. It appears that this method is computationally intensive due to its complexity. In [45], Capecchi et al. present sensorless control of the Syn-RM using a combination of two rotor position estimation methods: an EMF-based estimation and a high frequency flux signal injection method. At low speed, a high frequency alternating flux is injected. When the flux amplitude is large enough (about 5% to 6% of the nominal flux), the injection signal is removed and the estimation is based on the EMF. The disadvantage of this method is the noise due to the injected signal. **Figure I-11** represent the basic scheme of EEMF based sensorless control.

Ichikawa et al. [29] also proposed a sensorless control of the Syn-RM based on the EEMF model. At standstill, when the EEMF amplitude is zero, it is impossible to perform the position estimation from the EEMF. In order to solve this problem, a system identification method for sensorless control is proposed. This method can estimate the position of the rotor, even at standstill, by the identification system. It can estimate the rotor position from the current and voltage signals with white noise injection. Moreover, this method is not affected by parameter variations because it does not use the machine parameters. Conversely, the rotor position estimation based on EEMF model must use the machine parameters. In order to accurately estimate the rotor position, the machine parameters need to be well known. The inductances and resistances of the Syn-RM vary at high currents, in particular, due to magnetic saturation. Therefore, the precise measurement of the machine parameters is difficult and complex. To address these problems, Ichikawa et al. [30] proposed a sensorless control of the Syn-RM based on the EEMF model considering the magnetic magnetic saturation and with the identification of the on-line parameters, from the stator currents and voltages. However, the process of calculation and identification of the parameters is complex. The proposed method has been validated experimentally from 500 to 1000 rpm.

I.5.2 Estimation based on high frequency signal injection

In recent years, the High-Frequency Signal Injection (HFSI) method has often been used to detect the position of the Syn-RM in the zero- and low-speed operating regions [48]. In [32] Agarlita et al. proposed a sensorless control for a Syn-RM by combining the methods of high-frequency current injection, in the low-speed region, and active flux estimation based on stator voltages, in the high-speed region. Stator current injection in the d-axis then requires appropriate demodulation of the signal. Unfortunately, at high speed, the controllable voltage margin decreases

because of the voltage drop due to the injected high-frequency signal. In addition, the injected current causes additional losses and noise. A similar research by Consoli et al. [46]considers only the operation at low- and zero-speed regions. De Kock [47] compared the anisotropy of the Syn-RM with that of the PMSM for sensorless control, using high-frequency signal injection and appropriate demodulation. This study has refined the high-frequency model (anisotropy model) of a Syn-RM and a PMSM to implement robust and stable robust position estimation at low- and zero-speed. In [37], Consoli et al. presented a new rotor position estimation obtained by adding a small high-frequency sinusoidal voltage to the stator reference voltage for the Syn-RM. A stator voltage component is then generated orthogonally to the injected signal and its amplitude depends on the phase shift between the d-axis and the direction of the injected signal. A robust tracking can be achieved by adjusting the direction of the carrier voltage to minimize the amplitude of the orthogonally generated voltage. This technique works only at low speeds and at zero speed. The standard control schematic of HFSI is presented in **Figure I-12.**

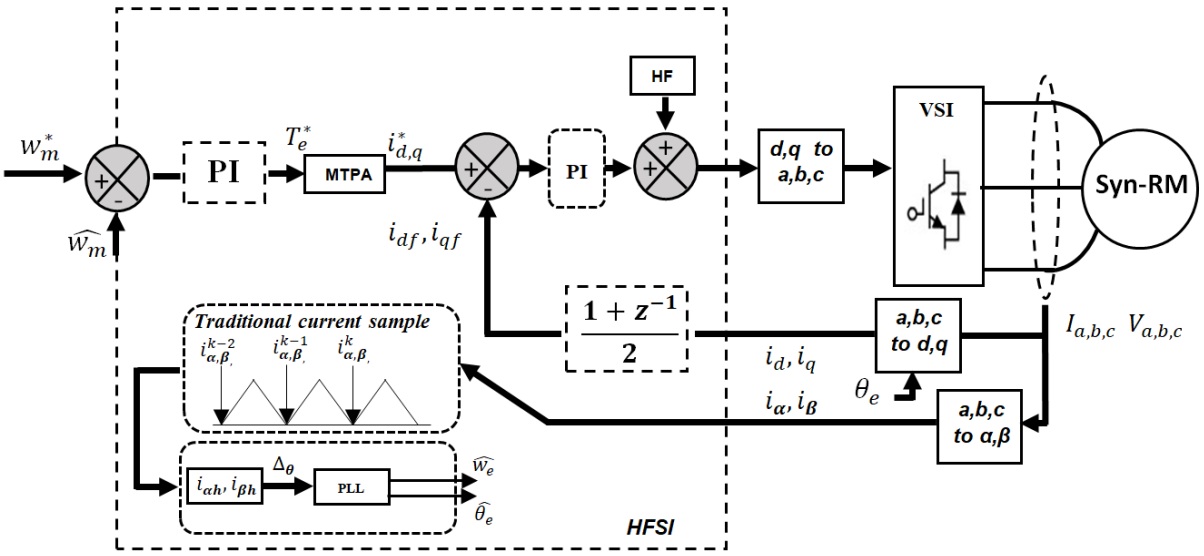

Figure I-12:Sensorless control scheme based on High Frequency Signal Injection.

I.5.3 Luenberger deterministic observer

The Luenberger observer is the most well-known in the class of deterministic type [49]. From measurements of inputs and outputs, we can reconstruct the state of the observable linear system. It is used in state feedback control when all or part of the state vector cannot be measured. In its extended version, it allows estimating the variable or unknown parameters of a system. In [50] , a

Luenberger-type flux observer was used to reconstruct the rotor position. The proposed estimator has many advantages, notably the fact that it does not depend at all on the initial position of the rotor, and it works equally well at speeds approaching zero as at very high speeds. The implementation of this technique is presented in [49], where the experimental results were presented and discussed.

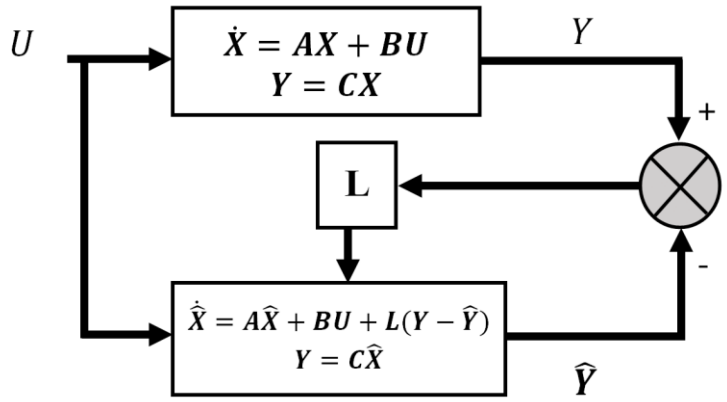

Figure I-13: Luenberger observer standard scheme.

I.5.4 Estimation based on extended Kalman filter

The Kalman filter is an optimal state observer for a defined stochastic context. It allows the reconstruction of the state of a system from the input and output signals. The basic Kalman filter algorithm is designed to estimate the state vector of a system with a linear model. If the model is nonlinear, it must be linearized to apply the Kalman filter (this is called an Extended Kalman Filter) [42]. The principle of the Kalman filter algorithm can be illustrated by the block diagram in **Figure I-14**.

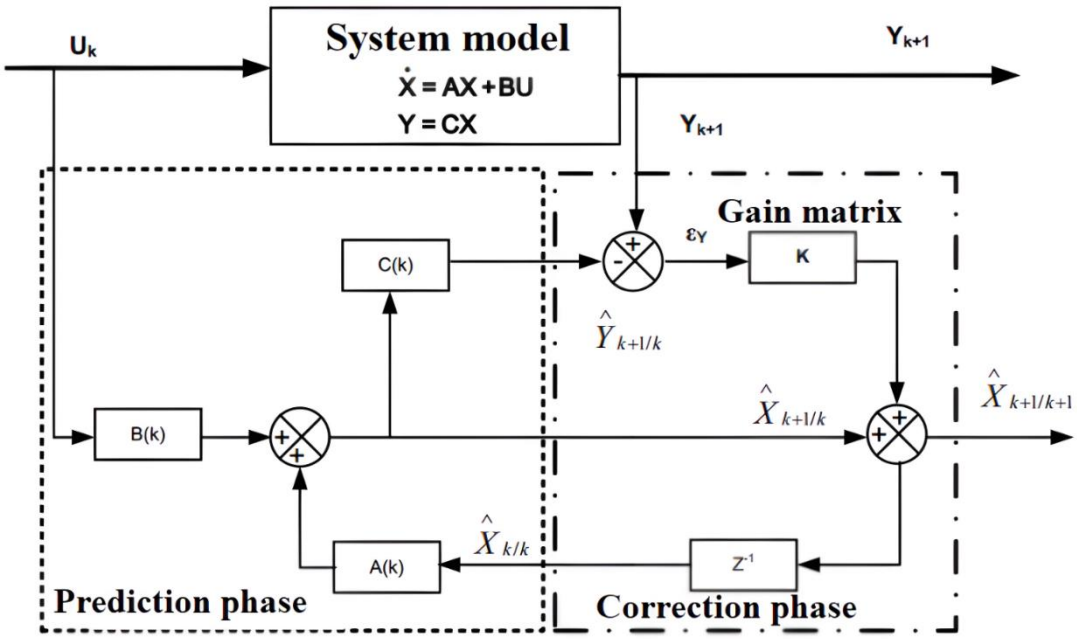

Figure I-14: Schematic block of Kalman filter principle[52].

A Kalman filter can simultaneously estimate several electrical and mechanical variables of the machine. The disadvantage of the Kalman filter lies in its high computational process because of the presence of several matrix calculations, which makes this algorithm difficult to implement in real-time. The advantage of this technique is the filtering of the estimated signals [51]. Many sensorless control strategies using EKF have been reported, but more commonly with PMSM [52-54] [38]. To our knowledge, only few papers have addressed sensorless control of Syn-RM by EKF and they were limited to low- and medium-speeds [77], [78].

In [39], Mynar et al. proposed a sensorless control with a EKF considering the stator iron losses. The developed EKF is based on the voltage equations considering the stator iron losses and the dynamic equation of the Syn-RM to estimate its position and speed. The results show that the position and speed are well estimated, but only at low- and medium-speeds (less than 1000 rpm). The EKF based on parameter identification method for synchronous motor and IPMSM has been described in [55] [56]. Nonetheless, the main downsides of the EKF are the tuning and design of the covariance matrices. In [57], some guidelines are used to obtain these matrices. However, this method is still based on a trial-and-error method.

I.6 Conclusion

In this chapter, a description of the various rotor structures developed so far for SynRMis provided, where an explanation was given on the impact of the inductance saliency ratio upon the output power of the machine. The second part presents a stateof-the-art review listing several techniques for controlling the Syn-RM and estimating its rotor speed and position. It was necessary to review the new methods proposed in recent years for sensorless control of electric machines, particularly the Syn-RM. The development of estimators continues to grow, which drives many researchers to deepen their studies.

Chapter II : Modeling and control simulation of the Syn-RM

II.1 Introduction

In this chapter, the focus is dedicated to the comprehensive modeling and control simulation of the Syn-RM. Beginning with a concise overview of the fundamental concept of reluctance torque, a crucial aspect is highlighted in understanding the behavior of the Syn-RM. Subsequently, the state space model of the Syn-RM is delved into, providing a robust mathematical representation of its dynamic behavior and interactions. Understanding the state space model is essential for the development of effective control strategies for this type of machine.

Subsequently, attention shifts to two prominent control theories: Direct Torque Control (DTC) and Field-Oriented Control (FOC). These advanced control techniques have proven to be highly effective in regulating the Syn-RM, ensuring optimal performance and efficiency. Throughout the discussion of these control theories, their key principles, advantages, and potential drawbacks are analyzed, enabling a comprehensive understanding of their applicability in real-world scenarios. Then, the results obtained during the simulation phase are presented and examined. These results offer valuable insights into the performance and effectiveness of the presented control strategies under various operating conditions. By comparing and analyzing these outcomes, the goal is to identify the most suitable control approach for maximizing the Syn-RM's performance, efficiency, and overall stability.

Finally, an enhanced control scheme for DTC (E-DTC) will be elaborated and simulated using the Syn-RM model. This will serve to highlight the advantages offered by this technique. Furthermore, a comparative discussion with conventional DTC will be presented in this section to provide a comprehensive evaluation of E-DTC.

II.2 Principle of the Syn-RM

If a magnetic field is applied to a magnetic material having different reluctances along two perpendicular axes ("d" and "q"), a reluctant torque is produced if the axis of symmetry of the magnetic material is not aligned with the magnetic field. This position where $\delta \neq 0$ creates field distortion in the space where the magnetic material is located **(Figure II-2).** The reluctant torque will tend to rotate the material to reduce the angle δ and to minimize the magnetic energy. If this angle δ is kept constant through torque control or applied resistive torque, the electromagnetic energy is then continuously converted into mechanical energy. Let's place two magnetic rods **(Figure II-3),** one of which is surrounded by N coils in which a current i flows and the other

without coils. Initially, the two bars are offset. The general expression giving the electromechanical force F_{em} of interaction between two magnetomotive sources represented by $N_N i_N$ and $N_m i_m$ is written as [59]:

$$F_{em}(x) = \frac{1}{2}\sum_{n=1}^{k} \frac{\partial \wp_{nn}}{\partial x}(N_n i_n)^2 + \sum_{n<m}^{k} \frac{\partial \wp_{nm}}{\partial x}(N_n i_n)(N_m i_m) \qquad \text{(II. 1)}$$

Where $\wp$ is the permeance of the magnetic circuit with respect to the x axis at a given position of the magnetic material.

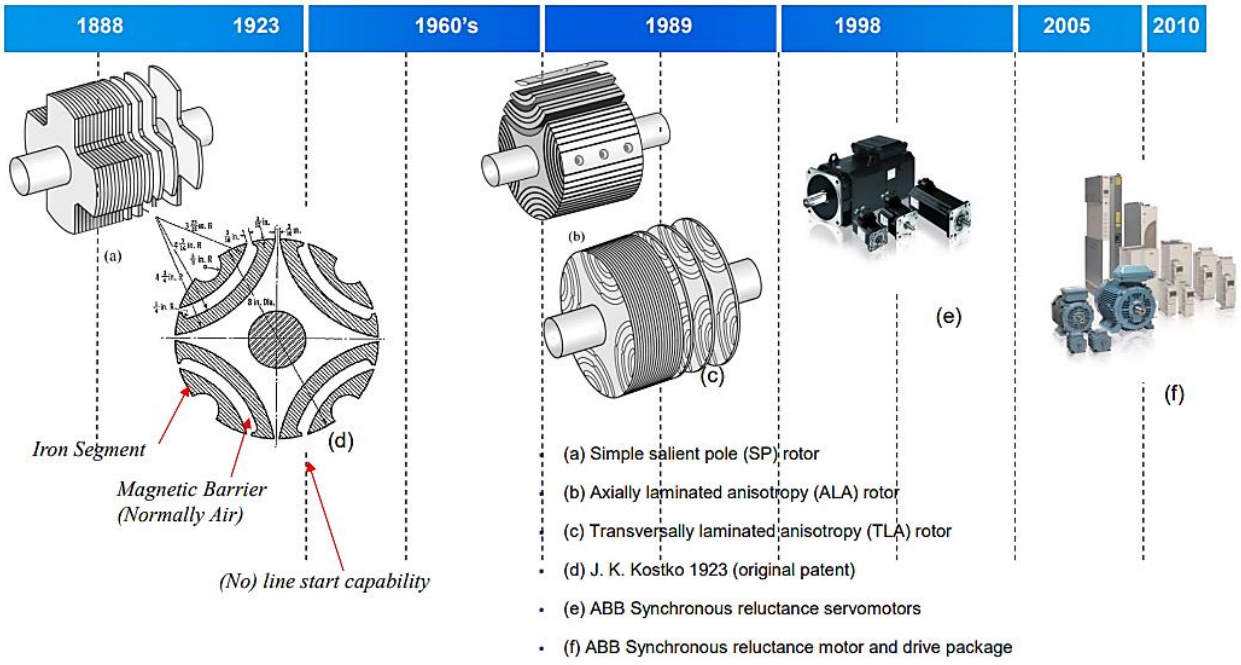

Figure II-1: History of design evolution of the Syn-RM [58].

Figure II-1 depicts a historical summary about the Syn-RM design evolution.

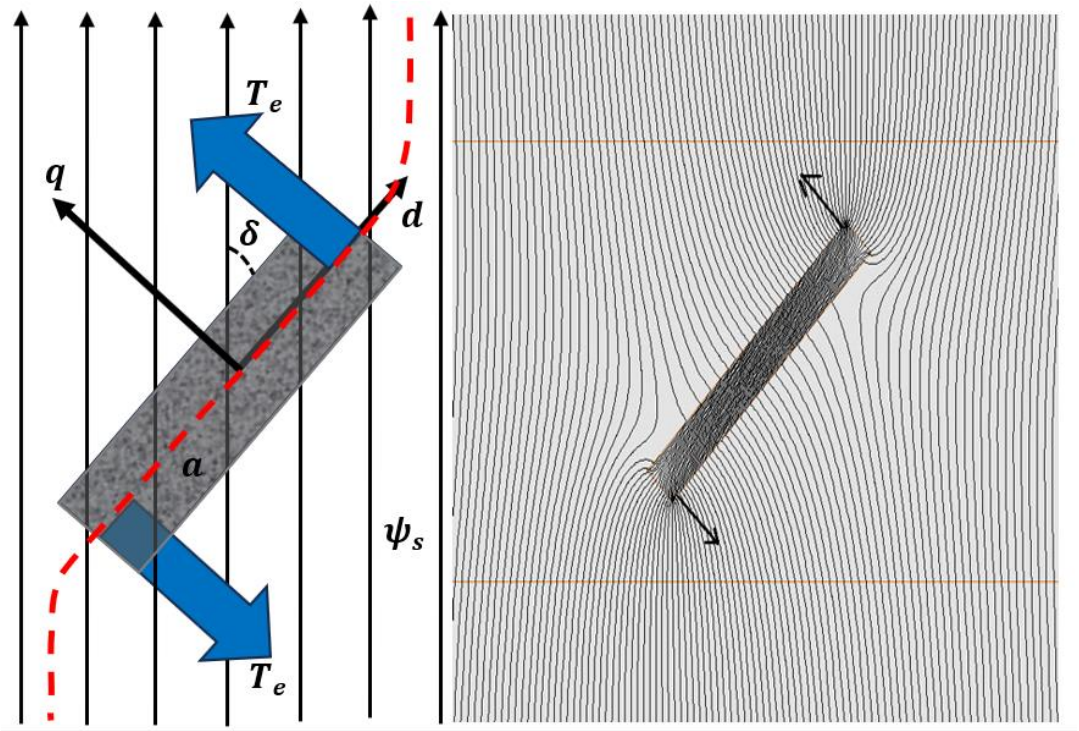

Figure II-2: Concept of reluctant torque [60].

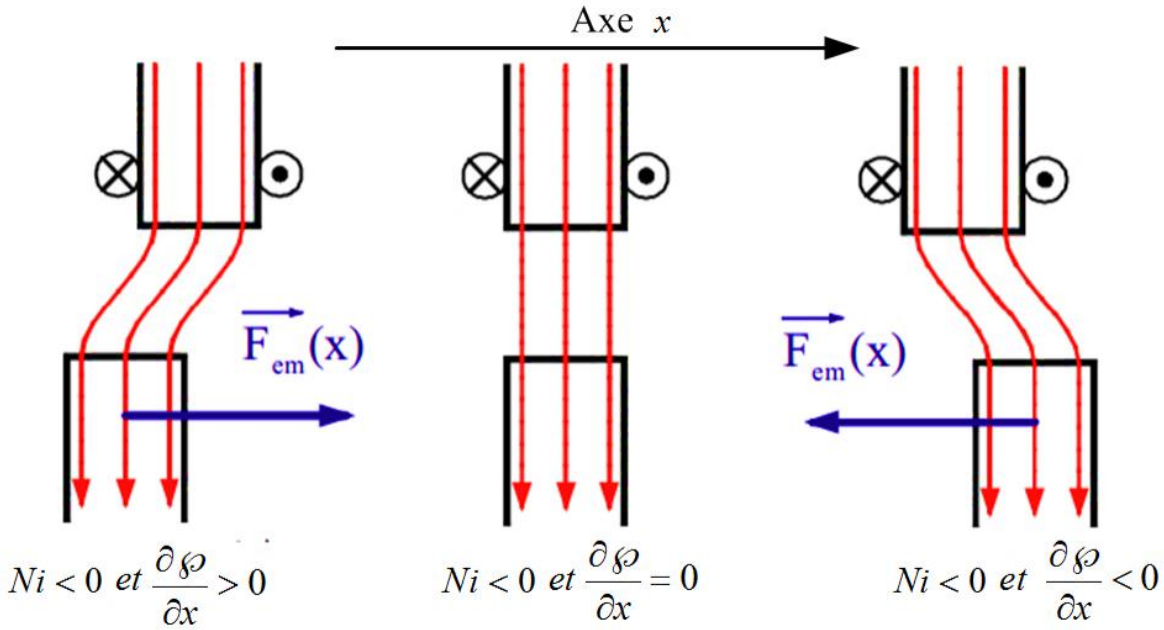

Figure II-3: Reluctant force generation between two magnetic bars [92].

In our case **(Figure II-3),** there is only one magnetomotive source represented by (*Ni*), and the resulting electromechanical force is then given by:

$$F_{em}(x) = \frac{1}{2}\frac{\partial \wp_{nn}}{\partial x}(Ni)^2 \qquad \text{(II. 2)}$$

We are therefore dealing with a reluctance force whose direction depends only on the variation in magnetic circuit permeance.

II.3 Syn-RM model

II.3.1 Simplifying assumptions

In order to develop the equivalent electrical model of the machine, it is necessary to make certain assumptions. In the case of the Syn-RM, the modeling is dependent on the following simplifying assumptions:

- The hysteresis in the magnetic parts is negligible;
- Notch and gap harmonics are not taken into account;
- The spatial distribution of the magnetomotive forces in the air gap is sinusoidal;

First, let's recall the classical model of the Syn-RM, neglecting the rotor currents. Nevertheless, the rotor of our machine is massive and conductive. It will be noticed that during flux transients, the influence of the rotor currents is significant, and sometimes, it will be necessary to consider them to improve our model.

II.3.2 Electrical equations of the machine in the abc reference frame

The electrical equations governing the operation of a synchronous machine in a three phase fixed reference frame *(a,b,c)* linked to the stator are written in the following form [61]:

$$[V_{abc}] = [R_s][I_{abc}] + \frac{d}{dt}[\Psi_{abc}] \qquad \text{(II. 3)}$$

Where : $[V_{abc}] = \begin{bmatrix} v_a \\ v_b \\ v_c \end{bmatrix}; [I_{abc}] = \begin{bmatrix} i_a \\ i_b \\ i_c \end{bmatrix}; [\Psi_{abc}] = \begin{bmatrix} \psi_a \\ \psi_b \\ \psi_c \end{bmatrix}; [R_s] = \begin{bmatrix} R_s & 0 & 0 \\ 0 & R_s & 0 \\ 0 & 0 & R_S \end{bmatrix}.$

The totalized fluxes of the stator phases are written in the stator-related reference frame in the following matrix form:

$$[\Psi_{abc}] = [L][I_{abc}] \tag{II. 4}$$

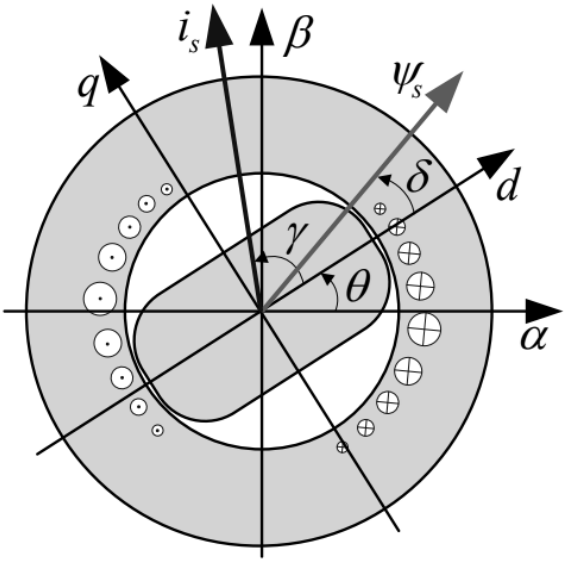

Figure II-4: Fixed frame α, β and rotor frame d, q vector diagram.

where $[L]$ is the inductance matrix which depends on the angle θ defined by **Figure II-4**:

$$[L] = \begin{bmatrix} L_a(\theta) & M_{ab}(\theta) & M_{ac}(\theta) \\ M_{ba}(\theta) & L_b(\theta) & M_{bc}(\theta) \\ M_{ca}(\theta) & M_{cb}(\theta) & L_c(\theta) \end{bmatrix} \tag{II. 5}$$

With the assumption of the first space harmonic, the terms in (II.5) are written as:

$$\begin{aligned} L_a(\theta) &= L_f + L_0 + L_2\cos(2\theta) \\ L_b(\theta) &= L_f + L_0 + L_2\cos\left(2\theta + \frac{2\pi}{3}\right) \\ L_c(\theta) &= L_f + L_0 + L_2\cos\left(2\theta - \frac{2\pi}{2}\right) \end{aligned} \quad \left| \quad \begin{aligned} M_{ab}(\theta) &= M_{ba}(\theta) = M_0 + M_2\cos\left(2\theta - \frac{2\pi}{3}\right) \\ M_{ac}(\theta) &= M_{ca}(\theta) = M_0 + M_2\cos\left(2\theta + \frac{2\pi}{3}\right) \\ M_{bc}(\theta) &= M_{cb}(\theta) = M_0 + M_2\cos(2\theta) \end{aligned} \right. \tag{II. 6}$$

L_f is the leakage inductance of a phase, L_0 and L_2 are the constant term and second harmonic components of the self-inductance respectively. Under the same framework of assumptions, we have the following relations:

$$M_0 = -\frac{1}{2}L_0 \text{ et } M_2 = L_2 \tag{II. 7}$$

II.3.3 Electrical equations of the machine in the frame α, β

With a two-phase current system, produced by two coils offset by $\pi/2$ in space, we can create a rotating field identical to that created by any three-phase system. There are two transformations: the Clarke transformation and the Concordia transformation. The Clarke transformation preserves the amplitude of the quantities, but not the power or the torque (they must be multiplied by a coefficient 3/2). On the other hand, the one of Concordia, which is normalized, keeps the power, but not the amplitudes. It is preferred to use the Clarke transformation, because it facilitates the analysis of temporal signals and the adjustment of the limitations. One can obtain, in the general case [62]:

$$\begin{bmatrix} x_a \\ x_b \\ x_c \end{bmatrix} = [C_{32}] \begin{bmatrix} x_\alpha \\ x_\beta \\ x_h \end{bmatrix}; \begin{bmatrix} x_\alpha \\ x_\beta \\ x_h \end{bmatrix} = [C_{23}] \begin{bmatrix} x_a \\ x_b \\ x_c \end{bmatrix} \quad \text{(II. 8)}$$

where:

$$[C_{23}] = \frac{2}{3} \begin{bmatrix} 1 & -\frac{1}{2} & -\frac{1}{2} \\ 0 & \frac{\sqrt{3}}{2} & -\frac{\sqrt{3}}{2} \\ \frac{1}{2} & \frac{1}{2} & \frac{1}{2} \end{bmatrix}; [C_{32}] = [C_{23}]^{-1} = \begin{bmatrix} 1 & 0 & 1 \\ -\frac{1}{2} & \frac{\sqrt{3}}{2} & 1 \\ -\frac{1}{2} & -\frac{\sqrt{3}}{2} & 1 \end{bmatrix} \quad \text{(II. 9)}$$

The system of equations (II.3) becomes:

$$[V_{\alpha\beta h}] = [R_s][I_{\alpha\beta h}] + \frac{d}{dt}[\psi_{\alpha\beta h}] \quad \text{(II. 10)}$$

where:

$$[V_{\alpha\beta h}] = \begin{bmatrix} v_\alpha \\ v_\beta \\ v_h \end{bmatrix}; [I_{\alpha\beta h}] = \begin{bmatrix} i_\alpha \\ i_\beta \\ i_h \end{bmatrix}; [\psi_{\alpha\beta h}] = \begin{bmatrix} \psi_\alpha \\ \psi_\beta \\ \psi_h \end{bmatrix} \quad \text{(II. 11)}$$

The flux matrix is given by:

$$[\psi_{\alpha\beta h}] = [L_{\alpha\beta h}][I_{\alpha\beta h}] \quad \text{(II. 12)}$$

with:

$$\left[L_{\alpha\beta h}\right] = \begin{bmatrix} L_f + \frac{3}{2}(L_0 + L_2\cos(2\theta)) & \frac{3}{2}L_2\sin(2\theta) & 0 \\ \frac{3}{2}L_2\sin(2\theta) & L_f + \frac{3}{2}(L_0 - L_2\cos(2\theta)) & 0 \\ 0 & 0 & L_f \end{bmatrix} \quad \text{(II. 13)}$$

With the neutral of the machine isolated, we have $i_h = 0$ and we can write:

$$\begin{bmatrix} v_\alpha \\ v_\beta \end{bmatrix} = R_S \begin{bmatrix} i_\alpha \\ i_\beta \end{bmatrix} + \frac{d}{dt}\begin{bmatrix} \psi_\alpha \\ \psi_\beta \end{bmatrix} \quad \text{(II. 14)}$$

II.3.4 Electrical equations of the machine in the d, q reference frame

Park's matrix is given by:

$$[P] = \frac{2}{3}\begin{bmatrix} \cos\theta & \cos\left(\theta - \frac{2\pi}{3}\right) & \cos\left(\theta + \frac{2\pi}{3}\right) \\ -\sin\theta & -\sin\left(\theta - \frac{2\pi}{3}\right) & -\sin\left(\theta + \frac{2\pi}{3}\right) \\ \frac{1}{2} & \frac{1}{2} & \frac{1}{2} \end{bmatrix} \quad \text{(II. 15)}$$

The calculation of the inverse of $[P]$ is obtained as:

$$[P]^{-1} = \begin{bmatrix} cos\,\theta & -sin\,\theta & 1 \\ cos\left(\theta - \frac{2\pi}{3}\right) & -sin\left(\theta - \frac{2\pi}{3}\right) & 1 \\ cos\left(\theta + \frac{2\pi}{3}\right) & -sin\left(\theta + \frac{2\pi}{3}\right) & 1 \end{bmatrix} \quad \text{(II. 16)}$$

If we project all the quantities into the d, q reference frame linked to the rotor **(Figure II-4)** using the Park's transformation, we write in the general case:

$$\begin{bmatrix} x_a \\ x_b \\ x_c \end{bmatrix} = [P]^{-1}\begin{bmatrix} x_d \\ x_q \\ x_h \end{bmatrix} \quad \text{(II. 17)}$$

The equation stated in (II.3) becomes then:

$$[P]^{-1}\left[V_{dqh}\right] = [R_S][P]^{-1}\left[I_{dqh}\right] + [P]^{-1}\frac{d\left[\psi_{dqh}\right]}{dt} + \frac{d[P]^{-1}}{dt}\left[\psi_{dqh}\right] \quad \text{(II. 18)}$$

where $[X_{dqh}]$ denotes any vector of quantities expressed in the rotor-related reference frame.

The multiplication of the two members of (II.18) by $[P]$ yields:

$$\left[V_{dqh}\right] = [R_s]\left[I_{dqh}\right] + \frac{d\left[\psi_{dqh}\right]}{dt} + P\omega_m[P]\frac{d[P]^{-1}}{d\theta}\left[\psi_{dqh}\right] \qquad (II.19)$$

where: $[P]\frac{d[P]^{-1}}{d\theta} = \begin{bmatrix} 0 & -1 & 0 \\ 1 & 0 & 0 \\ 0 & 0 & 0 \end{bmatrix}$

We finally get the following equations [63]:

$$\left[V_{dqh}\right] = [R_s]\left[I_{dqh}\right] + \begin{bmatrix} L_d & 0 & 0 \\ 0 & L_q & 0 \\ 0 & 0 & L_h \end{bmatrix}\frac{d\left[I_{dqh}\right]}{dt} + P\omega_m \begin{bmatrix} 0 & -L_q & 0 \\ L_d & 0 & 0 \\ 0 & 0 & 0 \end{bmatrix}\left[I_{dqh}\right] \qquad (II.20)$$

with:

$$\begin{cases} L_d = L_f + \frac{3}{2}(L_0 + L_2) \\ L_q = L_f + \frac{3}{2}(L_0 - L_2) \\ L_h = L_f \end{cases}$$

With the neutral of the machine isolated, which implies naturally $i_h = 0$, we can write:

$$\begin{bmatrix} v_d \\ v_q \end{bmatrix} = \begin{bmatrix} R_s & -P\omega_m L_q \\ P\omega_m L_d & R_S \end{bmatrix}\begin{bmatrix} i_d \\ i_q \end{bmatrix} + \begin{bmatrix} L_d & 0 \\ 0 & L_q \end{bmatrix}\frac{d}{dt}\begin{bmatrix} i_d \\ i_q \end{bmatrix} \qquad (II.21)$$

II.3.5 Mechanical equations

The calculation of the electromagnetic torque of the machine is based on the knowledge of the total instantaneous power $P_t(t)$, i.e.:

$$P_t = \frac{3}{2}R_S\left(i_d^2 + i_q^2\right) + \frac{3}{2}\left(\frac{d\psi_d}{dt}i_d + \frac{d\psi_q}{dt}i_q\right) + \frac{3}{2}P\omega_m\left(\psi_d i_q - \psi_q i_d\right) \qquad (II.22)$$

Considering that:

$P_j = \frac{3}{2}R_s\left(i_d^2 + i_q^2\right)$ represents the Joule effect losses in the stator windings.

$P_w = \frac{3}{2}\left(\frac{d\psi_d}{dt}i_d + \frac{d\psi_q}{dt}i_q\right)$ denotes the variations of the magnetic energy stored in the machine.

$P_e = \frac{3}{2} P \omega_m (\psi_d i_q - \psi_q i_d)$ represents the electrical power transformed into mechanical power inside the machine, or the electromagnetic power. The electromagnetic power results from the interaction of a flux term and a current term.

The electromagnetic torque equation is therefore:

$$T_e = \frac{P_e}{\omega_m} = \frac{3}{2} P(\psi_d i_q - \psi_q i_d) = \frac{3}{2} P(L_d - L_q) i_d i_q \qquad \text{(II. 23)}$$

Taking into account the total inertia J, the viscous friction coefficient B_m and the load torque T_L, the equation of motion is given by:

$$J \frac{d\omega_m}{dt} + B_m \omega_m = T_e - \mathrm{T}_L \qquad \text{(II. 24)}$$

The state model of the Syn-RM in the d, q frame is finally written:

$$\frac{d}{dt}\begin{bmatrix} i_d \\ i_q \\ \omega_m \\ \theta_m \end{bmatrix} = \begin{bmatrix} \frac{-R_s}{L_d} i_d + \frac{P L_q}{L_d} i_q \omega_m \\ \frac{-R_s}{L_q} i_q - \frac{P L_d}{L_q} i_d \omega_m \\ \frac{\frac{2}{2} P(L_d - L_q) i_d i_q}{J} - \frac{B_m}{J} \omega_m - \frac{\mathrm{T}_L}{J} \\ P \omega_m \end{bmatrix} + \begin{bmatrix} \frac{1}{L_d} & 0 \\ 0 & \frac{1}{L_q} \\ 0 & 0 \\ 0 & 0 \end{bmatrix} \begin{bmatrix} v_d \\ v_q \end{bmatrix} \qquad \text{(II. 25)}$$

The system of equations (II.25) is nonlinear because of the products between the currents i_d, i_q and the mechanical speed ω_m and also between the two currents. However, in most cases, the mechanical time constant is very large compared to the electrical time constants so that one can consider the two subsystems, electrical and mechanical, decoupled. Thus, the speed is considered constant during the transient current regimes, and it only remains to consider the non-linearity due to the product $i_d\ i_q$.

II.3.6 Syn-RM model with magnetic saturation and iron losses

Ferromagnetic materials with nonlinear magnetic characteristics are an important part of all electrical machines, and when the total magnetomotive force in the machine increases, saturation of the ferromagnetic parts occurs. This leads to a variation of the stator and rotor inductances, which must be taken into account in the motor model. The iron losses are also considered by adding

a shunt resistor in both direct and quadrature equivalent circuits. Different models have been proposed to account for these effects, including lookup tables for the iron loss resistance and direct/quadrature inductances [64], [65]. In this thesis, the Syn-RM dynamic model utilized was treated as an approximation of reality. The simulation incorporated lookup tables to represent the inductance parameters and iron losses resistor, as detailed in Table A-2 in appendix.

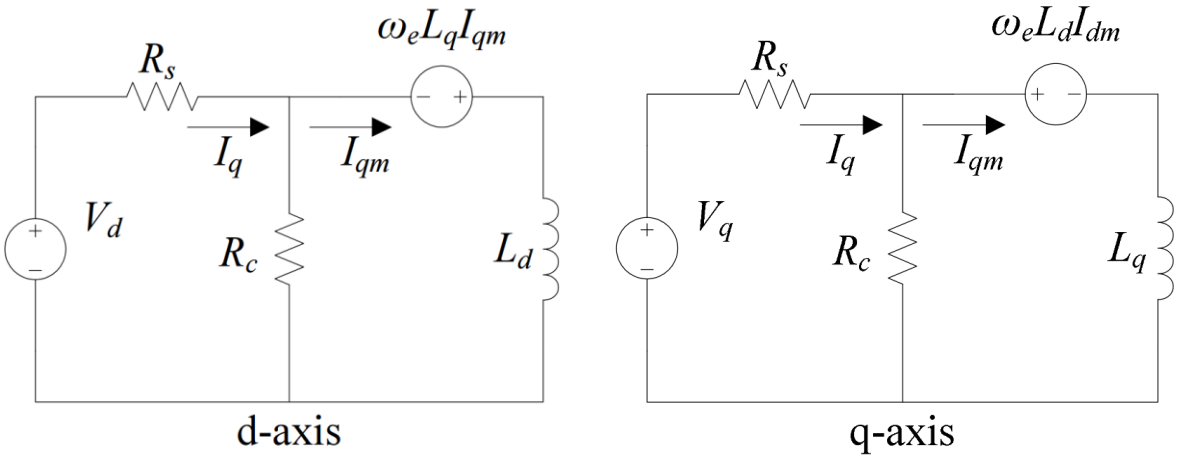

Figure II-5:Equivalent circuits of Syn-RM, considering iron losses, in the rotor reference frame.

In order to consider the saturation effect in the Syn-RM, it is necessary to assume that the inductances along the *d* and *q* axes are influenced by the current. It is important to note that the saturation effect in the *d* axis is expected to differ significantly from that in the *q* axis due to the distinct nature of their magnetic paths. In the *d* axis, the magnetic path is primarily composed of iron and is sensitive to excitation, whereas in the *q* axis, the magnetic path is primarily composed of air and is not sensitive to excitation. As a result, an unequal saturation effect occurs in the *d* and *q* axes as the current increases [64].

As illustrated in **Figure II-5**, taking into account magnetic saturation, new current terms are derived, namely i_{dm} and i_{qm}, which represent the torque-producing currents along the *d* and *q* axes, and they differ from the measured currents i_d, i_q . Measuring the iron loss resistance R_c during the transition state is challenging, so it is disregarded in the steady state. As a result, the relationship between stator currents and torque currents are represented as:

$$i_d = i_{dm} - \frac{1}{R_c}\left(\omega_e L_q i_{qm}\right) \tag{II.26}$$

$$i_q = i_{qm} - \frac{1}{R_c}\left(\omega_e L_d i_{dm}\right) \tag{II.27}$$

Substituting (II.26) and (II.27) in (II.25), the new Syn-RM model equations are obtained as follows.

$$\frac{d}{dt}\begin{bmatrix} i_{dm} \\ i_{qm} \\ \omega_m \\ \theta_m \end{bmatrix} = \begin{bmatrix} \frac{-R_s}{L_d} i_{dm} + \frac{P L_q}{L_d} i_{qm}\omega_m \\ \frac{-R_s}{L_q} i_{qm} - \frac{P L_d}{L_q} i_{dm}\omega_m \\ \frac{\frac{2}{2} P\left(L_d - L_q\right) i_{dm} i_{qm}}{J} - \frac{B_m}{J}\omega_m - \frac{\mathrm{T}_L}{J} \\ P\omega_m \end{bmatrix} + \begin{bmatrix} \frac{1}{L_d} & 0 \\ 0 & \frac{1}{L_q} \\ 0 & 0 \\ 0 & 0 \end{bmatrix} \begin{bmatrix} v_d \\ v_q \end{bmatrix} \tag{II.28}$$

II.4 Syn-RM power converter modeling

The grid power is converted to controlled ac power using AC-to-AC converter for electric drive applications. These AC-to-AC converters can be single-stage power converters using matrix converters or a rectifier stage followed by a DC-to-AC inverter. The main idea behind the usage of power converters for the drives is to create a controlled power supply from a fixed-frequency and fixed-voltage source with high efficiency. An ideal converter based on power electronic semiconductor devices is used as a switch which has:

- zero voltage drop across the switch when turned on.
- zero leakage current through the switch when turned off.
- zero turn-on and turn-off time.

This ensures that the ideal power electronics devices have no conduction, blocking, and switching losses. Therefore, the power converters with ideal components are supposed to have 100 % efficiency. However, it is not practical to get an ideal component, and the power converters are made with components whose characteristics are close to ideal to increase efficiency. As the cost of these devices and digital controller is decreasing, the usage of the power converters is increasing for drives' applications. There are several types of power converters which are used in the AC drives applications. In this chapter, the DC–AC three-phase voltage source inverters are discussed,

as they are the most commonly used power converters for the electric drive systems, and the two-level inverters, which are used for low-voltage drives, are discussed in sub-section **II.4.1**. These inverters are a source of variable voltage and frequency AC supply if the output of the inverters is Pulse Width Modulated (PWM). Several discussions on the pulse width modulation (PWM) method are available in literature. In this chapter, the most popular PWM methods - sinusoidal PWM and the Space Vector (SVPWM) - are discussed. The main focus is given on the simple implementation of these methods along with their relation with the theory, due to the their simple implementation, Hysteresis current controllers has been often employed within the AC drives control scheme. In this setup, inverters pulses are generated from the hysteresis comparators, which aims to maintain the current tracking error within the desired bandwidth [66].

II.4.1 Three-phase two-level inverter

For converting DC power to a controllable AC power, several DC–to-AC power inverters are available; among them, the two-level inverter (**Figure II-6)**. A phase of the AC side can be connected to either the positive DC-link terminal if the top device of that phase is turned on or the negative DC-link terminal if the bottom device of that phase is turned on. Therefore, the pole voltage of a phase is given by.

$$v_{x\mathrm{O}} = \begin{cases} V_{\mathrm{dc}} & \text{if top device of phase } x \text{ is turned on} \\ -V_{\mathrm{dc}} & \text{if bottom device of phase } x \text{ is turned on} \end{cases}$$

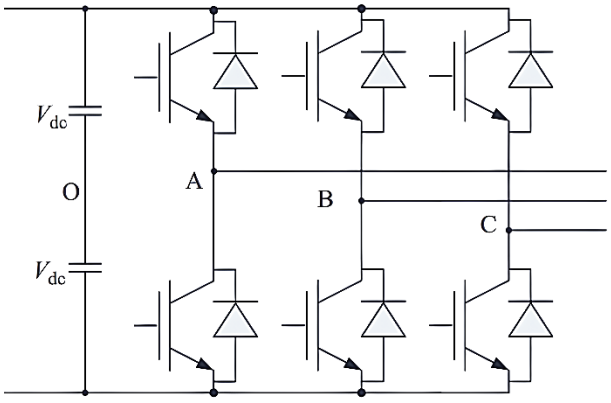

Figure II-6: Two-level inverter.

where $x = \{\mathrm{A}, \mathrm{B}, \mathrm{C}\}$, and V_{dc} is the dc-link voltage. As the pole of the ac side can have two levels, this inverter is called as the two-level inverter. Both devices in a phase should never be turned on simultaneously as it will short the dc power supply. Using this constraint, the two-level three-phase

inverter can have $2^3 = 8$ different switching states as listed in Table **II.1**. Each state is denoted by combination of plus (+) or minus (-) signs. The plus and minus signs denote that the pole voltage of that particular phase is +Vdc and -Vdc, respectively.

These switching states are used to generate a set of required three-phase balanced output voltage as given by:

$$\begin{aligned} v_{\mathrm{A}} &= V_m \cos(\omega t) \\ v_{\mathrm{B}} &= V_m \cos\left(\omega t - \frac{2\pi}{3}\right) \\ v_{\mathrm{C}} &= V_m \cos\left(\omega t + \frac{2\pi}{3}\right) \end{aligned} \tag{II.29}$$

where V_m is the peak of the desired phase voltage with fundamental frequency denoted by ω .

Although the converter is not able to generate the exact three-phase balanced output voltages, its output voltage can be modulated in a way that it approximates these balanced three-phase voltages. For that, several modulation techniques are used in literature. Among them, the most popular methods are sinusoidal PWM (SPWM) and Space Vector PWM (SVPWM) techniques [67].

II.4.2 Current controlling methods for voltage inverters

The role of the control device is to ensure self-steering and regulation of the currents, with the aim of keeping the actual currents measured at the machine phases as close as possible to their references. To achieve this, three techniques can be used:

- Hysteresis current control
- Sinusoidal Pulse Width Modulation (SPWM)
- Space Vector Modulation (SVM)

II.4.2.1 Hysteresis current control

This method, certainly the simplest, has often been used to supply AC machines. **Figure II-7** shows the principal diagram for this technique, where the current references are sinusoidal. This strategy uses three independent regulators, one per phase, and when the instantaneous current in a phase deviate from its sinusoidal reference, fixed by the regulator hysteresis, switching is imposed on the switches of the corresponding inverter arm, so as to keep these currents always within a band surrounding these references. Currents ripple are dependent to the value of the hysteresis bandwidth.

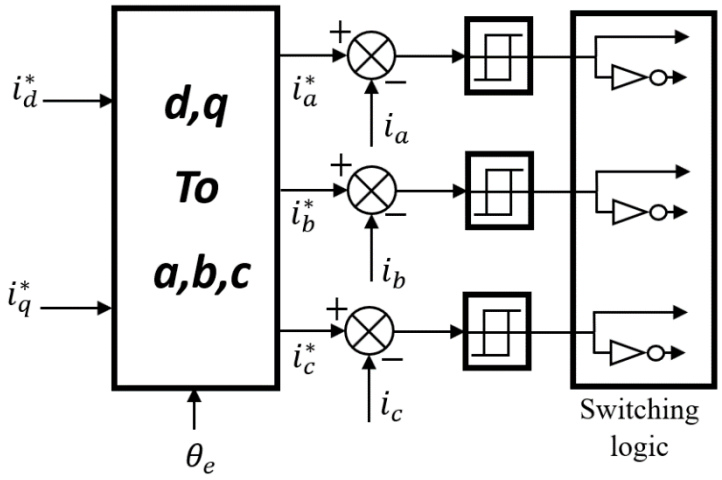

Figure II-7: Current control scheme based on hysteresis comparators.

II.4.2.2 Sinusoidal pulse width modulation

The SPWM technique is the most popular PWM technique due to its simplicity. In this method, the three-phase normalized sinusoidal reference signals are obtained by scaling the required AC output voltage as given by:

$$\begin{aligned} v_{\mathrm{A,ref}} &= m_a \cos(\omega t) \\ v_{\mathrm{B,ref}} &= m_a \cos\left(\omega t - \frac{2\pi}{3}\right) \\ v_{\mathrm{C,ref}} &= m_a \cos\left(\omega t + \frac{2\pi}{3}\right) \end{aligned} \qquad (\mathrm{II}.30)$$

where $m_a = V_m/V_{\mathrm{dc}}$ is known as modulation index.

These reference signals are compared with a high-frequency triangular carrier signal, as shown in **Figure II-8**. If the reference signal of a phase is higher or lower than the carrier signal, the top or bottom switch is turned on, respectively. Due to this arrangement of switching on/off, the pole voltages of the phases are obtained as shown in **Figure II-9**, which is valid for $0 < \omega t < \pi/3$. The resultant waveform is shown for one carrier cycle, also known as the switching period, where the reference signals are sampled and assumed to be constant. It can be seen that the applied sequence of the switching states in the carrier period is $(---) \rightarrow (+--) \rightarrow (++-) \rightarrow (+++)$ and reverse. The pole voltage of phase A averaged over a switching period can be given by:

$$\langle v_{\mathrm{AO}} \rangle_{T_s} = V_{\mathrm{dc}} \frac{(2t_a - T_s)}{T_s} \qquad (\mathrm{II}.31)$$

Table II-1:Switching states of two-level inverter

Switching state	Pole voltage		
	Phase $\mathbf{A}(v_{\mathrm{AO}})$	Phase $\mathbf{B}(v_{\mathrm{BO}})$	Phase $\mathbf{C}(v_{\mathrm{CO}})$
---	$-V_{\mathrm{dc}}$	$-V_{\mathrm{dc}}$	$-V_{\mathrm{dc}}$
+--	$+V_{\mathrm{dc}}$	$-V_{\mathrm{dc}}$	$-V_{\mathrm{dc}}$
++-	$+V_{\mathrm{dc}}$	$+V_{\mathrm{dc}}$	$-V_{\mathrm{dc}}$
-+-	$-V_{\mathrm{dc}}$	$+V_{\mathrm{dc}}$	$-V_{\mathrm{dc}}$
-++	$-V_{\mathrm{dc}}$	$+V_{\mathrm{dc}}$	$+V_{\mathrm{dc}}$
--+	$-V_{\mathrm{dc}}$	$-V_{\mathrm{dc}}$	$+V_{\mathrm{dc}}$
+-+	$+V_{\mathrm{dc}}$	$-V_{\mathrm{dc}}$	$+V_{\mathrm{dc}}$
+++	$+V_{\mathrm{dc}}$	$+V_{\mathrm{dc}}$	$+V_{\mathrm{dc}}$

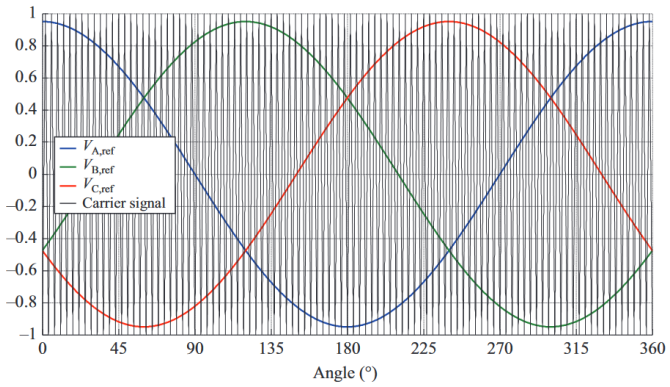

(a)

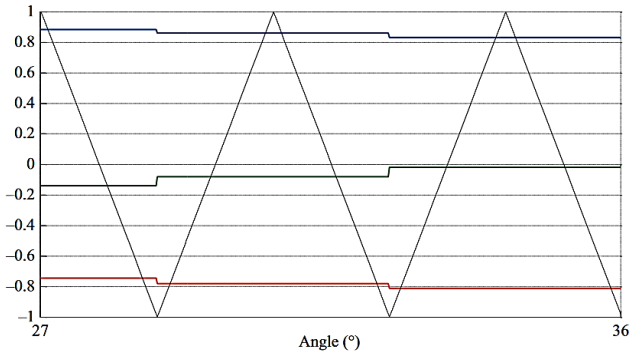

(b)

Figure II-8: Reference and carrier signals of sinusoidal PWM for: (a) a fundamental cycle; (b) Zoom-in of the cycle.

where T_s is the switching period, and $t_a$can be given by:

$$t_a = \frac{1 + v_{\mathrm{A,ref}}}{2} T_s \tag{II.32}$$

Using (II.31) and (II.32), the average value of phase A pole voltage is given by:

$$\langle v_{\mathrm{AO}} \rangle_{T_s} = V_{\mathrm{dc}} v_{\mathrm{A,ref}} \tag{II.33}$$

The pole voltage of phase A averaged over a switching period is proportional to the normalized reference signal. Similarly, phases B and C pole voltages averaged over a switching period are proportional to their respective normalized reference signals. If the reference signal is sinusoidally varying, the average pole voltage will also have sinusoidal variation. If the switching period is very small compared to the fundamental cycle, $T_s \ll 2\pi/\omega$, the fundamental component of the three-phase pole voltage will be equal to the required three phase balanced output voltage given by (II.29).

Equation (II.33) is valid for $m_a < 1$. Therefore, the maximum value of the peak voltage V_m for the AC-side output voltage that can be obtained from this method is V_{dc}.

II.4.2.3 Space Vector Modulation

The space vector finds its usage in explaining the rotating magnetic field due to three-phase balanced sinusoidal excitation current in the three-phase sinusoidal distributed winding in an AC machine [68]. The space vector, defined by its α- and β- components, describes the sinusoidal distribution of a variable in 'space'. For a three-phase variable (voltage, current, or any other electrical variable), the space vector is defined by:

$$\begin{aligned} \mathbf{F} &= f_\alpha + j f_\alpha \\ f_\alpha &= f_{\mathrm{A}} - \frac{f_{\mathrm{B}} + f_{\mathrm{C}}}{2} \\ f_\alpha &= \frac{\sqrt{3}}{2}(f_{\mathrm{B}} - f_{\mathrm{C}}) \end{aligned} \tag{II.34}$$

-

where α and β subscript describe the α - and β -components of the space vector. The voltage space vector components of the desired three-phase output voltage can be obtained by replacing (II.29) in (II.34), as given by

$$\begin{aligned} v_\alpha &= \frac{3}{2} V_m \cos(\omega t) \\ v_\beta &= \frac{3}{2} V_m \sin(\omega t) \end{aligned} \tag{II.35}$$

If the locus of the tip of the voltage space vector is plotted using (II.35) with respect to time, a circle is obtained. However, the two-level inverter cannot generate these voltage vectors. The space vectors that can be generated by the inverter can be obtained by replacing the voltage levels of the switching states of Table II.1 in (II.35). The resultant space vectors form the space vector diagram (SVD), as shown in **Figure II-9** [69]. The space vectors V1–V6 have the magnitude of $2\,V_{dc}$, and their tips are located at the corner of a hexagon displaced by 60°. These vectors are called active vectors. The space vector corresponding to two remaining switching states (+ + +) and (- - -) has zero magnitude. Therefore, it is known as zero vector. In other words, the zero vector can be realized by two switching states (it has two redundancies), and the active vectors can be realized by a unique switching state. The active vectors divide the SVD into six sectors identified by roman letters I–VI in **Figure II-10**. The vertices of a sector are the tip of the two active vectors and the zero vector. These vectors are used to approximate the desired voltage space vector, referred to as the reference vector. The reference vector can be obtained by sampling the reference signals of (II.30) in the switching period T_s and replacing the three-phase sampled reference signals in (II.34) after multiplying with V_{dc}.

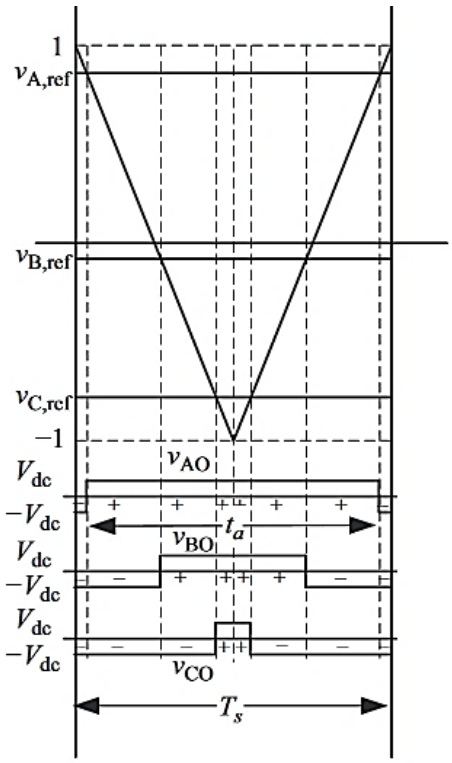

Figure II-9: Reference signals, carrier signal, and corresponding pole voltage for sinusoidal PWM.

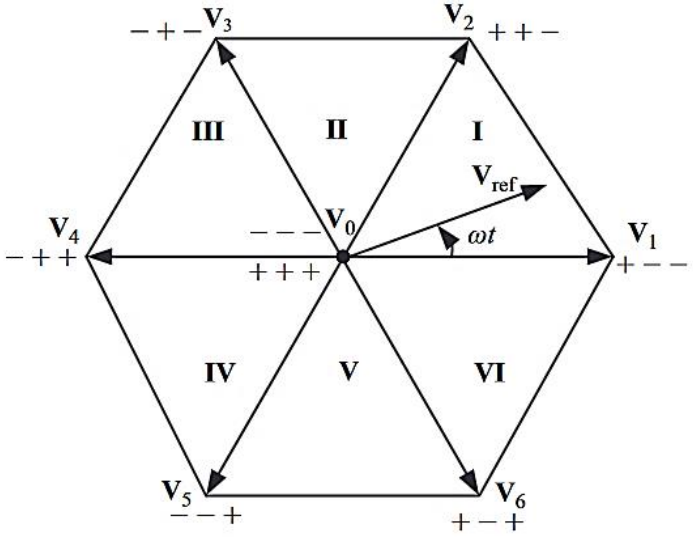

Figure II-10: Space vector diagram of a two-level inverter.

The time for which these switching states need to be applied depends on the magnitude and angle of the desired reference vector, and it is known as the dwell time for that particular switching state. The dwell times for the switching states (+ - -) and (+ + -) are given by:

$$\text{and} \quad T_1 = \frac{V_{ref} \sin\left(\left(\frac{\pi}{3}\right) - \theta\right)}{2V_{dc} \sin\left(\frac{\pi}{3}\right)} T_s \qquad (\text{II}.36)$$
$$T_2 = \frac{V_{ref} \sin(\theta)}{2V_{dc} \sin\left(\frac{\pi}{3}\right)} T_s,$$

respectively. V_{ref} and θ are the magnitude and angle of the reference vector. The dwell time T_1 and T_2 are determined by equating the average of the α- and β-components of the active vectors, V1 and V2, to the α- and β-components of the desired reference vector, respectively. The remaining time in the switching period is used for the application of the switching states (+ + +) and (- - -) to realize the zero vector. In conventional SVPWM, the dwell time for state (+ + +) (T_7) and for state (- - -) (T_0) are equal, as given by [66]:

$$T_0 = T_7 = \frac{1}{2}(T_s - T_1 - T_2) \qquad (\text{II}.37)$$

Table II-2:Switching sequence for SVPWM.

Sector	Switching sequence
I	$(-\,-\,-) \rightarrow (+\,-\,-) \rightarrow (+\,+\,-) \rightarrow (+\,+\,+)$ and reverse
II	$(-\,-\,-) \rightarrow (-\,+\,-) \rightarrow (+\,+\,-) \rightarrow (+\,+\,+)$ and reverse
III	$(-\,-\,-) \rightarrow (-\,+\,-) \rightarrow (-\,+\,+) \rightarrow (+\,+\,+)$ and reverse
IV	$(-\,-\,-) \rightarrow (-\,-\,+) \rightarrow (-\,+\,+) \rightarrow (+\,+\,+)$ and reverse
V	$(-\,-\,-) \rightarrow (-\,-\,+) \rightarrow (+\,-\,+) \rightarrow (+\,+\,+)$ and reverse
VI	$(-\,-\,-) \rightarrow (+\,-\,-) \rightarrow (+\,-\,+) \rightarrow (+\,+\,+)$ and reverse

II.5 Control simulation of Syn-RM

II.5.1 Direct torque control of Syn-RM

The basic principle of the DTC is to directly control the motor flux vector along the predetermined trajectory at the predetermined speed. Any deviation in the actual motor flux or torque from the reference trajectories is detected by set of hysteresis controllers, which directly select an appropriate switching vector in such way that the deviation is minimized. DTC directly generates the command signals for inverter phases. The flux vector orientation is done in the stationary reference frame, thus eliminating the need for speed/position sensors. The ultimate result of this simplification enables to obtain faster dynamic response.

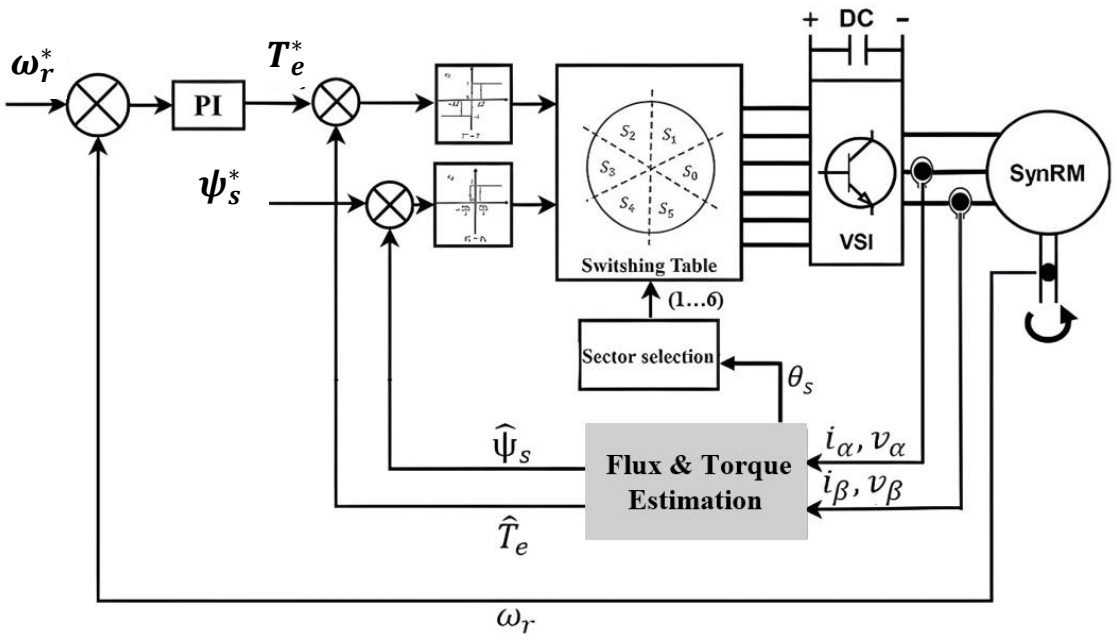

Figure II-11: Schematic block of conventional Direct Torque Control (DTC).

Figure II-11 shows the basic structure of conventional DTC. This technique consists of controlling torque and flux separately. Speed PI controller generates the electromagnetic torque reference T_e^* which is compared with the estimated value $\widehat{T_e}$, as well as the flux control. The reference value ψ_e^* is compared with the estimated flux $\widehat{\psi_s}$, and two hysteresis comparators are used for errors judgment, generating three command law possibilities for torque and two for flux. The possible results of the comparators are written in (II.38):

$$\begin{cases} CT_e^* = 1, \text{ for } \varepsilon_{Te} \rangle H_{Te} \\ CT_e^* = 0, \text{ for } H_{Te} \rangle \varepsilon_{Te} \rangle - H_{Te} \\ CT_e^* = -1, \text{ for } \varepsilon_{Te} \langle -H_{Te} \\ C\psi_s^* = 1, \text{ for } \varepsilon_{\psi s} \rangle H_{\psi s} \\ C\psi_s^* = -1, \text{ for } \varepsilon_{\psi s} \langle -H_{\psi s} \end{cases} \quad (\text{II.38})$$

The conventional flux estimation is based on voltage and current quantities in the stator reference frame α, β and can be expressed as:

$$\begin{cases} \psi_\alpha = \int (V_\alpha - i_\alpha R_s) dt \\ \psi_\beta = \int (V_\beta - i_\beta R_s) dt \end{cases} \quad (\text{II.39})$$

The estimated flux to be introduced into the DTC loop can be stated from (II.39) as:

$$\hat{\Psi}_s = \sqrt{\hat{\psi}_\alpha^2 + \hat{\psi}_\beta^2} \quad (\text{II.40})$$

The flux angle can be extracted from Equations (II.39) as:

$$\widehat{\theta_s} = arctan\frac{\psi_\beta}{\psi_\alpha} \qquad (II.41)$$

The electromagnetic torque used in the DTC algorithm is expressed as a function of the estimated flux in (II.39) as:

$$\widehat{T_e} = \frac{3}{2}P(\widehat{\psi_\alpha} i_\beta - \widehat{\psi_\beta} i_\alpha)$$

Table II-3 : DTC switching table

Sectors		**1**	**2**	**3**	**4**	**5**	**6**
Flux	Torque						
$C\psi_s^* = 1$	$CT_e^*=1$	V2 (110)	V3 (100)	V4 (101)	V5 (001)	V6 (011)	V1 (010)
	$CT_e^*=0$	V7 (111)	V0 (000)	V7 (111)	V0 (000)	V7 (111)	V0 (000)
	$CT_e^*=-1$	V6 (011)	V1 (010)	V2 (110)	V3 (100)	V4 (101)	V5 (001)
$C\psi_s^* = -1$	$CT_e^*=1$	V3 (100)	V4 (101)	V5 (001)	V6 (011)	V6 (010)	V2 (110)
	$CT_e^*=0$	V0 (000)	V7 (111)	V0 (000)	V7 (111)	V0 (000)	V7 (111)
	$CT_e^*=-1$	V5 (001)	V6 (011)	V1 (010)	V2 (110)	V3 (100)	V4 (101)

II.5.2 Field oriented control of Syn-RM

Field Oriented Control (FOC) is a control strategy used in electric motors to achieve high-performance operation. The principle of FOC is to control the torque and speed of the motor by decoupling the stator current into two components: one component that produces a magnetic field that rotates with the rotor, and another component that produces a magnetic field that is stationary with respect to the stator. The FOC technique involves transforming the three-phase AC voltage and current signals into two-phase signals, known as d-axis and q-axis components. The d-axis component represents the magnetic flux that is aligned with the rotor, while the q-axis component represents the magnetic flux that is perpendicular to the rotor. By controlling these two components separately, it becomes possible to control both torque and speed independently. This allows for precise control of motor performance, including high efficiency, low noise, and smooth operation.

Using direct Field Oriented Control (FOC) aims to regulate the two currents i_d and i_q while neglecting the coupling terms $e_d$and e_q. These coupling terms act as disturbances to be compensated, as they are proportional to the Back Electromotive Force (EMF). These terms are added to the output of the current controllers to obtain the control voltages v_d^* and v_q^* . The coupling terms are defined as follows:

$$\begin{aligned} e_d &= -w_e i_q^* L_q \\ e_q &= w_e i_d^* L_d \end{aligned} \qquad \text{(II. 45)}$$

As depicted in **Figure II.20**, torque and flux are indirectly controlled by means of i_d, i_q currents control, thus no flux or torque estimation is required. First, i_q reference value is obtained from speed *PI* controller, and then it is compared to the measured value. The *PI* cascade controller acts to eliminate the error e_{iq}. On the other hand i_d current is controlled as well, where its reference is fixed to a constant value. *PI is* used within the control loop. i_d reference value can be generated in others control modes such as Maximum Torque Per Ampere (MTPA) and/or Flux Weakening (FW) according to the flux reference at the actual operating speed, where optimal drive control is required for a wide speed region. Voltage references v_d^*, v_q^* are generated as,

$$\left.\begin{aligned} v_d^* &= C_d^* + e_d \\ v_q^* &= C_q^* + e_q \end{aligned}\right\} \qquad \text{(II. 45)}$$

where,

C_d^*, C_q^* are d, q currents controllers outputs defined as:

$$C_d^* = (i_d^* - i_d) * H(p)_d \qquad \text{(II. 46)}$$

$$C_q^* = \left(i_q^* - i_q\right) * H(p)_q \qquad \text{(II. 47)}$$

$H(p)_d$, $H(p)_q$ are d, q PI controller transfer functions respectively. i_d^*, i_q^* are current controllers commands. Inverse Park's transformation is used to transform voltage reference quantities v_d^*, v_q^* into stator reference quantities v_a, v_b, v_c to be introduced to PWM block as shown in **Figure II.12**

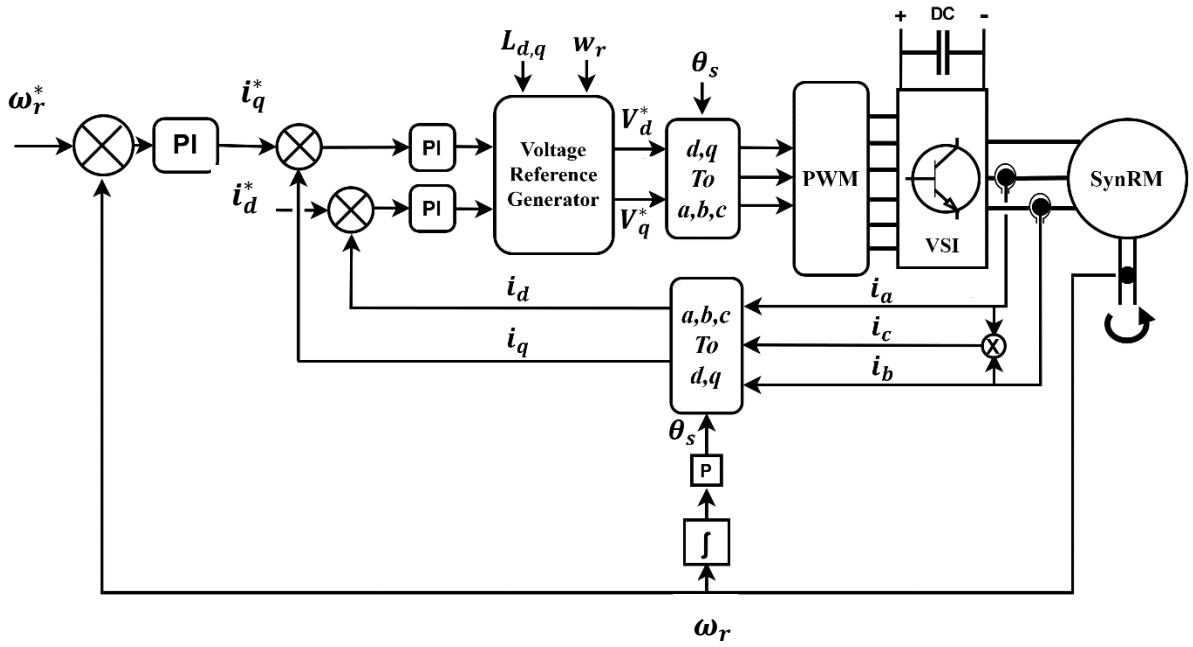

Figure II-12: Overall field-oriented control schematic of Syn-RM.

II.5.3 Space vector modulation-based DTC

DTC-SVM, a control technique applied in motor control, particularly for Syn-RM, is an improvement over the conventional DTC algorithm, which is plagued by torque ripple. It aims to minimize torque ripple by precisely aligning the stator flux through the use of space vector modulation (SVM), as depicted in **Figure II-14**. This approach enables real-time adjustments to the torque angle, leading to more stable control and reduced torque ripple. Additionally, the estimation of stator flux position and magnitude relies on motor parameters and current.

In this technique, torque and flux control are seamlessly integrated with the SVM technique to achieve a constant switching frequency while mitigating current distortion. In this approach, a single PI controller is dedicated to predicting the torque angle $\Delta\delta_T$ between actual and reference flux vector as illustrated in **Figure II-13**, which is used for flux references calculation ψ_α^* , ψ_β^* , while considering the flux reference value ψ_s^*. This can be expressed as follows:

$$\psi_\alpha^* = \psi_s^* \cos(\theta_s + \Delta\delta_T)$$
$$\psi_\beta^* = \psi_s^* \sin(\theta_s + \Delta\delta_T)$$

The flux error is stated as:

$$\psi_\alpha = \psi_\alpha^* - \widehat{\psi_\alpha}$$
$$\varepsilon\psi_\beta = \psi_\beta^* - \widehat{\psi_\beta}$$

Finally, voltage references can be expressed as,

$$v_\alpha^* = R_s i_\alpha + \frac{\varepsilon\psi_\alpha}{T_s}$$
$$v_\beta^* = R_s i_\beta + \frac{\varepsilon\psi_\beta}{T_s}$$

As depicted in **Figure II-14**, the inverter switching signals are generated using the voltage references v_α^* , v_β^* based on the SVM technique outlined in **Chapter I**.

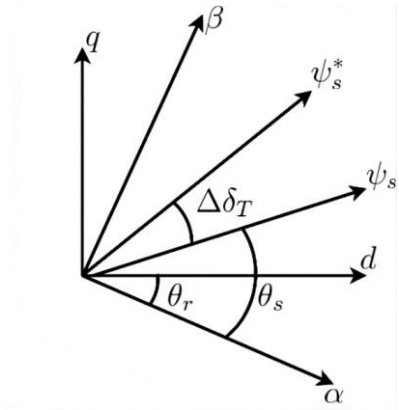

Figure II-13 : Flux vector diagram of Syn-RM.

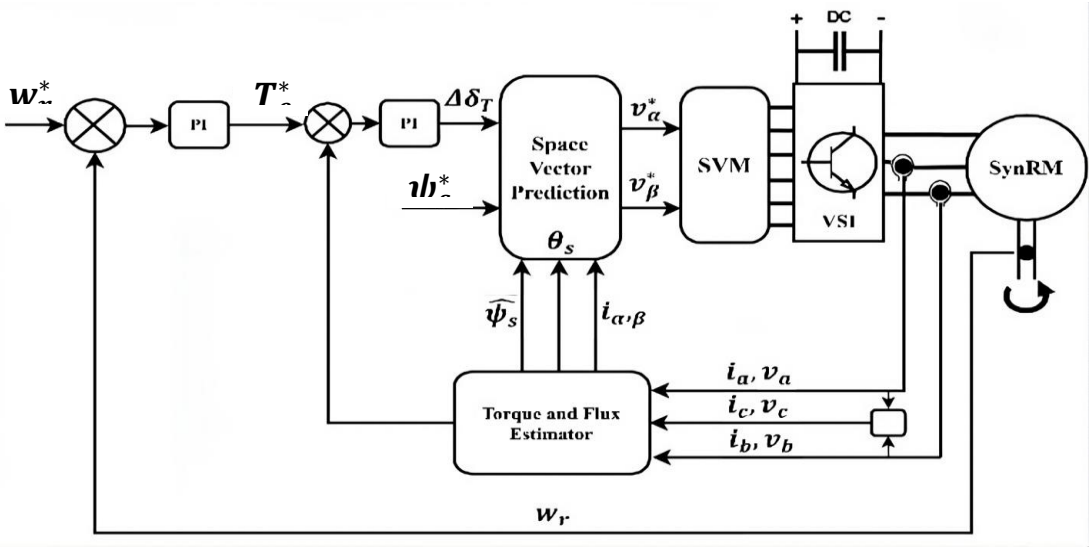

Figure II-14 : Overall DTC-SVM schematic of Syn-RM.

II.5.4 Simulation results

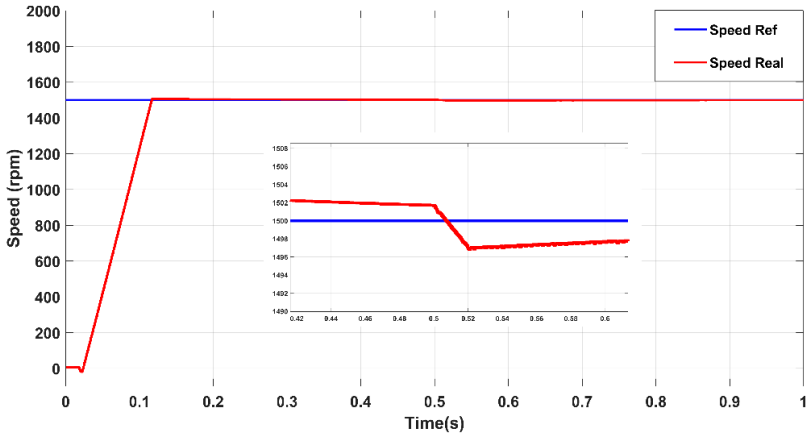

Figure II-15 : DTC Speed responses, full load applied at 0.5 (s).

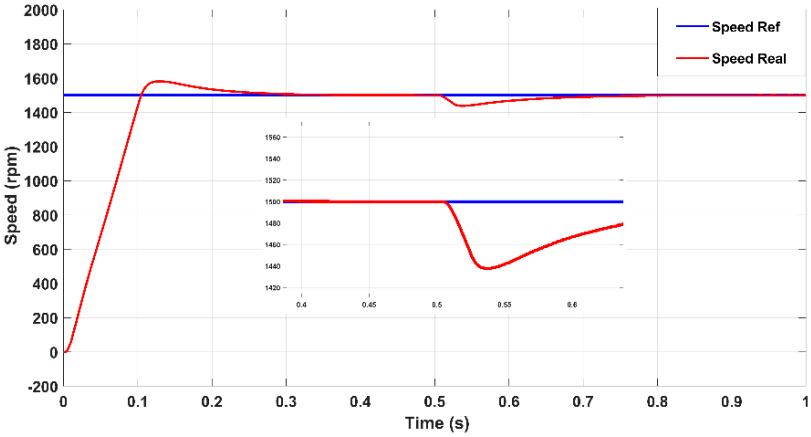

Figure II-16:FOC Speed response, full load applied at 0.5 (s).

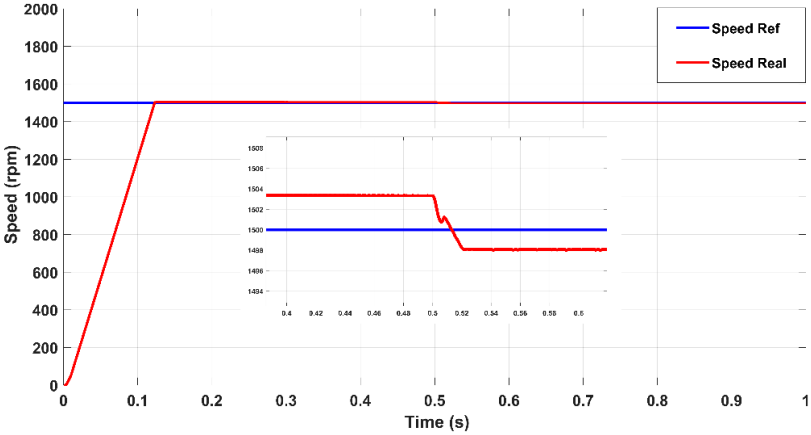

Figure II-17 : DTC-SVM Speed response, full load applied at 0.5 (s).

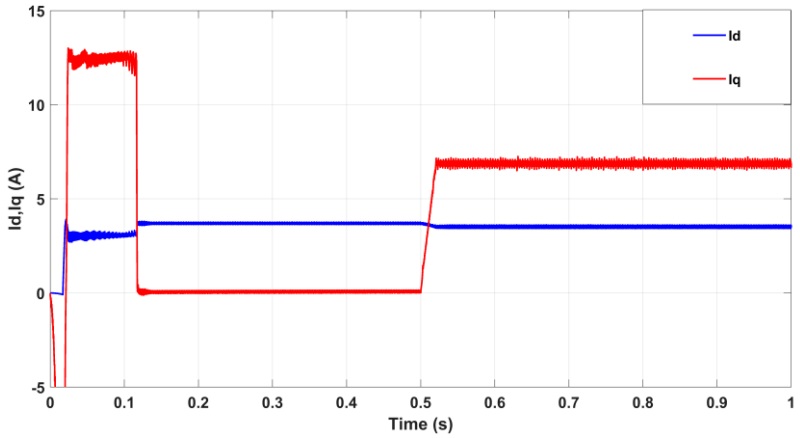

Figure II-18 : DTC i_d, i_q currents, full load applied at 0.5 (s).

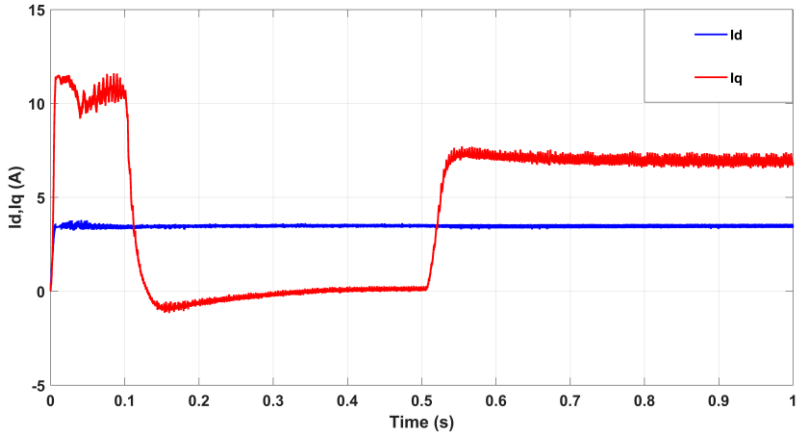

Figure II-19:FOC i_d, i_q currents, full load applied at 0.5 (s).

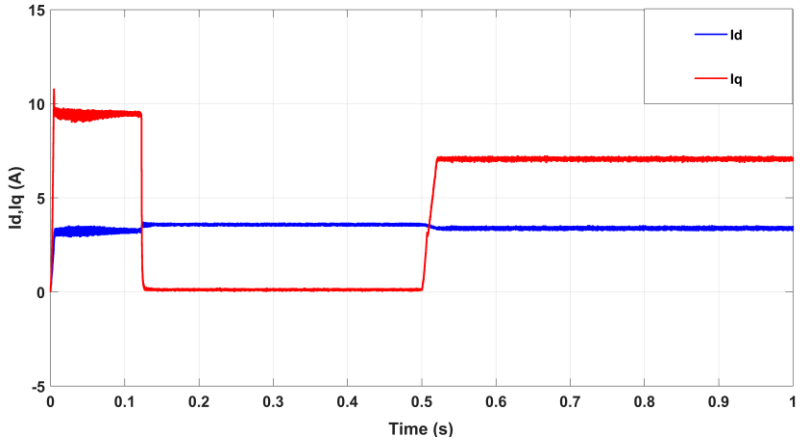

Figure II-20 :DTC-SVM i_d, i_q currents, full load applied at 0.5 (s).

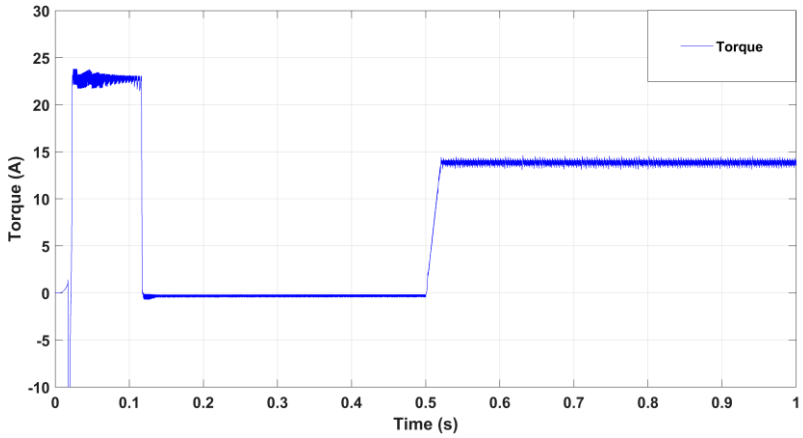

Figure II-21 : DTC Electromagnetic torque, full load applied at 0.5 (s).

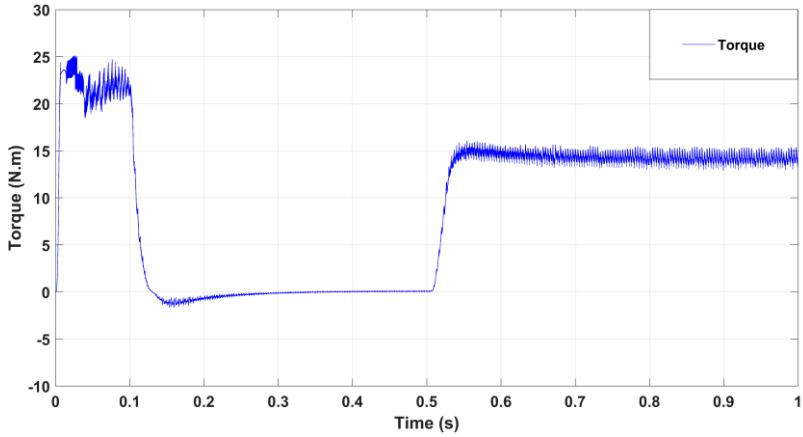

Figure II-22:FOC Electromagnetic torque, full load applied at 0.5 (s).

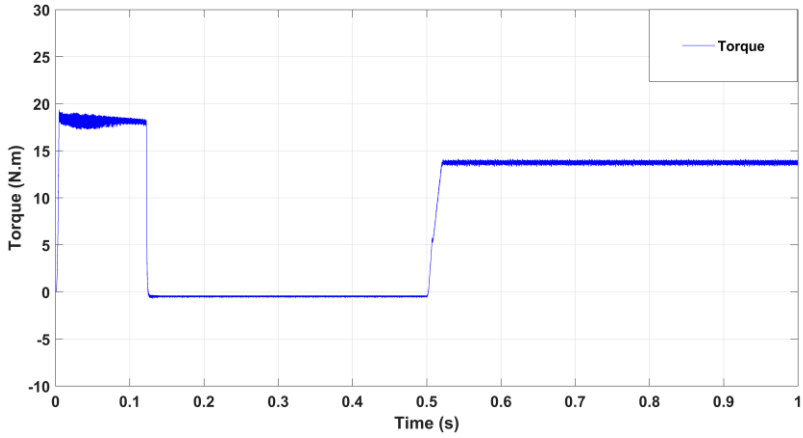

Figure II-23 : DTC-SVM Electromagnetic torque, full load applied at 0.5 (s).

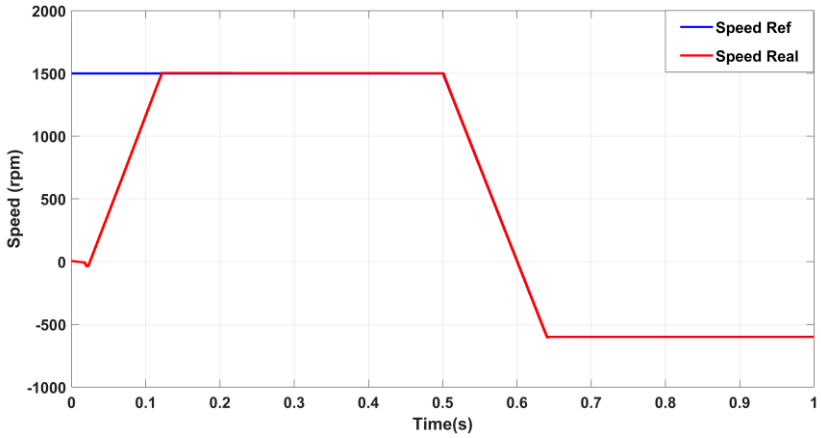

Figure II-24: DTC Speed response, at no load, speed reverse from 1500 rpm to -600 rpm.

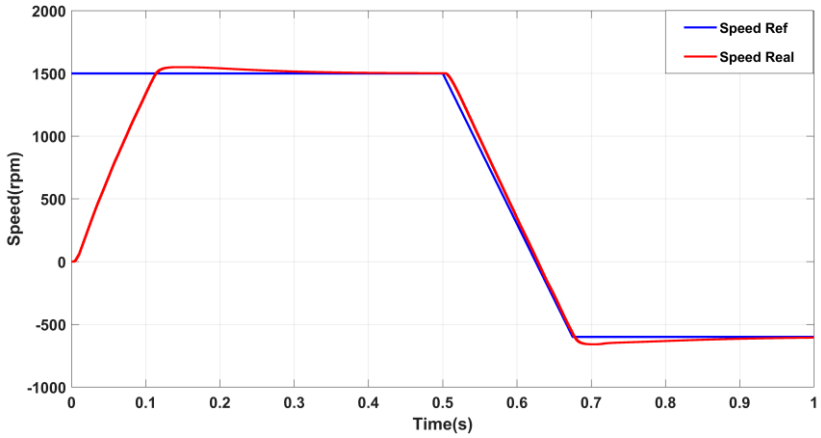

Figure II-25:FOC Speed response, at no load, speed reverse from 1500 rpm to -600 rpm.

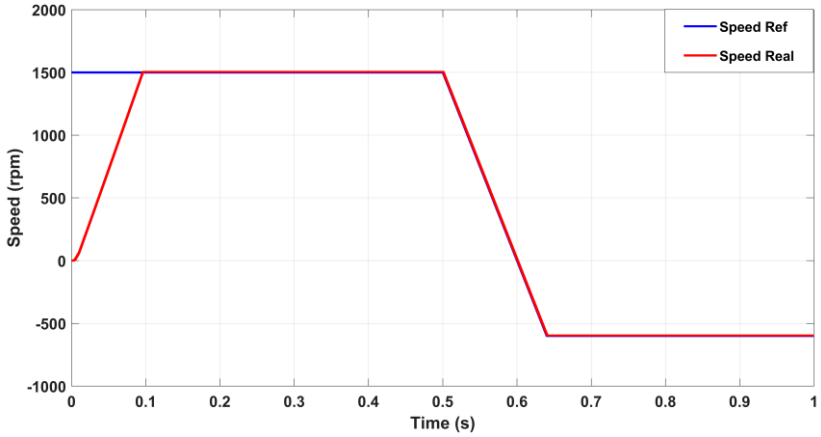

Figure II-26 : DTC SVM Speed response, at no load, speed reverse from 1500 rpm to -600 rpm.

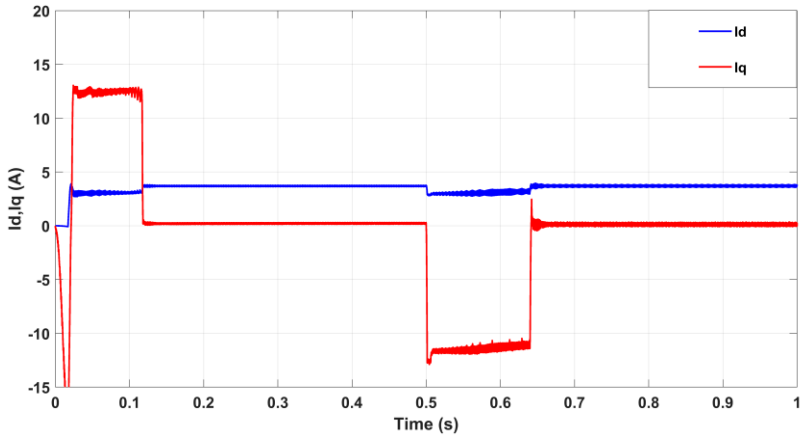

Figure II-27 : DTC i_d, i_qcurrents response, at no load, speed reverse from 1500 rpm to -600 rpm

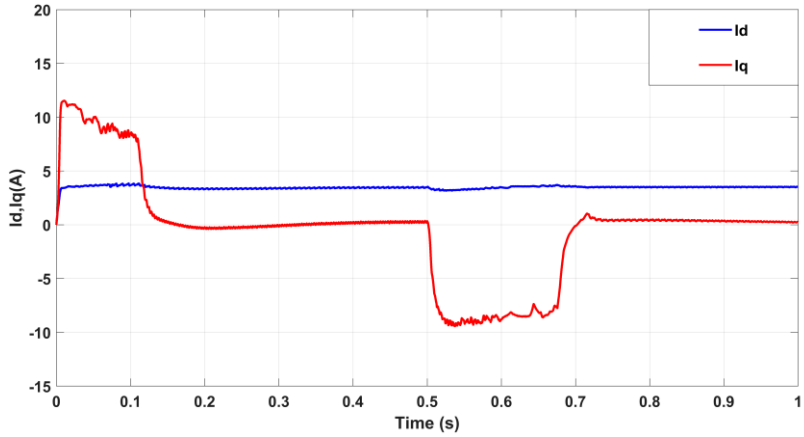

Figure II-28: FOC i_d, i_q currents response, at no load, speed reverse from 1500 rpm to -600 rpm.

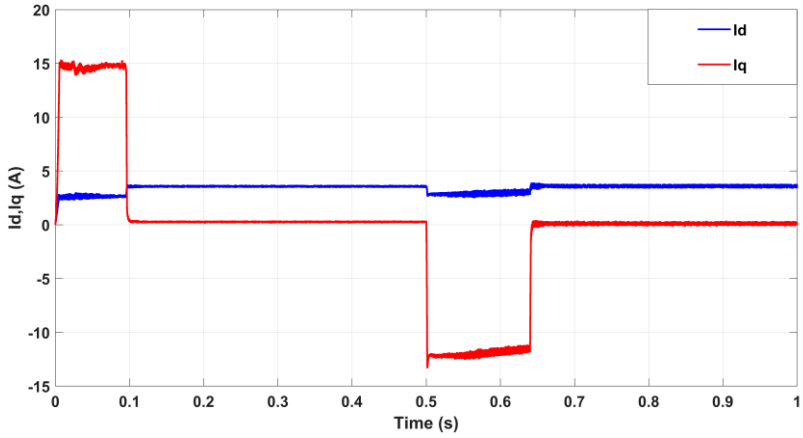

Figure II-29 : DTC-SVM i_d, i_q currents response, at no load, speed reverse from 1500 rpm to -600 rpm.

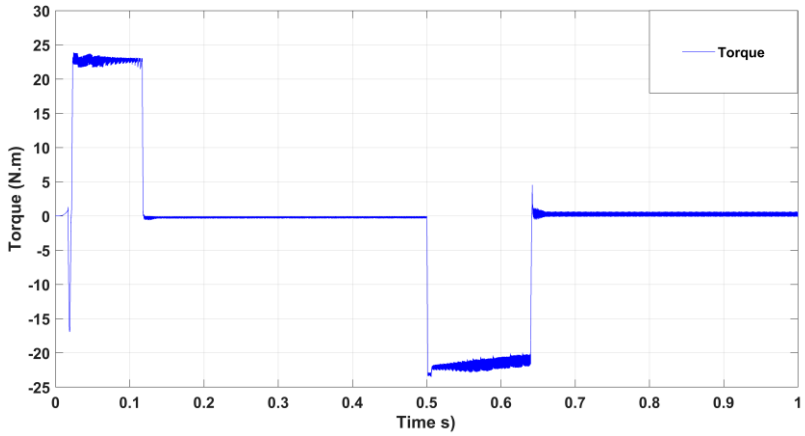

Figure II-30 : DTC Electromagnetic torque, at no load, speed reverse from 1500 to -600 rpm.

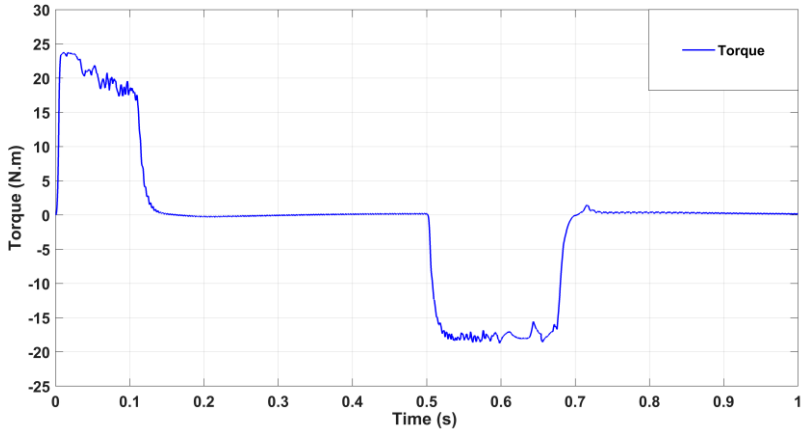

Figure II-31:FOC Electromagnetic torque, at no load, speed reverse from 1500 to -600 rpm.

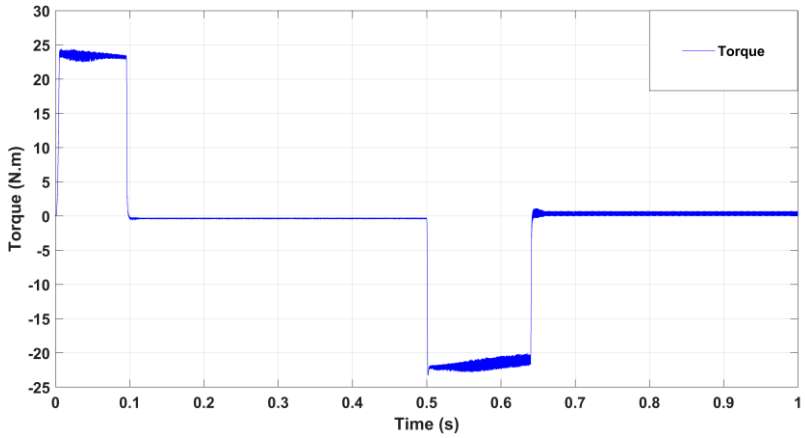

Figure II-32:DTC-SVM Electromagnetic torque, at no load, speed reverse from 1500 to -600 rpm.

II.5.5 Simulation results discussion

In order to evaluate the dynamic behavior of the Syn-RM with the afore-presented control techniques, two simulation scenarios were conducted in MATLAB/Simulink environment with the motor specifications mentioned in Table A-1 In appendix. Magnetic saturation and iron losses are included in the dynamic model. In the first scenario, the speed was raised from standstill up to rated speed (1500 rpm) then at 0.5 (s) full load was applied. In the second scenario, no-load test was performed where speed was reversed from 1500 rpm to -600 rpm.

II.5.5.1 Load change case

Figures II-15, II-16 and **II-17** exposes the speed responses. It can be clearly seen in **Figure II-15** and **Figure II-17** that DTC and DTC-SVM can handle the load variation. In contrast, in **Figure II-16** FOC speed response exhibited an overshoot during the transition phase of load torque. The use of FOC results in poor torque regulation presented as high torque ripple (**Figure II-22**) as compared to DTC and DTC-SVM in which torque response is smoother with less ripple as depicted in **Figure II-21** and **II-23**. i_d, i_q currents simulated responses are illustrated in **Figures II-18, II-19** and **II-20**. It becomes evident that the control of current is more effective with DTC-SVM control technique, thanks to the stable switching frequency, whereas in FOC technique i_d value remains constant (3.3 A) through the whole simulation duration, and i_q, varies with speed and load conditions. From the point of view of current distortion, DTC-SVM presents the best response as compared to DTC-Hys and FOC.

II.5.5.2 Speed change case

To delve deeper into the previously examined control methods for the Syn-RM, an additional simulation scenario has been conducted, where the motor was started without any load, and the speed was gradually raised to its rated value of 1500 rpm. Then, at t = 0.5 s, the speed was intentionally reduced and reversed, reaching -600 rpm in the opposite direction.

The traditional combination of Field-Oriented Control (FOC) and a standard PI regulator is well-matched for efficient operation within a defined operating condition. Nevertheless, its performance might not be optimal in every situation, potentially leading to transient overshooting, as illustrated in **Figure II-25** for speed response and **Figure II-28** for i_d, i_q currents. However, in steady-state operation, the performance of the Syn-RM is enhanced thanks to the incorporation of

back EMF compensation within the control loop. From the perspective of electromagnetic torque, the no-load simulation has demonstrated that DTC control exhibits an inherent limitation characterized by some fluctuations during the transition phase, even in the absence of any load torque, as evident in **Figures II-30** and **Figure II-32**. Conversely, in the case of FOC (**Figure II-31**), the level of ripple is significantly reduced compared to the other two strategies.

II.6 Enhanced DTC based control of Syn-RM.

Despite DTC being known for its simplicity, fast dynamic response, and robustness against parameter variations, one of the major drawbacks of conventional DTC is the high torque and flux ripple in steady-state operation. This ripple can cause undesirable effects such as acoustic noise, mechanical vibrations, and reduced efficiency. To address this issue, researchers have proposed various methods to improve DTC performance and reduce torque and flux ripples. One approach is to modify the switching table used in DTC to reduce the number of switching transitions and improve the accuracy of torque and flux estimation. Another approach is to incorporate advanced control techniques such as model predictive control (MPC), sliding mode control (SMC), or adaptive control. In addition to these methods, researchers have also focused on developing new algorithms that can reduce torque and flux ripples while maintaining the simplicity and robustness of conventional DTC. Most prior research on DTC for Syn-RM has predominantly employed traditional methods for estimating flux and torque [21], [65], [70-72]. In this section, Enhanced Direct Torque Control (E-DTC) will be presented, which combines hysteresis-based DTC with a Model Reference Adaptive System (MRAS) flux observer. E-DTC has been shown to achieve excellent torque and flux ripple reduction while maintaining fast dynamic response and robustness against parameter variations. Over all, improving DTC performance and reducing torque and flux ripples are important research topics that can lead to more efficient, reliable, and quiet electric motor systems. With continued research efforts in this area, we can expect to see further advancements in motor control technology that will benefit a wide range of applications from industrial automation to electric vehicles.

II.6.1 Flux and electromagnetic torque estimation

The estimation of flux and electromagnetic torque plays a crucial role in the performance of Direct Torque Control (DTC) systems. Accurate and reliable estimation of these quantities is essential for achieving precise control of motor dynamics. The quality of flux and torque

estimation directly impacts the responsiveness, stability, and efficiency of the DTC control system. A robust and efficient estimation algorithm enables the controller to accurately predict the motor behavior, enabling precise torque control and smooth operation across a wide range of operating conditions. Additionally, improved estimation techniques can help mitigate torque ripple and compensate for variations in magnetic parameters, enhancing the overall control performance and providing a higher level of control accuracy and stability in DTC-based motor drives. This is particularly crucial because the key to achieving smooth operation at high speeds lies in compensating for the back electromagnetic force (EMF) during flux and torque computation. The effectiveness of this enhanced DTC technique will be discussed through simulation results using a fully nonlinear model of Syn-RM.

II.6.2 Syn-RM flux model

The conventional flux estimation is based on voltage and current quantities in the stator reference frame α, β and can be expressed as:

$$\begin{aligned} \psi_\alpha &= \int (v_\alpha - i_\alpha R_s) dt \\ \psi_\beta &= \int \left(v_\beta - i_\beta R_s\right) dt \end{aligned} \tag{II.38}$$

The flux angle can be extracted from (II.38) as,

$$\theta_s = \arctan \frac{\psi_\beta}{\psi_\alpha} \tag{II.39}$$

On the other hand, flux expressions can be found in the literature approximated as the product of inductance and current as follows,

$$\begin{aligned} \psi_d &= L_d i_d \\ \psi_q &= L_q i_q \end{aligned} \tag{II.40}$$

The voltage-based flux estimator mentioned in equations (II.38) is widely recognized to have a detrimental impact on the quality of DTC. This can be attributed to inadequate filter settings and the presence of voltage offset effects. Similarly, the inductance-based flux estimator described in equations (II.40) also suffers from limitations when the identified inductance is mismatched with the real one. To address these issues, a new approach for an optimal flux observer is proposed in this study. The proposed method utilizes the dynamic model in the rotor reference frame (*d, q*) of the Syn-RM, and the formulation of this method is as follows:

$$\begin{aligned}\hat{\psi}_d &= \int \left(V_d - \hat{\imath_d} R_s + \hat{\psi}_q \hat{\omega}_e + K_d(i_d - \hat{\imath_d})\right) dt \\ \hat{\psi}_q &= \int \left(V_q - \hat{\imath_q} R_s - \hat{\psi}_d \hat{\omega}_e + K_q(i_q - \hat{\imath_q})\right) dt\end{aligned} \quad \text{(II. 41)}$$

where K_d, K_q are error gains of the estimated currents $\hat{\imath}_d, \hat{\imath}_q, \widehat{\omega_e}$ denotes the estimated electrical speed and it is obtained by,

$$\hat{\omega}_e = \frac{k_p s + k_i}{s}\left(\psi_s - \hat{\psi}_s\right) \quad \text{(II. 42)}$$

s is Laplace operator, ψ_s is the inductances $L_{d,q}$ related magnetic flux, that can be expressed using (II.40) as:

$$\psi_s = \sqrt{\psi_d^2 + \psi_q^2} \quad \text{(II. 43)}$$

In (II.41) the estimated flux linkage expression contains three terms; the conventional voltage-based expressions as stated in (II.38), and the currents errors multiplied by a proportional gain $K_{d,q}$ for compensation. The back EMF effect is taken into account as well, as an additive speed related term. As a result, the estimated flux to be introduced into DTC loop can be stated from (II.41) as:

$$\hat{\psi}_s = \sqrt{\hat{\psi}_d^2 + \hat{\psi}_q^2} \quad \text{(II. 44)}$$

The electromagnetic torque is written as:

$$\hat{T}_e = \frac{3}{2} P\left(\hat{\psi}_d i_q - \hat{\psi}_q i_d\right) \quad \text{(II. 45)}$$

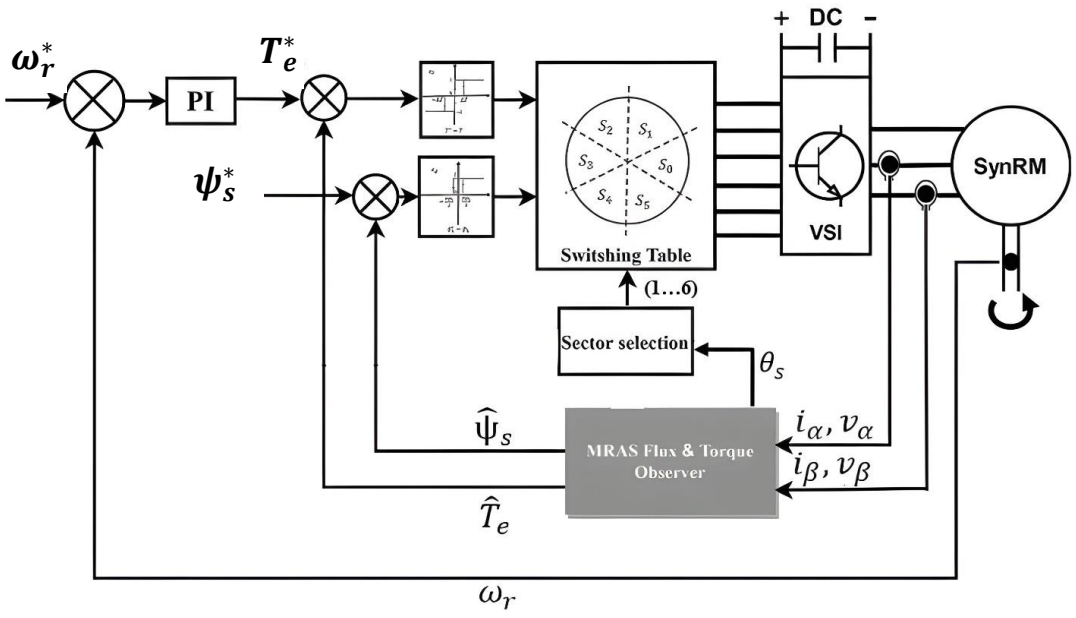

Figure II-33: Overall Syn-RM control scheme of the proposed DTC.

II.6.3 Simulation results and discussion

II.6.3.1 No-load test

The control quality and performance of the proposed method are simulated in the MATLAB/Simulink environment, with a Syn-RM motor whose parameters and inductances *Ld, Lq* are shown in Table A-2 in Appendix. Astep size of 0.05 ms for the Syn-RM model, and of 0.05 ms for the DTC controller and flux observer were considered. The classical DTC is tested using the conventional flux expressed in Equation (II.38), for a fixed flux reference of 0.9 Wb. A speed controller based on PI is employed, and the torque reference limitation is set to 23 N.m, the hysteresis bandwidth settings were optimized, as described in subsection **II.5.1.1**; torque and flux commands, as well as the selected sector are introduced into a preset switching table.

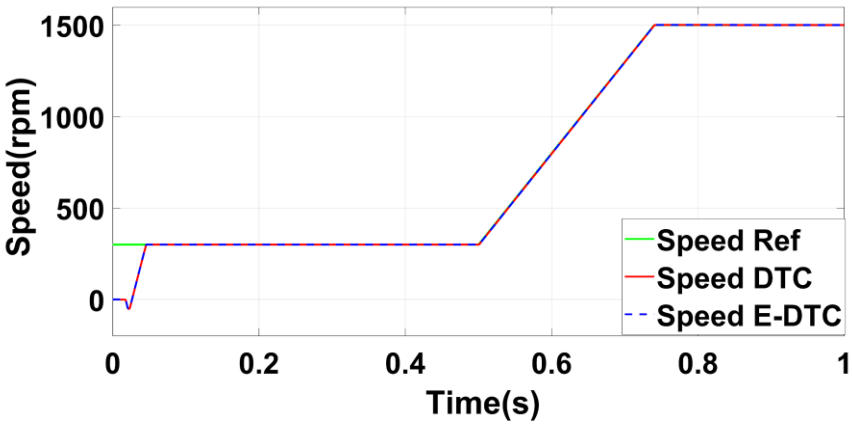

(a)

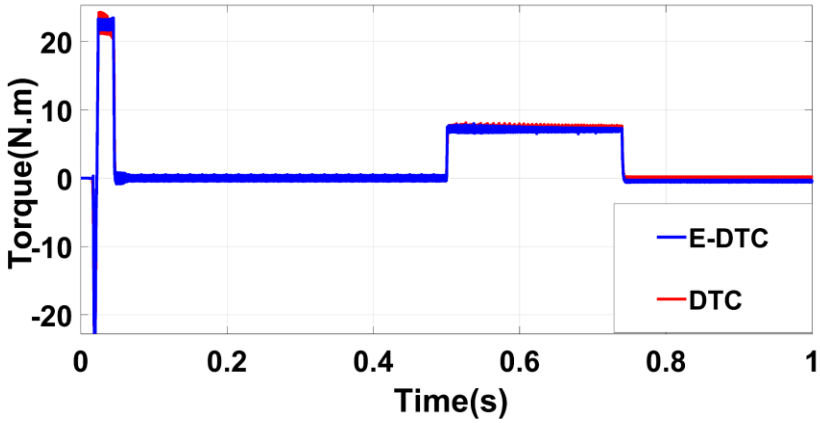

(b)

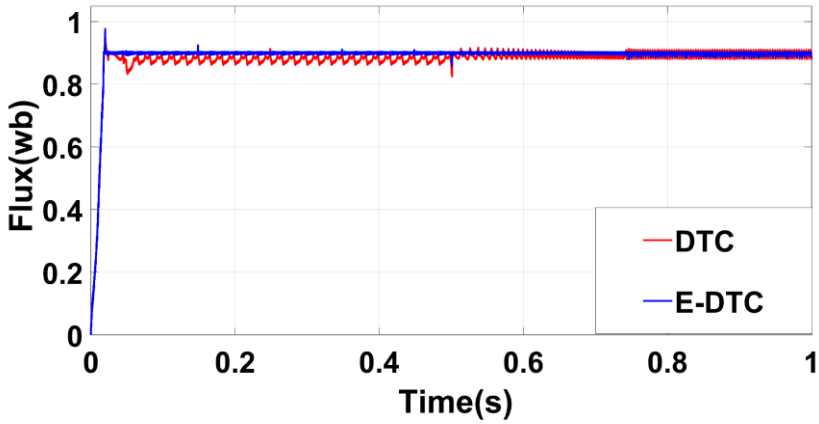

(c)

Figure II-34: Obtained results using both methods, DTC and E-DTC, for comparison: (a) speed (range 300 rpm - 1500 rpm); (b) electromagnetic torque; (c) magnetic flux.

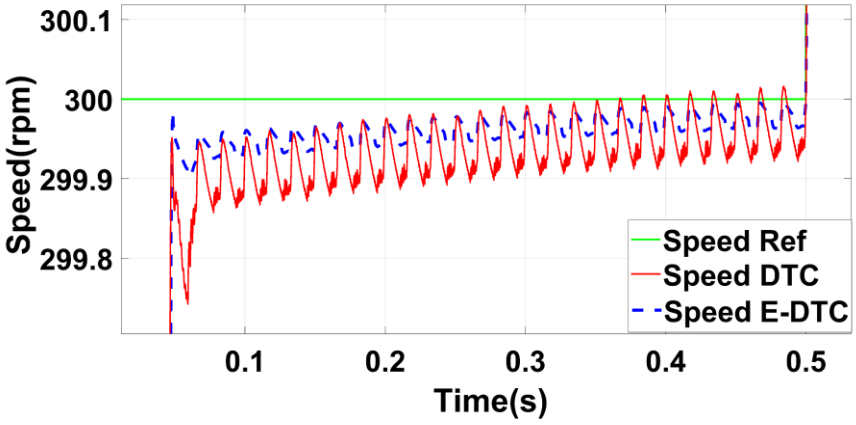

(a)

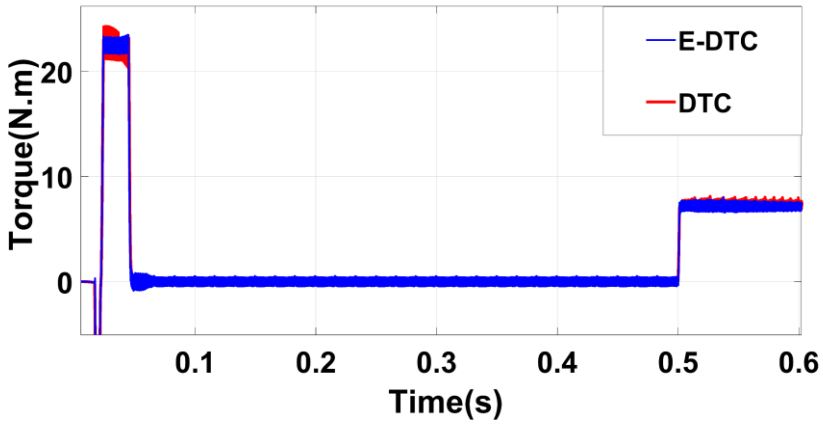

(b)

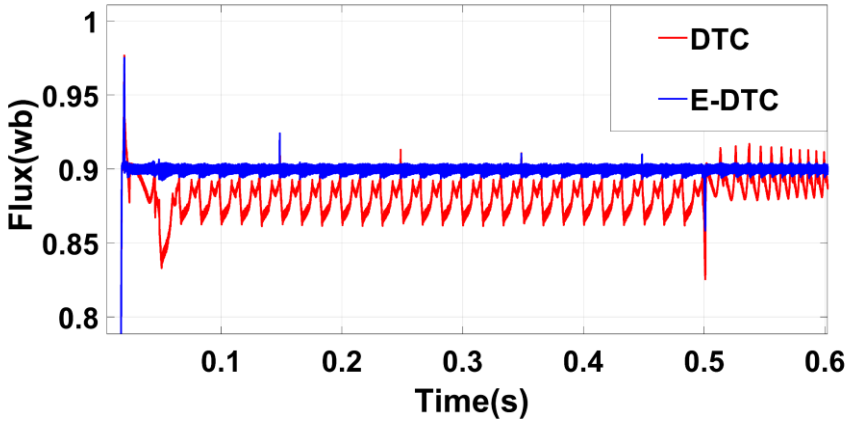

(c)

Figure II-35:Zoom-in of the obtained results during speed-up at 0.5 s using both methods, DTC and E-DTC, for comparison: (a) speed (b) electromagnetic torque (c) magnetic flux.

The effectiveness of the MRAS flux and torque observer described in Equations II.41 is proved for a wide speed range, starting from stand-still speed up to rated speed (1500 rpm). **Figure II-40** presents the no-load test for both DTC and E-DTC. The speed responses for both techniques are acceptable, as the speed variation is restricted within less than 0.2 rpm bandwidth. The torque responses are depicted in **Figure II-40.b** and **Figure II-41.b**. It can be seen that MRAS observer has reduced the torque ripple magnitude as compared to the conventional DTC results, particularly during the transition state and high-speed region. The flux was smoothly controlled along the simulation period, where its fluctuation bandwidth was significantly reduced from 0.04 Wb to less than 0.001 Wb.

II.6.3.2 Full-load test

In this scenario the Syn-RM was fully step loaded (14 N.m) at start-up. **Figure II-42** and **Figure II-43** show the obtained results from 0 to 1500 rpm. As discussed in the no-load test section, the proposed method has a strong effect on the torque ripple reduction, particularly when high torque response is required within the transition state. The flux distortion obtained by using the conventional DTC is almost eliminated, as it is illustrated in **Figure II-42.c** for the low-speed region. The flux response was clearly improved by using the MRAS observer. The electromagnetic torque frequency spectra are shown in **Figure II-44.a** and **Figure II-44.b** for both conventional DTC and E-DTC, respectively. It is evident that in the proposed DTC case, the magnitude of torque harmonics near the fundamental frequency was significantly reduced when compared to those observed in conventional DTC. This reduction in harmonics underscores the superior performance of the proposed DTC method.

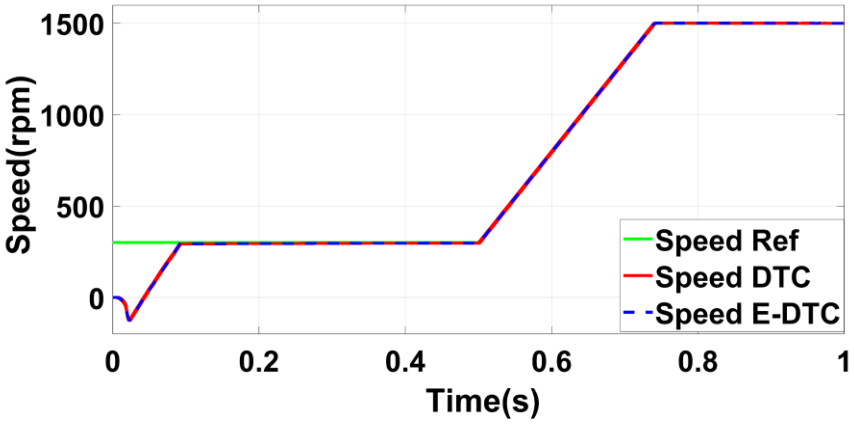

(a)

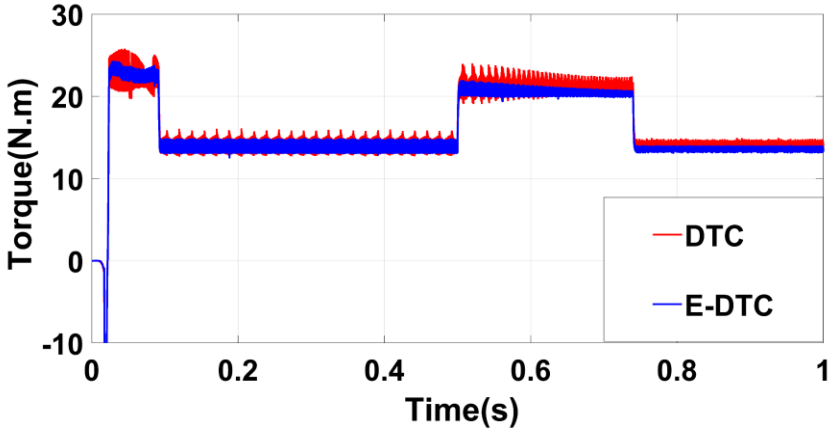

(b)

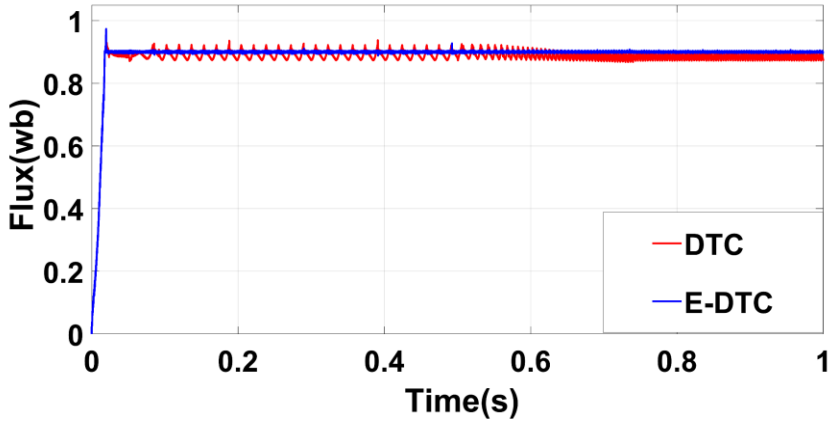

(c)

Figure II-36:Obtained results using both methods DTC and E-DTC, for comparison: (a) speed (range 300 rpm – 1500 rpm); (b) electromagnetic torque at full load (14 N.m); (c) magnetic flux.

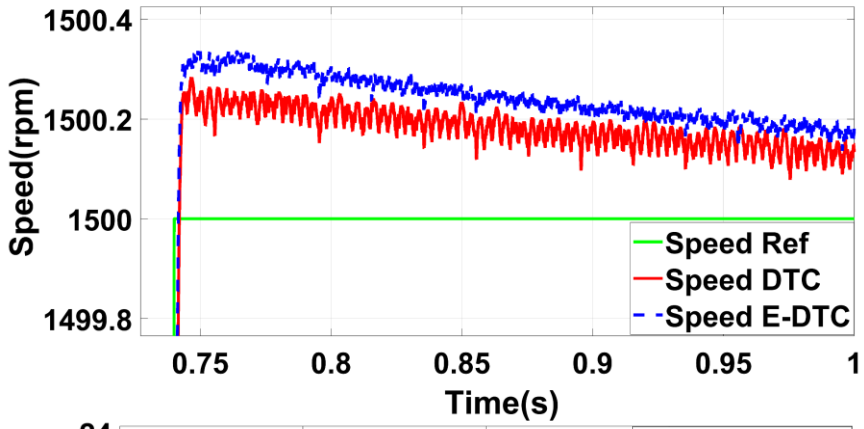

(a)

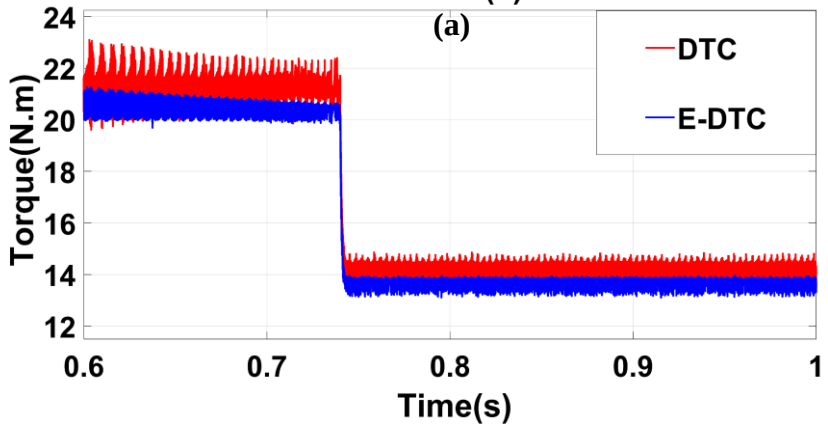

(b)

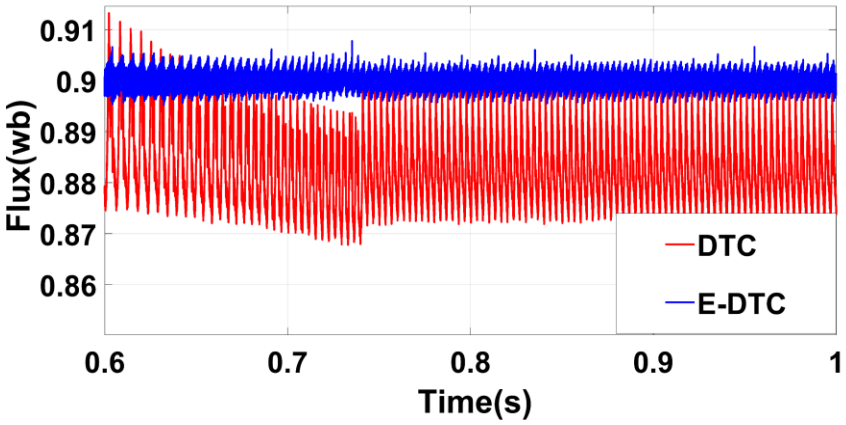

(c)

Figure II-37:Zoom-in of the obtained results during speed-up at 0.5 s, using both methods DTC and E-DTC, for comparison: (a) speed; (b) electromagnetic torque; (c) magnetic flux.

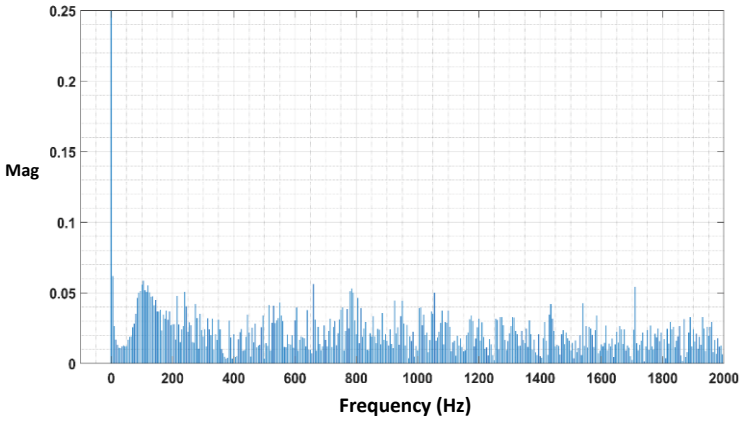

(a)

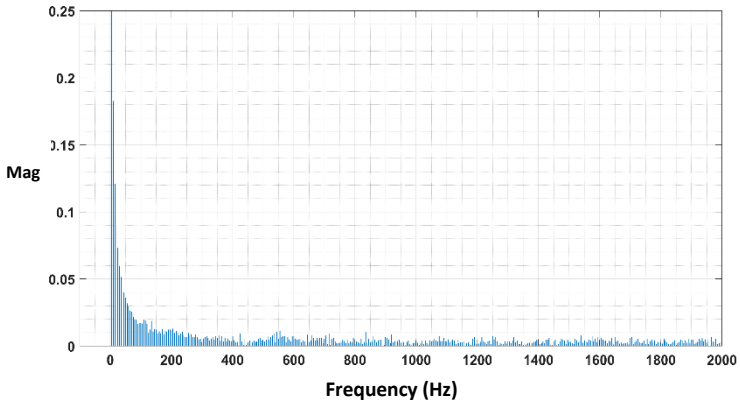

(b)

Figure II-38:Frequency spectra of the electromagnetic torque: (a) conventional DTC; (b) proposed E-DTC.

II.7 Conclusion

In this chapter, the basics of the Syn-RM and its modeling in the form of mathematical equations are presented. Subsequently, based on a set of simplifying assumptions, the model of the Syn-RM in Park's reference frame is established to simplify the system and facilitate the study. The modeling of the power supply and converter section is then addressed. The operating and control principle of the three-phase voltage inverter is presented, along with the principles of the well-known PWM. Various control strategies are explored, including Field-Oriented Control (FOC), conventional Direct Torque Control (DTC), and DTC with SVM technique. Through simulation results, it becomes evident that DTC-SVM emerges as an effective and straightforward approach

to control the Syn-RM. In the following section, a robust DTC was presented using the proposed technique for flux and torque estimation. MRAS model-based observer was employed to estimate the accurate quantities of torque and flux that are required within the DTC loop, instead of using the conventional voltage-based flux-angle. The performance of the proposed E-DTC is confirmed by simulation. The obtained results significantly prove the robustness and accuracy of the Syn-RM speed control using the proposed technique.

Chapter III : Sensorless control of Syn-RM using extended Kalman filter

III.1 Introduction

This chapter explains the theory and fundamentals of the Extended Kalman Filter (EKF). The exploration of this state observer will encompass understanding its core principles, mathematical foundations, and its practical application in controlling Syn-RM systems. Thorough examination of the key components of the EKF algorithm will be undertaken, including prediction and correction steps, covariance matrices, and measurement models. As the discussion proceeds, EKF techniques will be employed to linearize the Syn-RM model, a crucial step necessary for designing effective state estimators. This linearization process is pivotal in ensuring the robust operation of the estimation method. Within the observability study of the full-order Syn-RM model, focus will be on assessing the system's capacity to accurately reconstruct unmeasured states. In the results discussion section, an evaluation of the outcomes stemming from the EKF-based state estimation and control approach will be conducted.

III.2 State observer types

An observer is a mathematical development that allows the reconstruction of the internal states of a system based solely on accessible data, which means the measured inputs and outputs. According to the field of application and use of the state observer, there are two main families of observers:

III.2.1 Deterministic observers

These are observers that do not take into account measurement noise and random fluctuations of state variables when the environment is deterministic. Among these observers, we can mention the Luenberger observer in the case of linear models or the sliding mode observer whose correction term is the sign function.

III.2.2 Stochastic observers

These observers give an optimal estimate of the states based on stochastic criteria. Their observations are based on the presence of noise in the system, which is often the case. The Kalman filter algorithm is a good example of this application.

III.3 Syn-RM speed sensorless control with Extended Kalman Filter (EKF)

III.3.1 EKF observer theory

The Kalman filter allows the reconstruction of the state of a system using the input and measurement signals, as well as its dynamic model in discrete time. The state vector of the system is the information that we try to extract from the noise. In a stochastic environment, when the variances of the noises are known, it is a powerful observer. Moreover, if the noises can be considered as white and Gaussian, it is optimal, i.e., among all linear observers, it offers the lowest deviation of the observation error [76].

The basic Kalman filter algorithm is designed to estimate the state vector of a system with a linear model. If the model is nonlinear, it can be linearized to apply the Kalman filter [77]. This is called Extended Kalman Filter (EKF).

Consider the following non-linear model:

$$\begin{cases} x_{k+1} = f_k(x_k) + w_k \\ y_k = g_k(x_k) + \eta_k \end{cases} \quad \text{(III. 1)}$$

and the covariance matrices of state noise w and measurement noise η:

$$Q_k = \text{cov}(w_k) = E\{w_k w_k^T\} \quad \text{(III. 2)}$$

$$R_k = \text{cov}(\eta_k) = E\{\eta_k \eta_k^T\} \quad \text{(III. 3)}$$

In order to linearize the model (III.1), we apply the Taylor approximation around an estimate $\hat{x}_k$of x_k :

$$\begin{aligned} f_k(x_k) &\approx f_k(\hat{x}_k) + A_k(x_k - \hat{x}_k) \\ g_k(x_k) &\approx g_k(\hat{x}_k) + C_k(x_k - \hat{x}_k) \end{aligned} \quad \text{(III. 4)}$$

where A_k and C_k are the Jacobian matrix defined as:

$$A_k = \left[\frac{\partial f_k}{\partial x_k}(\hat{x}_k)\right] \text{ and } C_k = \left[\frac{\partial g_k}{\partial x_k}\left(\hat{x}_{k,k-1}\right)\right]$$

We define,

$$u_k = f_k(\hat{x}_k) - A_k \hat{x}_k \quad \text{(III. 5)}$$

$$\varphi_k = y_k - g_k(\hat{x}_{k|k-1}) + C_k\hat{x}_{k|k-1} \quad \text{(III. 6)}$$

The nonlinear model (III.1) then becomes the following linearized model:

$$\begin{cases} x_{k+1} = A_k x_k + B_k u_k + w_k \\ \varphi_k = C_k x_k + \eta_k \end{cases} \quad \text{(III. 7)}$$

The EKF regression algorithm consists of an initialization and two steps: the "Prediction" and the "Correction". The optimal estimate provided by the EKF at step $k-1$ is denoted $\hat{x}_{k-1|k-1}$, it is based only on the data available at step $k-1$, as it is the prediction $\hat{x}_{k|k-1}$ calculated at step k. The data at time t_k will be used to perform the optimal correction and determine $\hat{x}_{k|k}$. The initialization focuses on the optimal estimate of the initial state and its variance [78].

Initialization

$$\hat{x}_{0|0} = E(x_0), P_{0|0} = E(x_0 x_0^T) \quad \text{(III. 8)}$$

Prediction

State vector prediction

$$\hat{x}_{k|k-1} = f_{k-1}(\hat{x}_{k-1|k-1}) \quad \text{(III. 9)}$$

Covariance matrix of the prediction error

$$P_{k|k-1} = A_{k-1}P_{k-1|k-1}A_{k-1}^T + Q_{k-1} \quad \text{(III. 10)}$$

Correction

Optimal Kalman gain

$$K_k = P_{k|k-1}C_k^T[C_k P_{k|k-1}C_k^T + R_k]^{-1} \quad \text{(III. 11)}$$

Optimal state estimation

$$\hat{x}_{k,k} = \hat{x}_{k|k-1} + K_k\left(y_k - g_k(\hat{x}_{k|k-1})\right) \quad \text{(III. 12)}$$

Error covariance

$$P_{k|k} = P_{k|k-1} - K_k C_k P_{k|k-1} \quad \text{(III. 13)}$$

With: $C_k = \left[\frac{\partial g_k}{\partial x}(\hat{x}_{k|k-1})\right]$

III.3.2 Full order model based EKF

Our goal is to implement a control without speed sensor, according to the structure presented in Figure III-1. It is therefore a question of estimating the position and speed of the rotor of the Syn-RM, over a large speed range, but with a reasonable computational cost. The full state representation of the Syn-RM model in the $d-q$ reference frame which will allow us to synthesize our observer will be of the following form:

$$\begin{cases} \dfrac{dX(t)}{dt} = A_k X(t) + BU(t) \\ Y(t) = C_k X(t) \end{cases} \tag{III.14}$$

With:

$$X = [i_d \quad i_q \quad \omega_m \quad \theta_m]^T, U = [v_d \quad v_q\ ]^T, Y = [i_d \quad i_q]^T$$

Since we do not know the load torque, assuming that the angular speed remains constant between two sampling instants, the non-linear model of Syn-RM can be written as:

$$\begin{cases} \dfrac{di_d}{dt} = \dfrac{v_d}{L_d} - \dfrac{R_s i_d}{L_d} + p\omega_m \dfrac{L_q}{L_d} i_q \\ \dfrac{di_q}{dt} = \dfrac{v_q}{L_q} - \dfrac{R_s i_q}{L_q} - p\omega_m \dfrac{L_d}{L_q} i_d \\ \dfrac{d\omega_m}{dt} = 0 \\ \dfrac{d\theta_m}{dt} = \omega_m \end{cases} \tag{III.15}$$

The matrix A_k, C_k, B used in (III.14) can be stated as:

$$A_k = \begin{bmatrix} \dfrac{-R_s}{L_d} & \dfrac{p\omega_m L_q}{L_d} & \dfrac{pL_q i_q}{L_d} & 0 \\ \dfrac{p\omega_m L_d}{L_q} & \dfrac{-R_s}{L_q} & \dfrac{pL_d i_d}{L_q} & 0 \\ 0 & 0 & 0 & 0 \\ 0 & 0 & 1 & 0 \end{bmatrix} \tag{III.16}$$

$$B = \begin{bmatrix} \frac{1}{L_d} & 0 \\ 0 & \frac{1}{L_q} \\ 0 & 0 \\ 0 & 0 \end{bmatrix} \quad (\text{III.}17)$$

$$C_k = \begin{bmatrix} 1 & 0 & 0 & 0 \\ 0 & 1 & 0 & 0 \end{bmatrix} \quad (III.18)$$

The discrete formulation of the state model is obtained by discretizing the continuous model between two sampling times, by assuming [79] : $t(k+1) - t(k) = kT_s(k \in N)$

The discrete state system of the Syn-RM can be written in the form:

$$X_{k+1} = A(X_k)X_k + B(X_k)U_k \quad (\text{III.}19)$$

With:

$$X_k = [i_d \quad i_q \quad \omega_m \quad \theta_m]^T, U_k = [V_d \quad V_q]_k^T$$

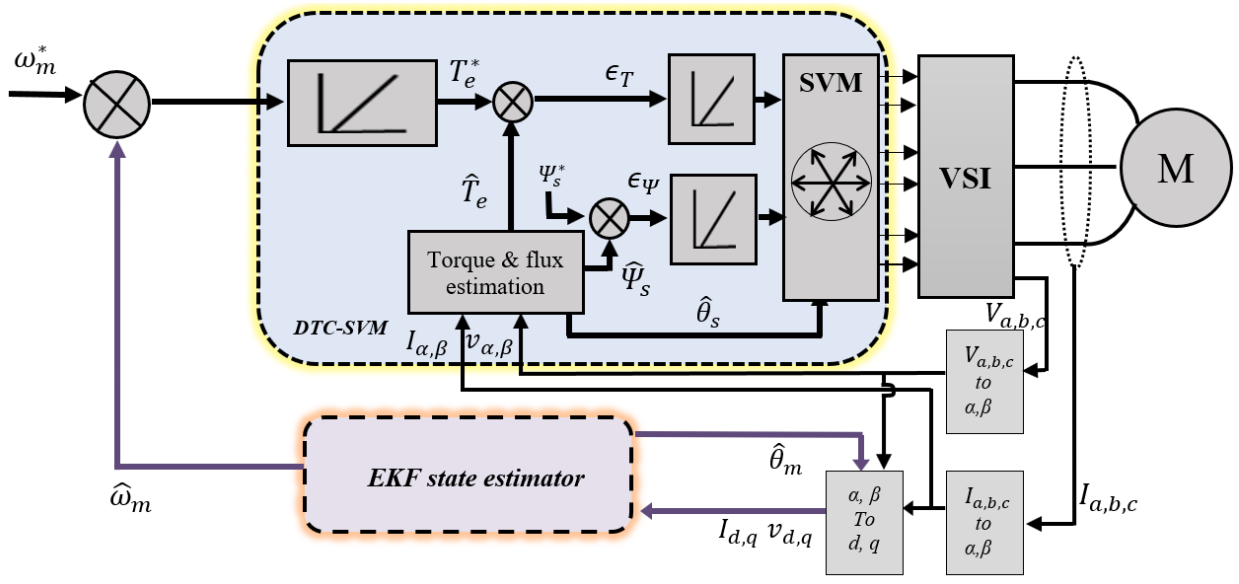

Figure III-1: EKF based sensorless DTC-SVM control schematic of Syn-RM.

If the sampling period T_s is significantly smaller than the time constants of the model, we can employ a straightforward Euler approximation to establish the corresponding discrete mode.

$$f\big(X(k),U(k)\big)=\begin{cases} i_{d,k+1}=i_{d,k}+T_s\dfrac{di_d}{dt}\Big|_{t_k}=\left(1-T_s\dfrac{R_s}{L_d}\right)i_{d,k}+\omega_{m,k}T_s\dfrac{L_q}{L_d}i_{q,k}+T_s\dfrac{v_{d,k}}{L_d} \\ i_{q,k+1}=i_{q,k}+T_s\dfrac{di_q}{dt}\Big|_{t_k}=-\omega_{m,k}T_s\dfrac{L_d}{L_q}i_{d,k}+\left(1-\dfrac{R_s}{L_q}\right)i_{q,k}+T_s\dfrac{v_{q,k}}{L_q} \\ \omega_{m,k+1}=\omega_{m,k}+T_s\dfrac{d\omega_m}{dt}\Big|_{t_k}=\omega_{m,k} \\ \theta_{m,k+1}=\theta_k+T_s\dfrac{d\theta_m}{dt}\Big|_{t_k}=\theta_k+T_s\omega_{m,k} \end{cases} \quad \text{(III. 20)}$$

By applying the Jacobian derivative, linearizing this model around an operating point defined by state x_k yields the following matrices:

$$A(X_k)=\begin{bmatrix} 1-T_s\dfrac{1}{L_d}R_s & p\dfrac{L_q}{L_d}T_s\omega_{m,k} & p\dfrac{L_q}{L_d}T_s i_{q,k} & 0 \\ -p\dfrac{L_d}{L_q}T_s\omega_{m,k} & 1-T_s\dfrac{1}{L_q}R_s & p\dfrac{L_d}{L_q}T_s i_{d,k} & 0 \\ 0 & 0 & 1 & 0 \\ 0 & 0 & T_s & 1 \end{bmatrix} \quad \text{(III. 21)}$$

$$B\ (X_k)=\begin{bmatrix} T_s\dfrac{1}{L_d} & 0 \\ 0 & T_s\dfrac{1}{L_q} \\ 0 & 0 \\ 0 & 0 \end{bmatrix} \quad \text{(III. 22)}$$

The output quantities are given by:

$$Y_k=\begin{bmatrix} i_d \\ i_q \end{bmatrix}_k=C\ (X_k)X_k=\begin{bmatrix} 1 & 0 & 0 & 0 \\ 0 & 1 & 0 & 0 \end{bmatrix}X_k \quad \text{(III. 23)}$$

where the mechanical speed ω_m is supposed constant over each sample period T_s.

Selecting the appropriate reference frame is crucial when applying the Kalman filter. The optimal approach involves utilizing the Park's frame of reference, which is connected to the rotor. Accordingly, in our situation, we opted for a model that employs the rotor frame of reference (d, q), and the Extended Kalman Filter (EKF) is utilized to determine the state vector

X_k, which includes the i_d and i_q currents, mechanical speed ω_m, and rotor position θ_m. This nonlinear model operates under the assumption that the mechanical speed is a state, rather than a parameter [78].

To cope with the uncertainties and disturbances of the system, the Syn-RM is represented by the following non-linear stochastic model:

$$\begin{cases} X(k+1) = f(X(k), U(k)) + W(k) \\ Y(k) = C_d X(k) + V(k) \end{cases} \quad \text{(III. 24)}$$

The Kalman filter considers the covariance matrix of the state vector P and the covariance of the system and measurement noise vectors such that:

$$\begin{aligned} Q(k) &= E\{W(k)W^T V(k)\} \\ R(k) &= E\{V(k)V^T(k)\} \end{aligned} \quad \text{(III. 25)}$$

Assuming that $Q(k)$ and $R(k)$ are matrices with diagonal elements, the α and β axes have identical parameters. This implies that a total of four noise covariance components must be known.

III.3.3 Observability of Syn-RM linearized model

If we analyze the last column of matrices $A(X_k)$ and $C\ (X_k)$, we observe that the last state variable (position θ_m) has no direct impact (due to the two zeros in the last column of $C\ (X_k)$) or indirect influence (due to the three zeros in the last column of $A\ (X_k)$) on the model's outputs. This result can also be confirmed through the controllability matrix of the pair ($A(X_k)$ and $C\ (X_k)$):

$$O_{A,C} = \begin{bmatrix} C\ (X_k) \\ C\ (X_k)A(X_k) \\ C\ (X_k)A^2(X_k) \\ C\ (X_k)A^3(X_k) \end{bmatrix} \quad \text{(III. 26)}$$

The specific form of matrices $A(X_k)$ and $C(X_k)$ results in the last column of all terms in $C(X_k)\ A^i(X_k)$ being zero. As a result, this matrix is not of full rank, and the position is not observable. It is also not detectable because it is associated with an unstable mode (integration).

The previous observability matrix has a rank of 3, but only if the current is non-zero, because of the following:

$$O_{A,C} = \begin{bmatrix} C\,(X_k) \\ C\,(X_k)A(X_k) \end{bmatrix} = \begin{bmatrix} 1 & 0 & 0 & 0 \\ 0 & 1 & 0 & 0 \\ 1 - \frac{R_s T_s}{L_d} & \frac{L_q T_s}{L_d}\omega_k & \frac{L_q T_s}{L_d} i_{q,k} & 0 \\ -\frac{L_d T_s}{L_q}\omega_k & 1 - \frac{R_s T_s}{L_q} 1 & -\frac{L_d T_s}{L_q} i_{d,k} & 0 \end{bmatrix} \quad \text{(III. 27)}$$

So, it is sufficient for either $i_{d,k}$or $i_{q,k}$to be non-zero for the matrix above to have a rank of three ($n = 3$), and consequently, the speed becomes observable. However, if $i_{d,k}$= $i_{q,k}$= 0, the two zeros that appear in the third column of $O_{A,C}$ render the speed no longer indirectly influential (through $A(X_k)$) on the measured outputs. It also becomes unobservable. This can be explained physically. When the currents are zero, the electromotive forces (EMFs) are also zero, and the speed is no longer discernible through electrical quantities.

III.3.4 The implementation of discrete EKF

We summarize in the followings the different steps allowing the implementation of the EKF algorithm:

Step 1: Initialization of the system state and of its covariance matrix:

$$\begin{aligned} X(0/0) &= X(0) \\ P(0/0) &= P(0) \end{aligned} \quad \text{(III. 28)}$$

Step 2: Prediction phase, which consists of estimating the state and the output in the following form:

$$\begin{aligned} \hat{X}(k+1|k) &= f(\hat{X}(k+1|k), U(k), k \\ \hat{Y}(k+1) &= C_d \hat{X}(k+1|k) \end{aligned} \quad \text{(III. 29)}$$

This step allows to construct a first estimate of the state vector at time $k + 1$. We then look to determine its variance.

Step 3: Computation phase of the EKF covariance matrix given by:

$$P(k+1|k) = F(k)P(k)F^T(k) + Q \quad \text{(III. 30)}$$

With,

$$F(k) = \left.\frac{\partial\big(X(k), u(k)\big)}{\partial X^T(k)}\right|_{x(k)=\hat{x}\left(\frac{k}{k}\right)} \quad \text{(III. 31)}$$

Step 4: Correction phase, which consists in calculating the optimal gain of the EKF at time $(k+1)$:

$$K(k+1) = P(k+1|k)H^T(k)\big(H(k)P(k+1|k)H^T(k) + R(k)\big)^{-1} \quad \text{(III. 32)}$$

Such that:

$$H = \begin{bmatrix} 1 & 0 & 0 & 0 \\ 0 & 1 & 0 & 0 \end{bmatrix} \quad \text{(III. 33)}$$

Step 5: Calculation of the covariance matrix of the EKF error which is given by:

$$P(k+1\,|k+1) = P(k+1|k) - K(k+1)H(k)P(k+1|k) \quad \text{(III. 34)}$$

Step 6: Estimation of the state vector at time k+1:

$$\hat{X}(k+1|k+1) = \hat{X}(k+1|k) + K(k)\left(Y(k+1) - H(k)\hat{X}(k+1|k)\right) \quad \text{(III. 35)}$$

The simulations presented in this section are carried out in order to evaluate the performance of the Kalman filter-based estimation algorithm and, consequently, the performance of the overall training system. The system is subjected to various simulation tests. The results obtained concern a speed setting by a PI controller . The adjustments of the covariance matrices Q and R were carried out by simulation tests in order to ensure a global stability of the drive throughout the whole speed range, while respecting a compromise between dynamics and static errors.

Figure III.1 depicts the overal structure of the presented sensorless control scheme , where DTC-SVM was incorporated with EKF algorithm.

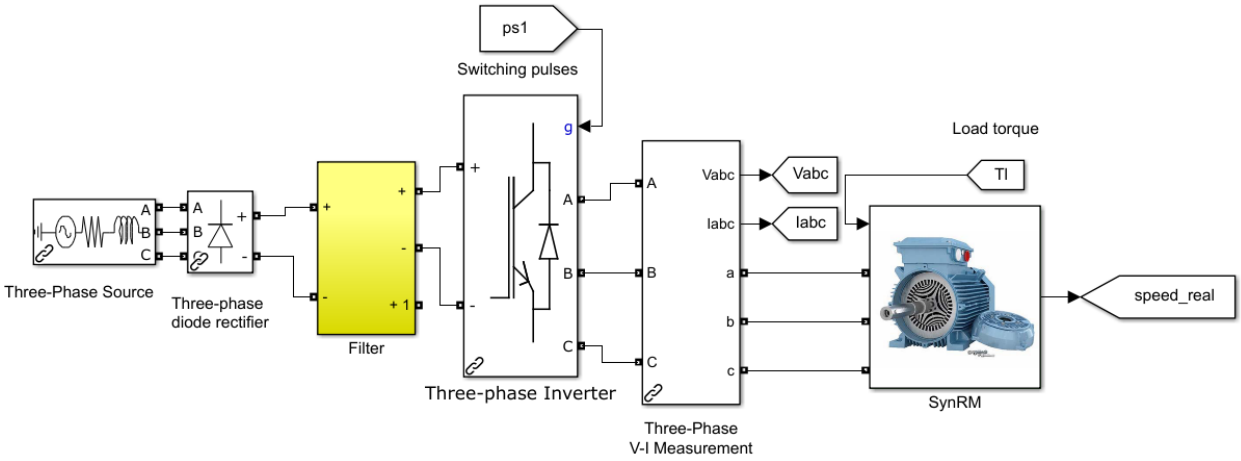

Figure III-2:Overall arangement of the simulation model based on Syn-RM.

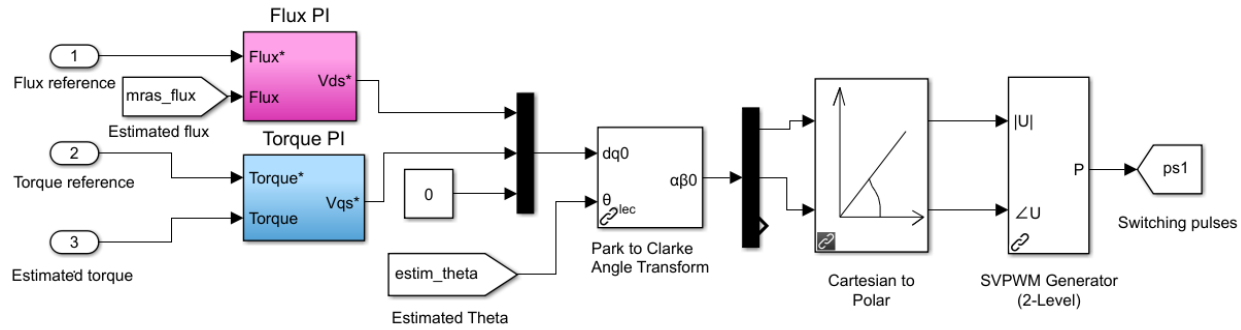

Figure III-3:Flux and torque controlllers with SVPWM technique.

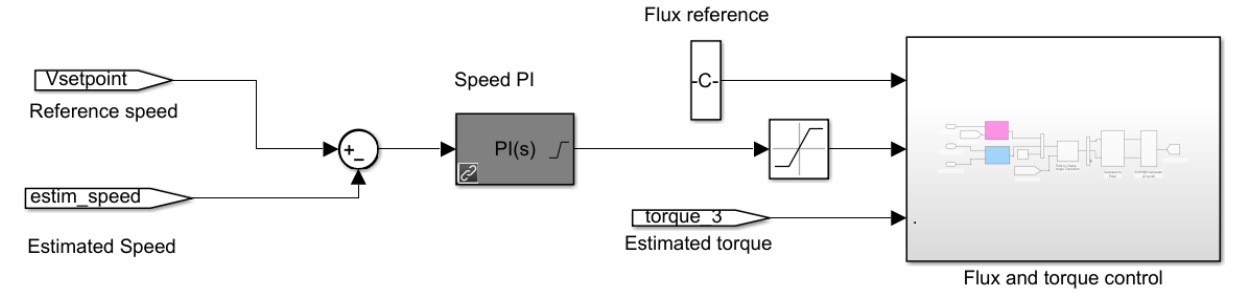

Figure III-4:Speed control based on PI controller.

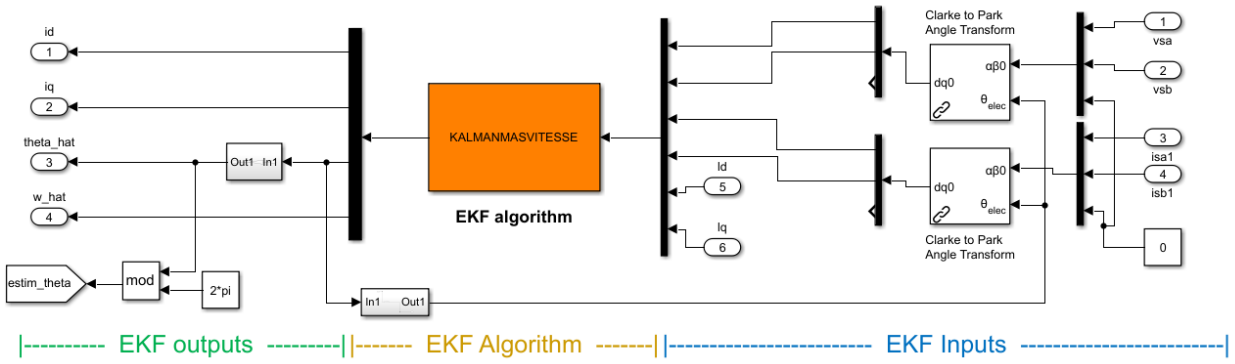

Figure III-5:The overall EKF algorithm schematic.

III.4 Simulation results and discussion

Using the model presented in subsection II.2.2 and the previous algorithm, we have built a simulation of the sensorless control. This simulation was mainly used to debug our EKF, before implementing and testing it in real time. It does not allow to adjust the variances of the state and output noises, because it would be necessary to know the characteristics of the modeling and measurement errors in order to inject realistic errors or realistic errors or noises in the signals.

The simulation was performed in Matlab/Simulink using a fully nonlinear model of Syn-RM with parameters given in **Table A-1**. The magnetic saturation was taken into account in the dynamics. The sample time was set to 0.05 ms The presented control scheme stands for DTC-SVM incorporated with EKF speed estimation technique. Three simulation scenarios were carried out, including speed and load variation.

III.4.1 Disturbance rejection

Figure III-6 depicts the obtained results during low-speed operation. Initially, the speed was set to 10 rpm, and the load was set to 2 N.m. At t=0.5 s, a full load of 14 N.m was suddenly applied. Analyzing the first channel in Figure III.6, it is evident that the estimated speed is closely tracking the actual speed, despite the abrupt change in load torque. This demonstrates the effectiveness of the sensorless control method in adapting to dynamic load variations.

Furthermore, the response of the estimated currents, i_d and i_q is clearly superimposed over their actual values, as shown in **Figure III-6**. This indicates that the observer-based approach successfully estimates the currents accurately, even in the presence of load disturbances.

These results provide strong evidence of the robustness and reliability of the proposed sensorless control strategy for the Syn-RM. It not only ensures accurate tracking of the speed reference but also maintains precise estimation of the machine parameters. Additionally, the control method exhibits excellent transient response and robustness to load changes, which are crucial factors for the overall performance and stability of the drive system.

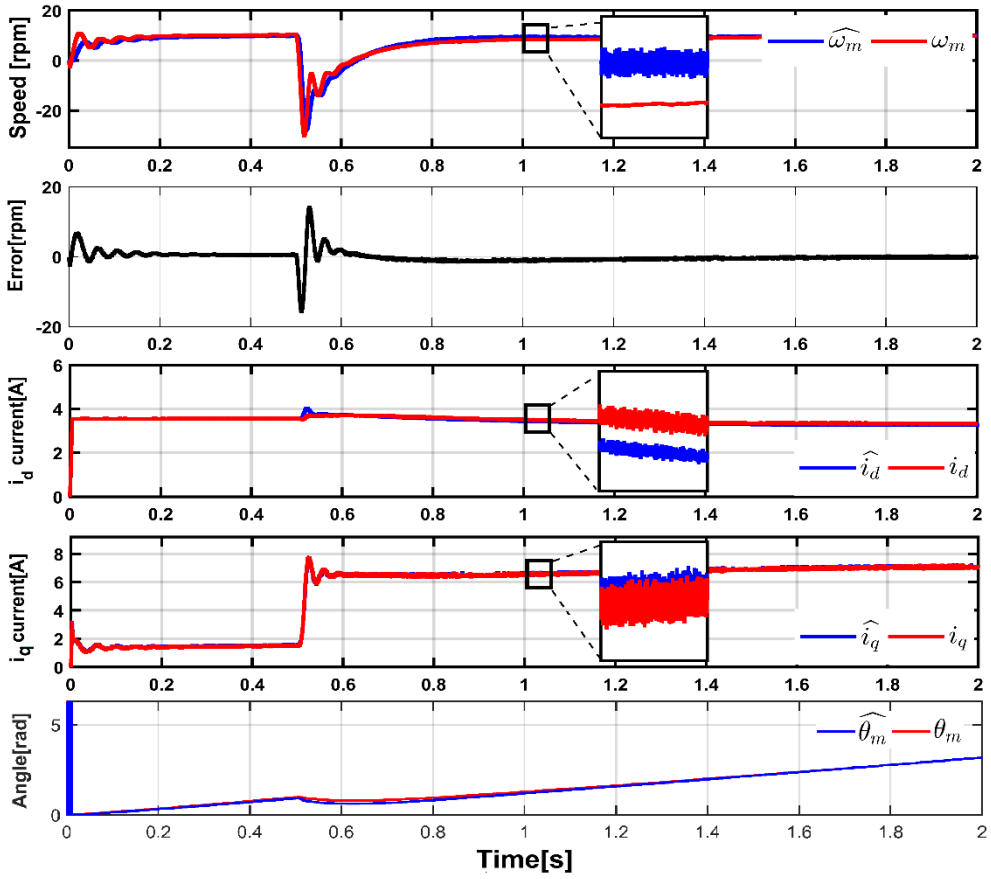

Figure III-6: Simulation results under low-speed test (10 rpm), and full load (14 N.m).

III.4.2 Transition to high speed

In **Figure III-7**, we present the simulated response of a high-speed operation test. At t=0 (s), the speed was increased from a standstill to 1000 rpm. Subsequently, at t=1.5 s, a full load was applied. Then, at t=2 s, the speed ramped up to the rated value of 1500 rpm. The plot in **Figure III-7** demonstrates the remarkable performance of the control system, particularly in high-speed scenarios. Thanks to the fast computation capacity of the Extended Kalman Filter (EKF), the speed

estimation error is sufficiently minimized throughout the test. Moreover, the response of the estimated currents, i_d and i_q, also shows excellent agreement with their actual values. The EKF's ability to rapidly estimate these currents contributes to the overall robustness of the control method.

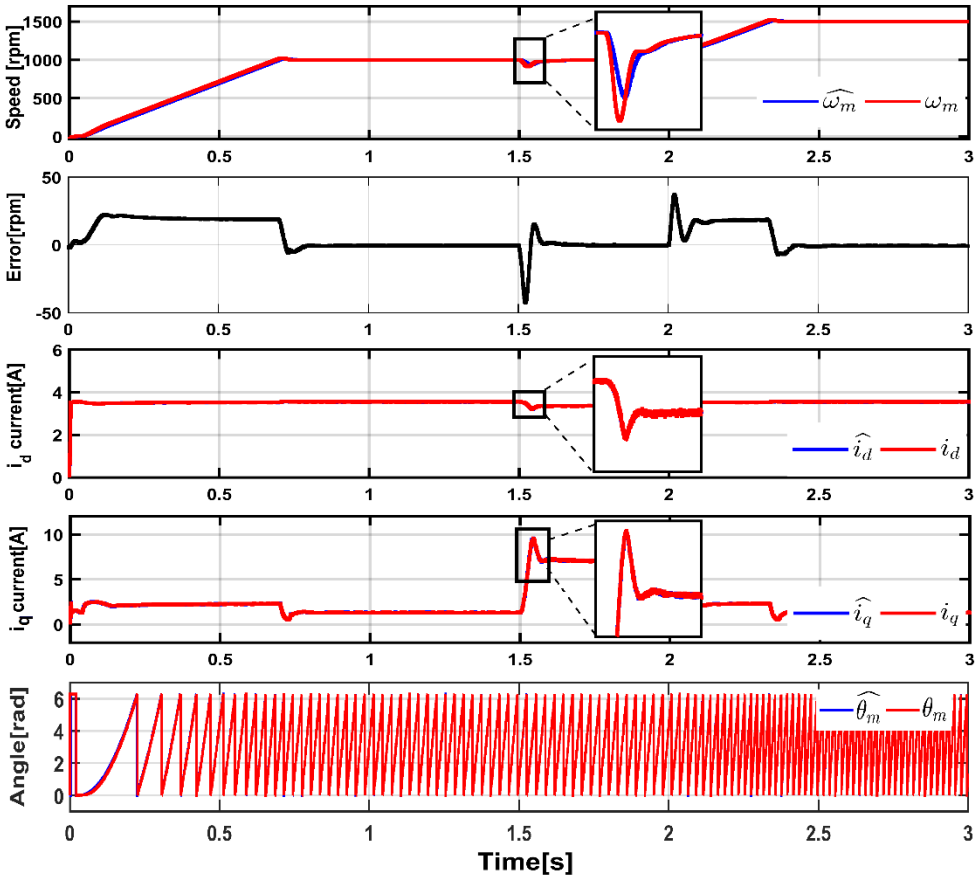

Figure III-7:Simulation results under speed change, and full load (14 N.m).

III.4.3 Sinusoidal setpoint tracking

To further investigate and assess the effectiveness of the proposed Extended Kalman Filter (EKF), an additional test was conducted on a synthetic rotary machine (Syn-RM). The test involved applying a sinusoidal speed setpoint with an amplitude of 200 rpm and an offset of 450 rpm. Additionally, the load was set to 4 N.m. The results of this test are depicted in **Figure III-8**. Upon analyzing the results, it can be seen that the speed tracking error remained within a narrow bandwidth of less than 20 rpm. This observation underscores the robustness and efficiency of the EKF in accurately tracking and controlling the speed of the Syn-RM. Furthermore, the start-up

response of the estimated angle, as determined by the EKF algorithm, exhibited a remarkable level of convergence towards the actual angle value. This convergence indicates that the estimated angle closely aligned with the true angle of the Syn-RM, resulting in accurate and reliable estimations

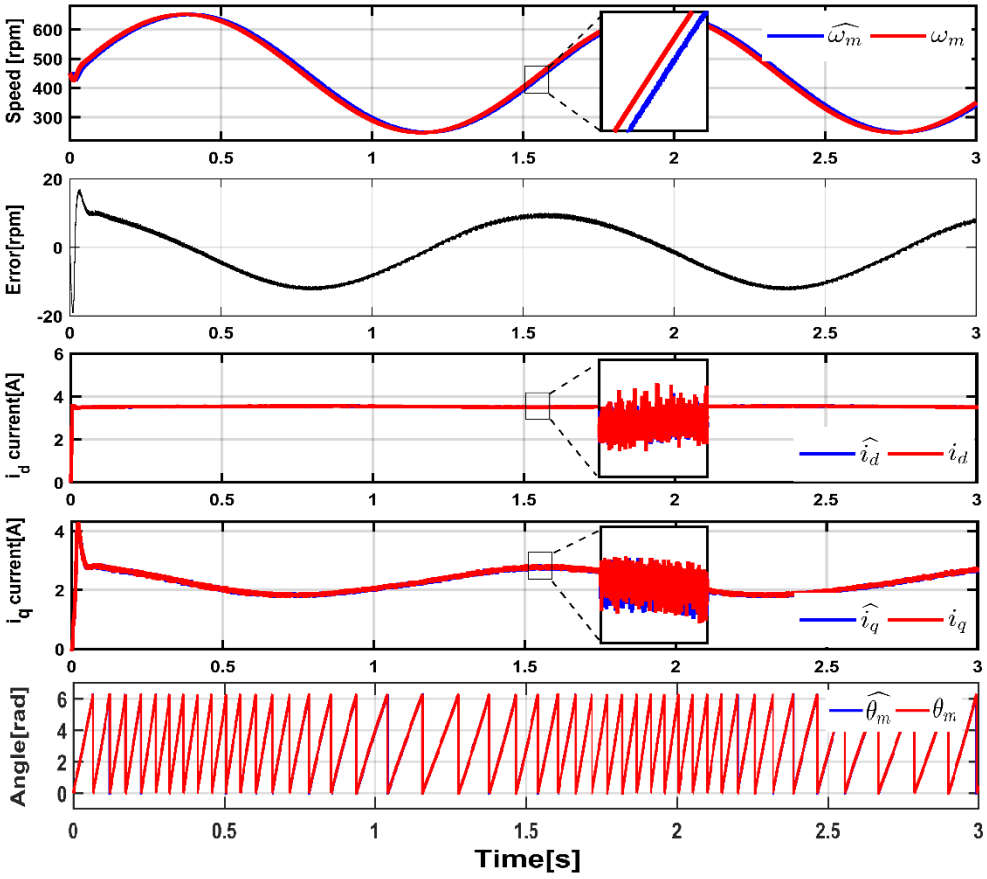

Figure III-8:Simulation results under sinusoidal speed variation, at a load level of 4 N.m.

III.5 Conclusion

In this chapter, a simple sensorless control scheme (DTC-SVM) for Syn-RM was presented, using an Extended Kalman Filter-based observer (EKF) and a PI controller with SVM technique. The simulation results obtained have led us to conclude that the sensorless speed control of the DTC-SVM for the Syn-RM is quite fast and robust, even in the presence of load disturbances, or changes in the speed reference. It was also observed that this control method is characterized by its simplicity of design and mechanical robustness. Indeed, it has allowed us to eliminate the need for any speed or position sensors which are necessary for coordinates' transformation. It is worth

noting that the adjustment of the Q and R matrices of the Kalman filter should be performed through simulation tests to ensure drive stability across the whole speed range, while striking a balance between dynamics and static errors.

Chapter IV : Model-free predictive current control of Syn-RM

IV.1 Introduction

Looking to the typical structure of Model Based Control (MBC), the mathematical model of the studied system plays a crucial role in this control design method [80-82]. Relying on this fact, the control performance, safety, and reliability of MBC methods are highly dependent on the correctness of the system model used in the control design [91] [92]. The slightest mismatch in system parameters may affect the control and lead to an inevitable degradation in performance [83].

This chapter introduces model-free control to deal with the MPC drawbacks mentioned above. The proposed structure consists of incorporating the conventional predictive current control with system lumped uncertainties estimation technique based on time delay estimation approach. The benefit is that it does not need all the system's parameters. Also, it does not use the decoupling term for Syn-RM control compared to conventional control like field-oriented control based on the traditional PI controller. Moreover, its control law is not complicated to design and prove. Finally, to validate the model-free control, the Syn-RM control simulation will be performed to emphasise the gained performance and robustness.

IV.2 Model free control and control law

IV.2.1 Model free control structure

The types of the modern control system can be roughly categorized by MBC and Model Free Control (MFC), as in **Figure IV-1,** where the model identification and / or reduction is an essential task in MBC control type**.**

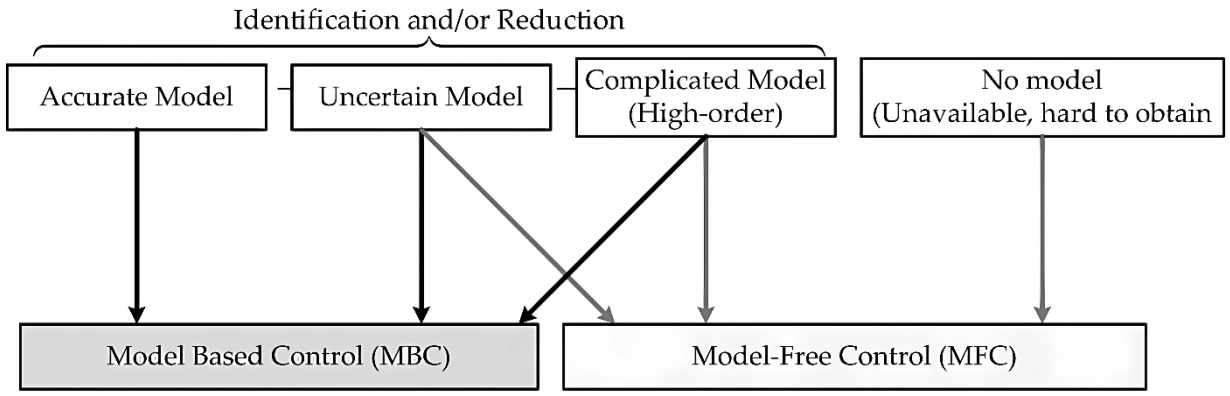

Figure IV-1: Categorization of modern control systems into MBC and MFC [89].

The concept of model-free based control performed for the control system application was first presented by Fliess et al. [92]. A brief theory of model-free control is provided as follows.

A nonlinear system given by a state-variable expression is:

$$\begin{aligned} \dot{x} &= f(x,u) \\ y &= h(x,u) \end{aligned} \tag{IV.1}$$

where,

$$\begin{aligned} x &= [x_1, x_2, \dots, x_n]^T; x \in \mathbb{R}^n \\ u &= [u_1, u_2, \dots, u_m]^T; u \in \mathbb{R}^m \\ y &= [y_1, y_2, \dots, y_m]^T; y \in \mathbb{R}^m \end{aligned} \tag{IV.2}$$

x is the state variable, u is the control variable, y is the measurable variable (or output variable), and $n, m \in N$.

A system is flat if we can find a set of flat outputs equal in number to the number of inputs. More precisely, if the system has state variables $x \in R^n$ and input variables $\in R^m$, thus, if there exists a set of flat outputs $y \in R^m$, the system is flat.

A control can be defined as:

$$u = u_{ref} + u_{feedback}\,(\varepsilon) \tag{IV.3}$$

with

$$u_{feedback} = K_p \cdot \varepsilon + K_r \int \varepsilon \, dt \tag{IV.4}$$

and

$$u_{\text{ref}} = \psi\left(y_{\text{ref}}, \dot{y}_{\text{ref}}\, \ddot{y}_{\text{ref}}, \dots, y_{\text{ref}}^{(\beta+1)}\right) \tag{IV.5}$$

where

$$\varepsilon = y_{ref} - y \tag{IV.6}$$

ε is the error between the desired value and the measured value.

According to (IV.3), this control law is suitable for wholly known all parameters system. However, if only some system parameters can be identified, the controller needs to be modified, as the partial-known model is replaced by the model-free control, given as follows:

$$u = \frac{\hat{\alpha}\left(y, \dot{y}, \ddot{y}, \ldots, y^{(n)}\right)}{b} + \frac{F}{b} \tag{IV.7}$$

Alternatively, it can be rewritten and rearranged as a straightforward linear model as follows:

$$\dot{y} = -F + b \cdot u \tag{IV.8}$$

where $\hat{\alpha}\left(y, \dot{y}, \ddot{y}, \ldots, y^{(\beta+1)}\right)$ is a known part of $\alpha\left(y, \dot{y}, \ddot{y}, \ldots y^{(\beta+1)}\right)$ and F stands for all the other dynamics of the system [93].

IV.2.2 Control law and intelligent PI controller (iPI)

Figure IV.2 represents the block diagram of the model-free control based on intelligent PI. The control law is defined as follows:

$$u = u_{ref} + u_{feedback}\,(\varepsilon) + \frac{\hat{F}}{b} \tag{IV.9}$$

with

$$u_{\text{ref}} = \frac{\hat{\alpha}\left(y_{\text{ref}}, \dot{y}_{\text{ref}}, \ddot{y}_{\text{ref}}, \ldots y_{\text{ref}}^{(\beta+1)}\right)}{b} \tag{IV.10}$$

and

$\hat{F}$ is the estimated value of F, which is given as:

$$\hat{F} = b \cdot u - \dot{y} \tag{IV.11}$$

The feedback part $u_{feedback}$ is given by applying a PI controller, as follows:

$$u_{\text{feedback}} = K_{\text{p}} \cdot \varepsilon + K_1 \int \varepsilon dt \tag{IV.12}$$

Substituting (IV.9) into (IV.8) and rearranging, (IV.8) can be rewritten as:

$$\dot{y} = -F + b \cdot u_{\text{ref}} + b \cdot u_{\text{feedback}}\,(\varepsilon) + \hat{F} \tag{IV.13}$$

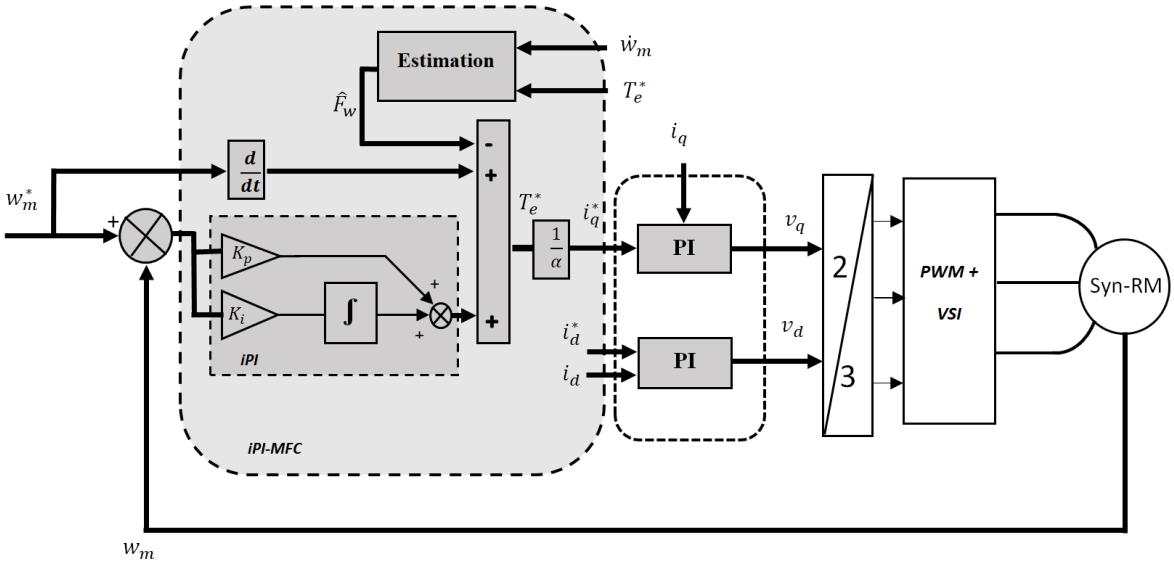

Figure IV-2: Control law of MFC based on intelligent PI [94].

IV.3 Model based predictive current control of Syn-RM (MB-PCC)

The conventional MB-PCC consists of two control loops, an outer loop for speed control and an inner loop for current predictive control. This later is going to be the main scope of this chapter, whereas a classical Proportional Integrator (PI) is employed for the speed control loop. As depicted in **Figure IV.3**, the value of the current reference $I_{q|k}^*$ is obtained from the speed PI controller, and $I_{d|k}^*$ is calculated based on maximum torque per ampere (MTPA) control [95]. The model-based predictive current control employs the system parameters to predict the next time step current quantities, using Euler approximation. The discrete form of the predicted currents stated in equation II.25 in Chapter II can be written as:

$$\begin{cases} I_{d|k+1} = \left(1 - \dfrac{R_s T_s}{L_d}\right) I_{d|k} + \omega_e T_s \dfrac{L_q}{L_d} I_{q|k} + \dfrac{T_s}{L_d} V_{d|k} \\ I_{q|k+1} = \left(1 - \dfrac{R_s T_s}{L_q}\right) I_{q|k} - \omega_e T_s \dfrac{L_d}{L_q} I_{d|k} + \dfrac{T_s}{L_q} V_{q|k} \end{cases} \quad (\text{IV.14})$$

where $I_{d|k}$ and $I_{q|k}$ are the measured currents at the k^{th} time step, T_s is the sampling time, and $V_{d|k}$ and $V_{q|k}$ are the applied voltage components.

The selected voltage vectors are optimized through a short iteration algorithm containing the eight possible voltage vectors candidates. The cost function equation below (IV.15) minimizes the errors between the reference currents and their predicted values [96]: .

$$g = \left[I^*_{d|k} - I_{d|k+1}\right]^2 + \left[I^*_{q|k} - I_{q|k+1}\right]^2 + I_{sat} \quad \text{(IV. 15)}$$

where I_{sat} is a protection constraint value related to the predicted current $i_{s|k+1}$ defined as:

$$I_{sat} = \begin{cases} \infty, & \text{if } \left|I_{s|k+1}\right| > \left|I_{s_{max}}\right|, \left|I_{s|k+1}\right| = \sqrt{I^2_{d|k+1} + I^2_{q|k+1}} \\ 0, & \text{otherwise.} \end{cases} \quad \text{(IV. 16)}$$

***Remark 1*:** In most AC drive control schemes, speed control is usually performed using classical PI due to the slow dynamics of the mechanical speed and it is less affected by parameter changes. In **Figure IV.3** the speed error is minimized with a simple PI control with the parameters K_P and K_I that are given in Table A-3 in Appendix.

IV.4 Model free control based on time delay estimation

In this section, a control scheme is suggested that combines the conventional PCC approach with model-free control, as proposed by Fliss and Joint in [92]. The scheme is made more robust through the use of the Time Delay Estimation technique (TDE), which estimates local unknown dynamics and uncertainties. Hence, the nonlinear dynamics of the currents in equation (IV.14) are represented by ultra-local models. To estimate the local dynamics, the TDE approach is utilized, and the Particle Swarm Optimization (PSO) algorithm is employed to optimize the design parameters. The overall control scheme of the proposed method is depicted in Figure IV.3.

IV.4.1 Ultra local model

For a given non-linear dynamic system, its general ultra-local expression can be written as:

$$y^v = f(t) + \alpha U \quad \text{(IV. 17)}$$

y^v is the v^{th} derivative of the system output y

$f(t)$ is the lumped uncertainties resulting from unmodeled dynamics, and unknown disturbances.

U is the control input signal.

α is a given constant.

The complex dynamic model of Syn-RM in (IV.14) can be represented by an ultra-local model according to (IV.17) as follows:

$$\begin{cases} \dot{I}_d = f_d(t) + \alpha_d V_d \\ \dot{I}_q = f_q(t) + \alpha_q V_q \end{cases} \quad \text{(IV. 18)}$$

where f_d and f_q are the lumped parameter uncertainties and nonlinear dynamic functions which are considered unknowns, and α_d and α_q are design constants. In model-free control design, various techniques were proposed to estimate the unknown dynamic functions [84-88] [90], such as extended state observer approach [24], nonlinear disturbance compensation technique [25], and adaptive neural network approximator based on extended Kalman filter [28]. In this study, the TDE technique is proposed to estimate all the unknown dynamic functions and parameter variations. This approach is easy to implement since it only requires the measured input/output data of the system to compute the unknown functions with a small computational burden.

IV.4.2 Time delay estimation technique

The estimation accuracy of f_d and f_q can have an impact on control performance since it includes the dynamics or disturbances of the system. As a result, the solution of f_i for $i \in \{d, q\}$ becomes a key problem for this approach. TDE is frequently utilized to estimate unknown nonlinear dynamics, where time-delayed signals are used to estimate the lumped uncertainty and bring about a simple and useful model-free feature [35]. Consequently, using the TDE approach, an acceptable approximation of f can be obtained; $f_i(t-\varepsilon)$ is regarded as the estimated value of $f_i(t)$. As long as the time delay is minimal, we consider $\hat{f}_i(t) \approx f_i(t) \approx f_i(t-\varepsilon)$, thus obtaining:

$$\hat{f}_i(t) = \dot{y}_i(t) - \alpha U_i(t) \quad \text{(IV. 19)}$$

$$\hat{f}_i(t) \approx \hat{f}_i(t-\varepsilon) = \dot{y}_i(t-\varepsilon) - \alpha U_i(t-\varepsilon) \quad \text{(IV. 20)}$$

To achieve a stable control output and prevent excessive chattering, a low pass filter (LPS) is introduced in the calculation of $\hat{f}_i(t)$. Additionally, fast converging gains β_d and β_q have been incorporated into the proposed TDE to expedite the convergence of the control algorithm. The values of $\hat{f}_d$ and $\hat{f}_q$ are thus estimated using the following formulas:

$$\begin{cases} \hat{f}_d(t) = \beta_d\left[\text{LPS}\left[\dot{I}_d(t-\varepsilon) - \alpha_d V_d(t-\varepsilon)\right]\right] \\ \hat{f}_q(t) = \beta_q\left[\text{LPS}\left[\dot{I}_q(t-\varepsilon) - \alpha_q V_q(t-\varepsilon)\right]\right] \end{cases} \quad \text{(IV. 21)}$$

The first-order LPS is adopted, with the transfer function given as follows:

$$\begin{cases} h_d(P) = \dfrac{1}{\dfrac{1}{w_d}P + 1} \\ h_q(P) = \dfrac{1}{\dfrac{1}{w_q}P + 1} \end{cases} \quad \text{(IV. 22)}$$

where w_d and w_q are the cut-off frequencies to be optimized, the coefficients $\alpha_{d,q}$ are selected close to the reversed rated inductances d, q, respectively, that are $\alpha_d = \frac{1}{L_d}$ and $\alpha_q = \frac{1}{L_q}$.

The discrete version of (IV.18) can be obtained using Euler approximation as follows:

$$\begin{cases} I_{d|k+1} = \hat{f}_{d|k} T_s + \alpha_d V_{d|k} T_s + I_{d|k} \\ I_{q|k+1} = \hat{f}_{q|k} T_s + \alpha_q V_{q|k} T_s + I_{q|k} \end{cases} \quad \text{(IV. 23)}$$

where $I_{d,q|k}$ and $V_{d,q|k}$ are the d, q currents and input voltage respectively, T_s stands for the sampling time.

***Assumption 1*:** The estimated values of $\hat{f}_d(t)$ and $\hat{f}_q(t)$ are considered bounded such that: $\left|\hat{f}_d(t)\right| \leq \Delta_d$ and $\left|\hat{f}_q(t)\right| \leq \Delta_q$, where Δ_d and Δ_q are the upper boundaries of $\hat{f}_d(t)$ and $\hat{f}_q(t)$ respectively.

Remark 2: The inclusion of derivative terms in TDE equations has led to high fluctuations in the estimated values of $\hat{f}_d$ and $\hat{f}_q$, as shown in equation (IV.21). In order to address this issue, a Low Pass Filter (LPS) has been incorporated in the TDE output to reduce the ripple effect.

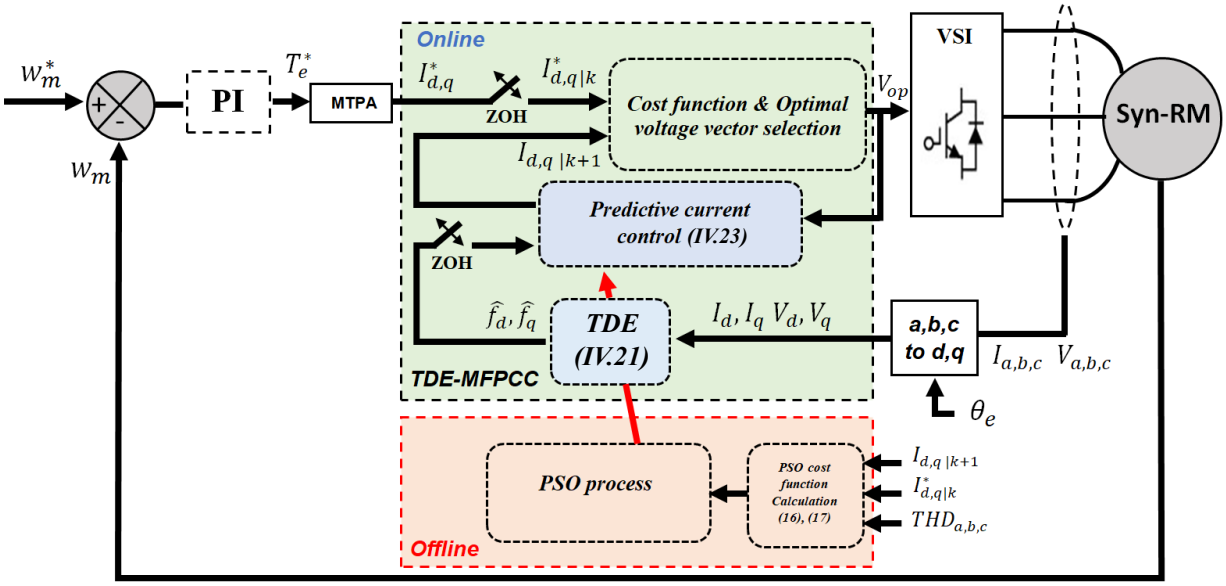

Figure IV-3: TDE-MFPCC schematic control block.

IV.4.3 Optimization of the TDE-MFPCC using Particle Swarm Algorithm (PSO)

In the proposed control scheme, the coefficients $\beta_{d,q}$ and LPS cut-off frequencies $w_{d,q}$ are optimized with a PSO algorithm, which is a computational technique for optimizing a particular problem by iteratively attempting to improve a candidate solution in relation to a specified quality measure. In the process of PSO, it begins by selecting a random set of unknown parameter values, with each set representing a particle swarm. The goal function corresponding to each particle is computed using each position and velocity of the current particle. Then, the particle whose objective value matches to the optimal value is picked and recorded after each iteration of the algorithm, and ultimately the global best solution is generated [97]. The PSO process flowchart is depicted in **Figure IV-4.**

Fig (IV.5)

$\beta_{d,q}$ used in (IV.21) are defined through the PSO algorithm process based on minimization of the cost function G_β :

$$\begin{cases} Find\ X = (\beta_d, \beta_q) \\ G_\beta = \text{ To minimize } {}_{obj}(X) = min\left[\left(I^*_{d|k} - I_{d|k+1}\right) + \left(I^*_{d|k} - I_{d|k+1}\right)\right] \end{cases} \quad \text{(IV. 24)}$$

The Total Harmonic Distortion (THD) of the three-phase currents (a, b, c) measurement is minimized to achieve optimal settings $w_{d,q}$ according to the cost function G_w defined as:

$$\begin{cases} Find\ X = (w_d, w_q) \\ G_w = \text{ To minimize } {}_{obj}(X) = min[THD_a + THD_b + THD_b] \end{cases} \quad \text{(IV. 25)}$$

The swarm particle velocity $vi(t\ +\ 1)$ is updated using the last best global solution p_g as stated in the following:

$$v_i(t+1) = wv_i(t) + c_1 r_1\left(p_i - x_i(t)\right) + c_2 r_2\left(p_g - x_i(t)\right) \quad \text{(IV. 26)}$$

where w is the inertia weight, c_1 and c_2 represent the cognition learning and the social learning factors, respectively, and $r_1, r_2 \in [0,1]$ are generated random numbers, p_g is the current best global position, whilst p_i denotes the local best position of the current PSO iteration. The new position is then updated as follows:

$$x_i(t+1) = x_i(t) + v_i(t+1) \quad \text{(IV. 27)}$$

The pseudo-code written in Algorithm.1 represents a brief description of the PSO process used for parameters optimization through 100 iterations of 10 swarm particle candidates.

Remark 3: There are many optimization techniques in the literature to achieve an optimum solution for a given problem. In this thesis a PSO algorithm is chosen, with a few iterations. The algorithm is able to provide good results in such optimization issues.

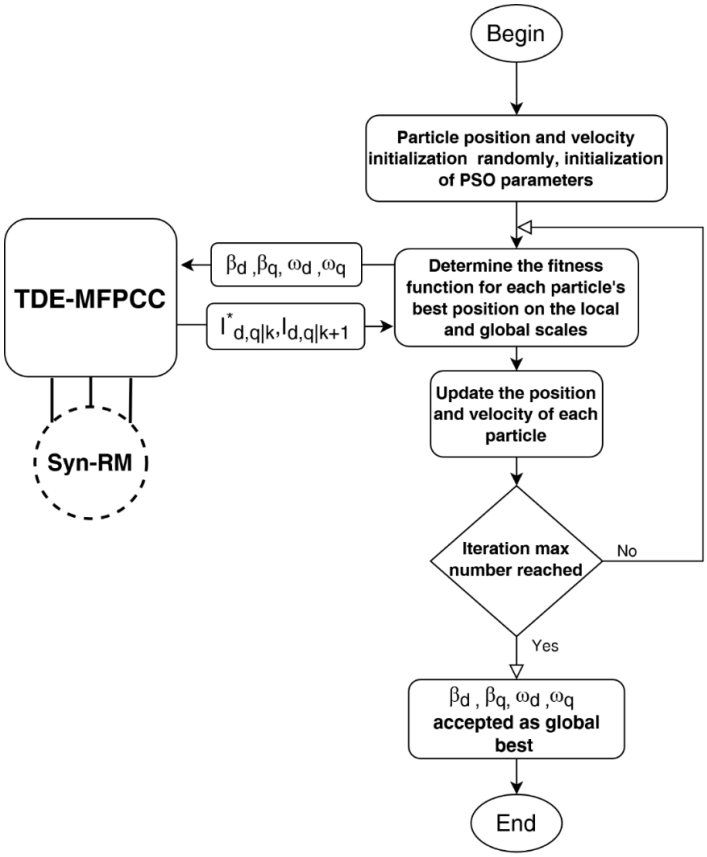

Figure IV-4: Flowchart of particle swarm optimization algorithm.

Algorithm 1: Pseudo-code of the PSO algorithm

Cost function G_n for **n** $\in \{\boldsymbol{\beta_d}, \boldsymbol{\beta_q}, \boldsymbol{w_d}, \boldsymbol{w_q}\}$

Swarm initialization: the position $\boldsymbol{x_i(t)}$ and velocity $\boldsymbol{v_i(t)}$ are initialized randomly

for $\boldsymbol{t} \leftarrow \mathbf{1}$ to 100 (Iteration number)

for $\boldsymbol{i} \leftarrow \mathbf{1}$ to 10 (Swarm size)

Evaluate and update the local best $\boldsymbol{G_n(p_i(t))}$ based on the result of (IV.26) and (IV.27)

if $\boldsymbol{G_n(x_i(t)) < G_n(p_i(t))}$ **then**

update the best position $\boldsymbol{p_i(t)}$, that is $\boldsymbol{p_i(t) = x_i(t)}$

end if

end for

$\boldsymbol{G_n(p_g(t)) = \min_i(G_n(p_i(t)))}$

Evaluate and update the global best $\boldsymbol{G_n(p_g(t))}$ after each swarm iteration update

---

particle velocity $v_i(t+1)$ using (IV.24)

update particle position $x_i(t+1)$ using (IV.25)

end for

Rank the solutions and find the global best of $\beta_{d,q}$ and $w_{d,q}$.

IV.5 Simulation and discussion

The simulation of the proposed control was conducted in Matlab/Simulink, where a non-linear model of Syn-RM was implemented in the overall scheme, with nominal parameters presented in Table A-1 in Appendix. The sample time is set to 0.00005 s as well as the delay time used in TDE estimation equation (IV.21). For a fair comparison between the proposed method and the conventional MB-PCC, the same PI speed controller parameters were tuned for both strategies, in order to simulate the effect of parameters mismatch on Syn-RM PCC control. Both L_d and L_q are set to 50 % of their rated values. The results of the last iteration of PSO process is presented in **Figure A-1** and **Figure A-2** in appendix for $\beta_{d,q}$ and $w_{d,q}$ employed in (IV.21),(IV.22) respectively, containing the local best value of each swarm (small blue stars) and the globally optimal solution (big orange stars) .

IV.5.1 Load change burden

Figures IV.5 , IV.6 and **IV.7** show the simulated response of the conventional MB-PCC and TDE-MFPCC, where the same operation scenarios were applied. At first, the load was set to 10 N.m and the speed to the rated value of 1500 rpm. Then, at t=2 s the load steps to the rated value 14 N.m. The results of MB-PCC with accurate motor parameters are illustrated in **Figure IV-5**. The first graph shows the speed response and its reference value, and in the second graph phase (A) current is presented. The third graph shows the obtained response of $I_{d,q}$ and their references $I_{d,q}^{*}$. It can be clearly seen that MB-PCC in **Figure IV-5** provides good performance when accurate motor parameters are taken into account in the control. **Figure IV-6** depicts the responses obtained using MB-PCC with mismatched model parameters, where increased current THD and deviation are observed as the current response deviates more from the target signal as the load increases. The results of the suggested TDE-MFPCC are depicted in **Figure IV-7.** In contrast to the MB-PCC, the proposed

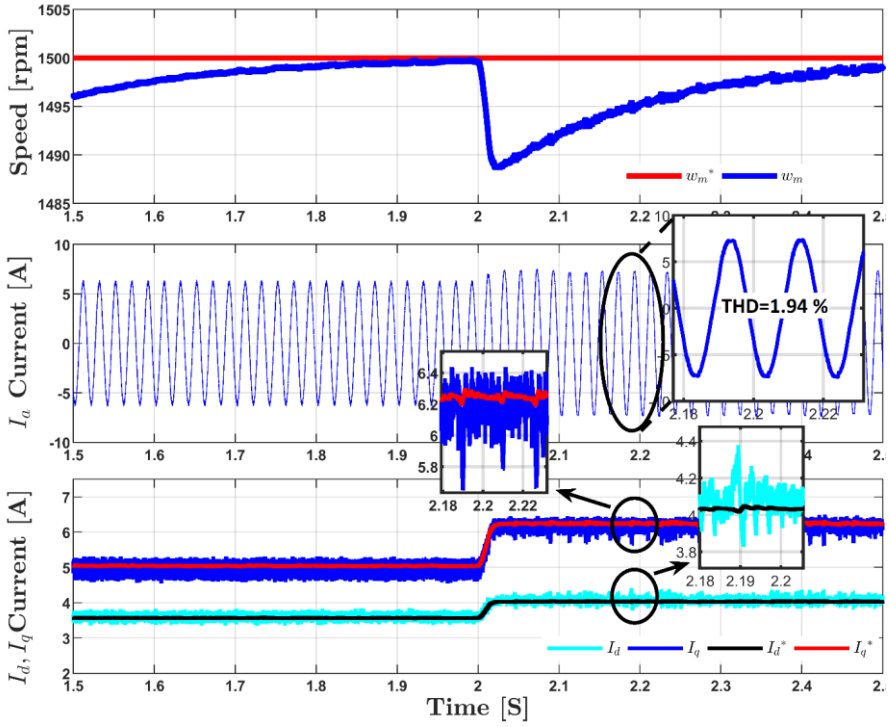

Figure IV-5: Simulation results under a load change: (a) conventional MB-PCC with accurate parameters.

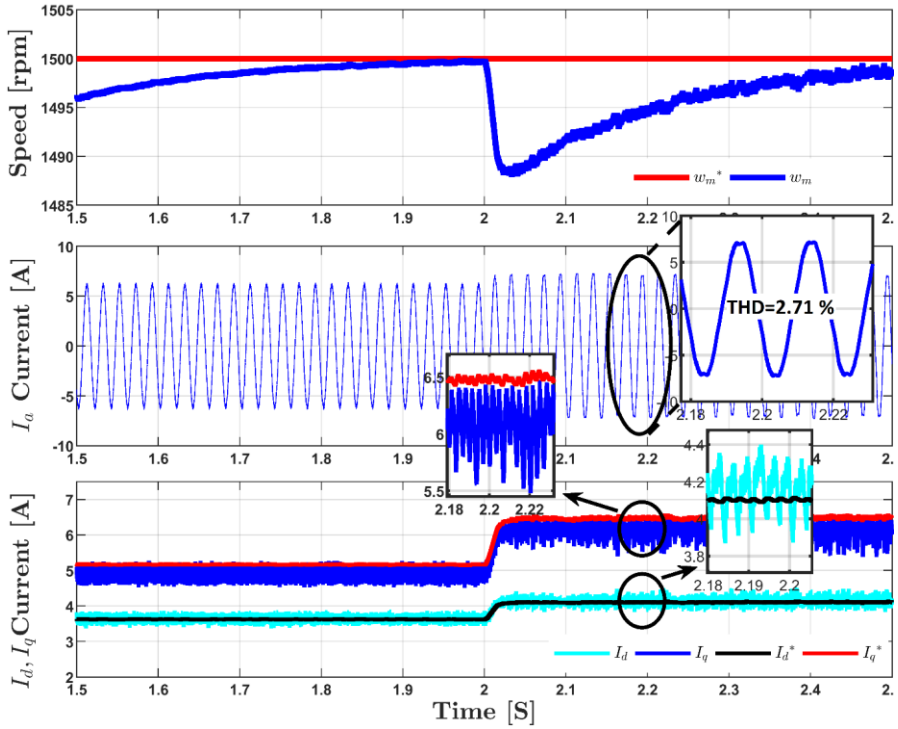

Figure IV-6: Simulation results under a load change for conventional MB-PCC with mismatched parameters.

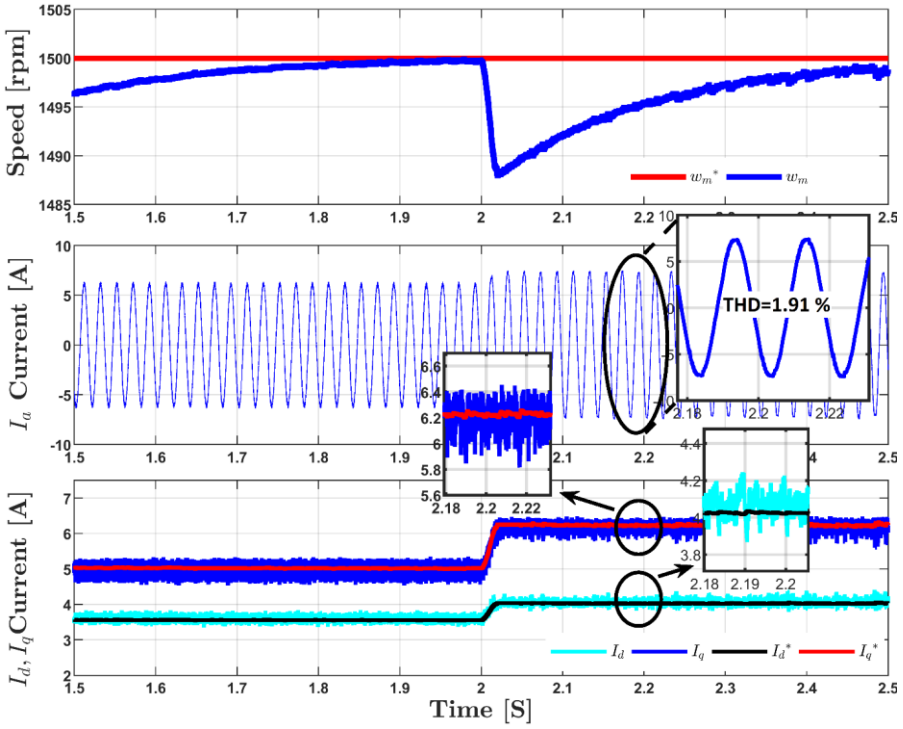

Figure IV-7: Simulation results under a load change for the proposed TDE-MFPCC.

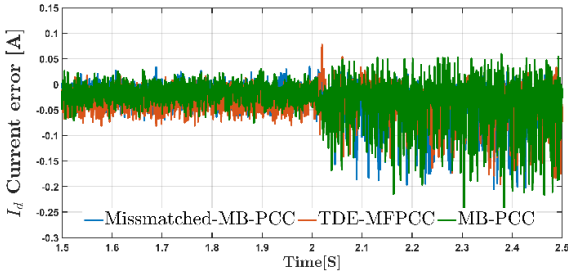

Figure IV-8: I_d current tracking error under a load change.

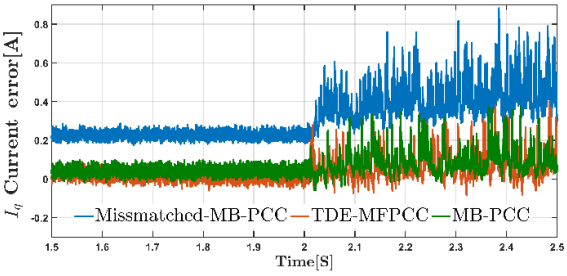

Figure IV-9: I_q current tracking error under a load change.

scheme has better steady-state performance and less THD. The lumped uncertainties estimate $\widehat{f_d}$ and $\widehat{f_q}$ response is shown in **Figure A-1** in Appendix, where steady-state performance is achieved owing to the system dynamic behavior reflected by the TDE technique.

Figure IV-8 and **Figure IV-9** depict the current tracking errors for I_d and I_q of the presented control schemes when the Syn-RM is under the effect of load torque. It is clear also that the parameter mismatch has a significant effect on the current control. Besides, in the MB-PCC with accurate parameters and the proposed TDE-MFPCC, the tracking errors were reduced significantly in the load change case. To further highlight the robustness of the proposed control scheme

compared to the other control approaches, the graph of the tracking errors of I_d and I_q according to the multivariate load torque have been also shown in **Figure IV-10** and **Figure IV-11**. It can be seen that when using MB-PCC with mismatched parameters, the I_q error increases proportionally with load variation. The proposed TDE-MFPCC reduces the gap between the current reference and its actual value, in a similar way to the MB-PCC with accurate parameters.

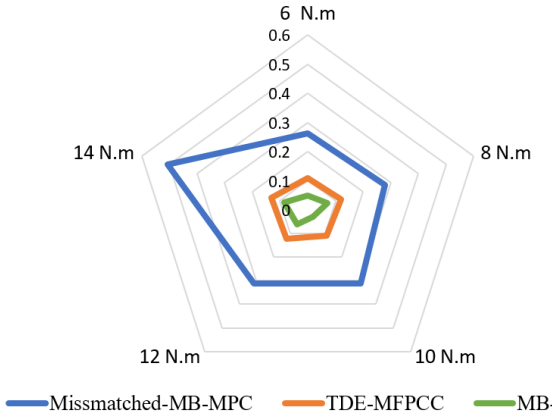

Figure IV-10: I_d current tracking error as a function of load torque.

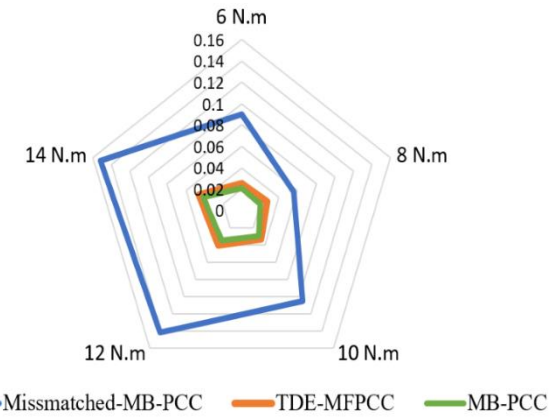

Figure IV-11: I_q current tracking error as a function of load torque.

IV.5.2 Speed variation burden

Figure IV-12, IV.13 and **IV.14** show the simulation results of the aforementioned control methods for a speed variation test. At first, the load value is set to 10 N.m, and the speed value is set to 800 rpm. Then, at t=1.8 s the load value steps to the rated value of 1500 rpm. The obtained results, shown in **Figure IV-12,** indicate that the parameters mismatch has also a considerable effect on conventional MB-PCC under a speed variation scenario. **Figure IV-14** shows that the I_q tracking error proportionally increases with the speed from t=1.8 s, while TDE-MFPCC is less affected by a speed change (see **Figures IV.15** and **IV.16**) with a slight increase of I_q tracking error. From the point of view of THD, the current distortion was reduced thanks to the disturbance compensation feature provided by the TDE technique. In **Figure IV-13** the MB-PCC Phase (A) response shows the burden caused by inaccurate parameters which led to high THD value compared with TDE-MFPCC, where phase (A) THD was lower as well as in the case MB-PCC with exact parameters shown in **Figure IV-12** For further analysis of the presented TDE-MFPCC, the lumped uncertainties estimates $\widehat{f_d}$ and $\widehat{f_q}$ response is depicted in **Figure A-2** in Appendix. Here,

one can observe the change in estimated dynamics that occurs in conjunction with the variation in speed. It is seen that parameter mismatch has a significant effect on the current control as the load increases. On the contrary, the MB-PCC with accurate parameters has less current. In sum up the obtained results within the simulation tests, compared issues of the three presented schemes MB-PCC and TDE-MFPCC were illustrated in **Table IV-1.**

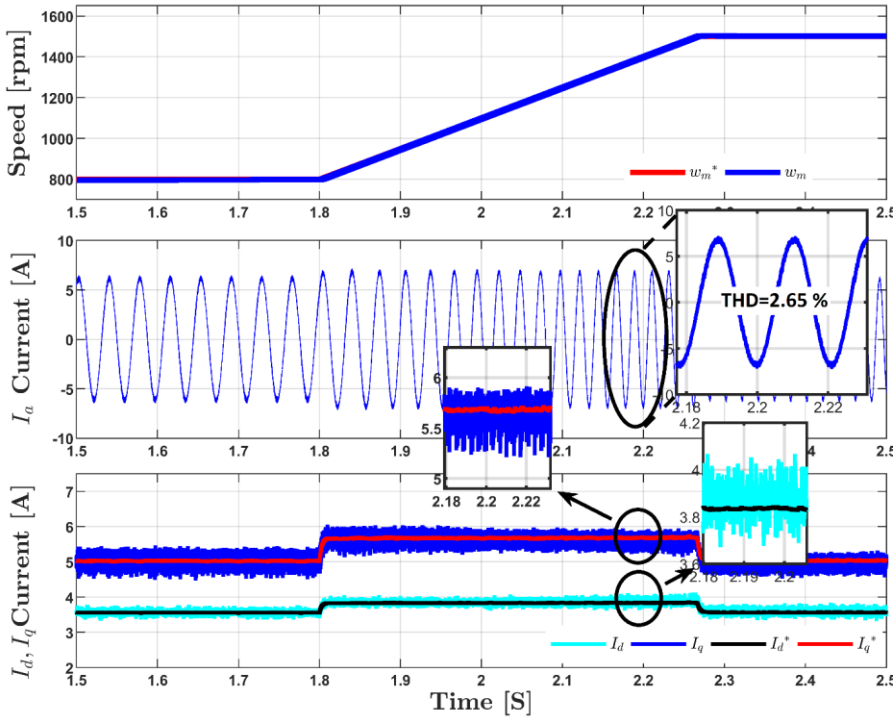

Figure IV-12: Simulation results under speed change for conventional MB-PCC with accurate parameters.

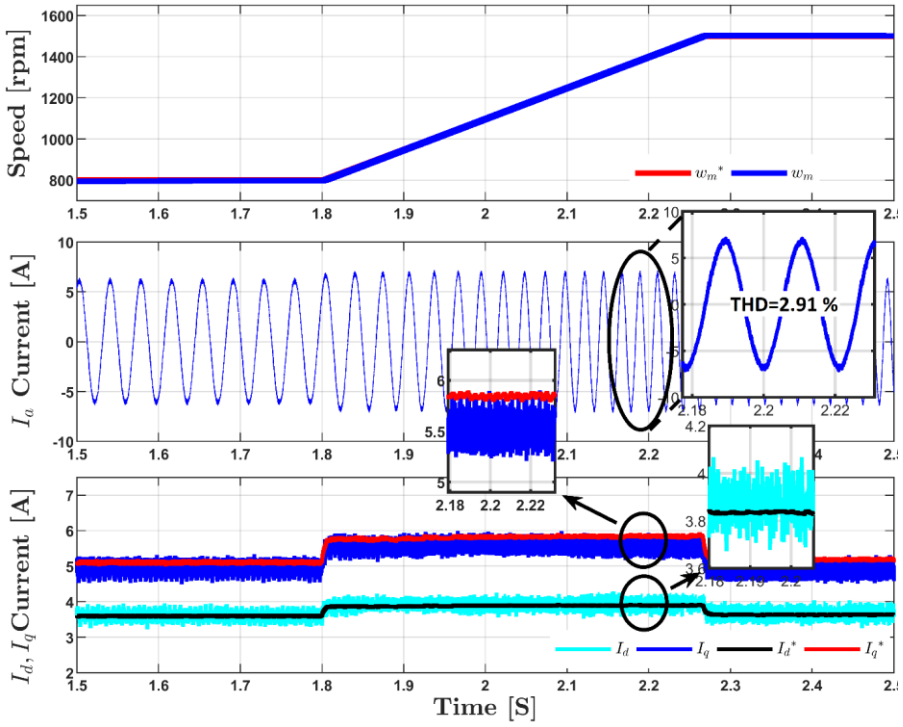

Figure IV-13:Simulation results under speed change for conventional MB-PCC with mismatched parameters.

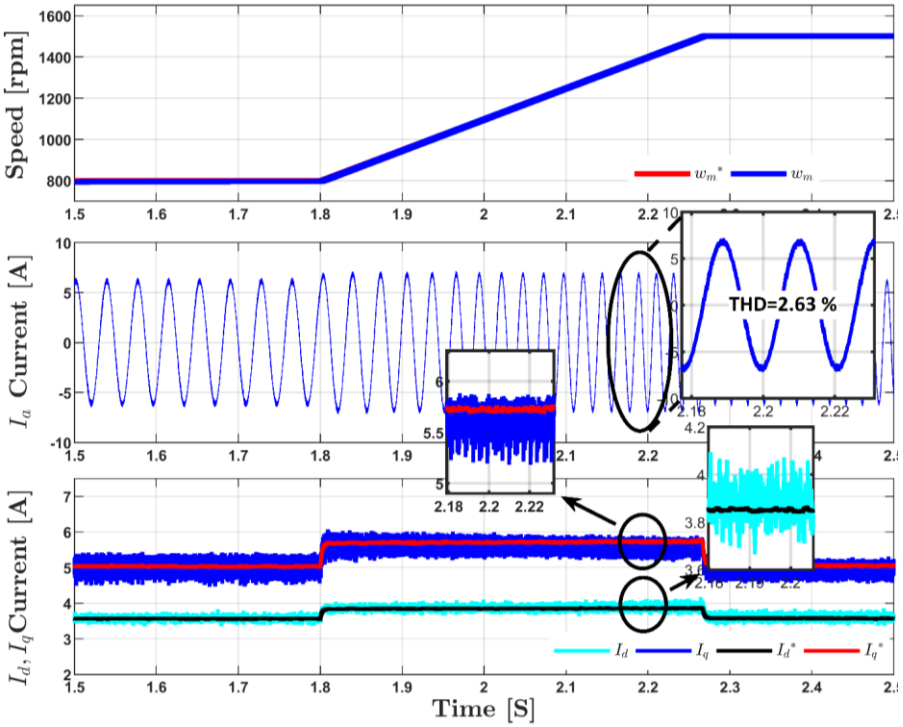

Figure IV-14: Simulation results under speed change for the proposed TDE- MFPCC.

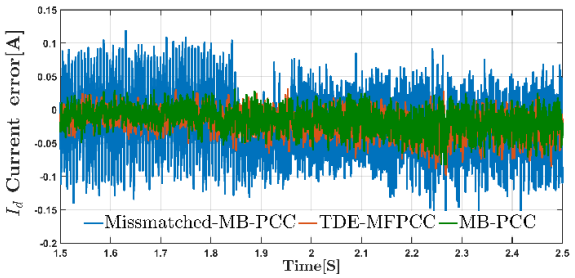

Figure IV-15: I_d current tracking error under a speed change.

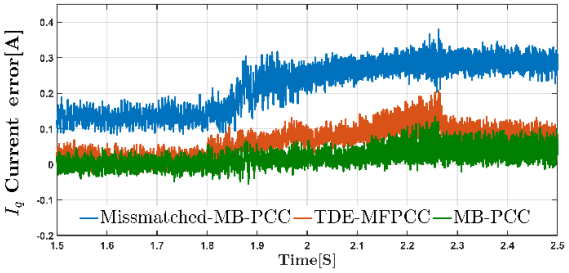

Figure IV-16: I_q current tracking error under a speed change.

Syn-RM PCC scheme	Computation time	Motor parameters needed	Algorithm complexity	Tuned Parameters
Conventional MB-PCC	$27.5\mu s$	R_s, L_d, L_q	Low	Null
Proposed TDE-MFPCC	$26.0\mu s$	Null	Low	$\beta_{d,q}, w_{d,q}$

Table IV-1: Comparative issues.

IV.6 Conclusion

In this Chapter a new optimal model-free predictive control approach for Syn-RM drive based on a time-delay estimation (TDE) technique has been proposed. By combining the model-free control theory and the TDE approximator, this proposed control system is able to deal with uncertainties and disturbance problems. Furthermore, it allows to give a robust and straightforward control that can be implemented in real-time applications. By introducing a particle swarm optimization (PSO) metaheuristic algorithm, the control design parameters were optimized to improve the electrical dynamic performances of the Syn-RM system. To give more simplicity, the speed control is made by the conventional proportional-integral controller in the outer loop. The proposed TDE-based model-free predictive current control (TDE-MFPCC) is employed in the inner loop to effectively stabilize the internal dynamics of the Syn-RM. Extensive numerical results have been presented to illustrate the best performance of the proposed control algorithm in comparison with the conventional model-based predictive controller. The simulation results have proven that MF-PCC can effectively address the drawbacks resulting from Syn-RM parameter variations when compared to MB-PCC .

GENERAL CONCLUSION

General conclusion

In this thesis, a literature review, theoretical analysis, and simulation-based study of Synchronous Reluctance Machines (Syn-RM) have been presented. Regarding the control performance optimization was obtained by using Enhanced Direct Torque Control (DTC) and Model-Free Predictive Current Control (MF-PCC). A speed sensorless control was elaborated as well as a simple Extended Kalman Filter (EKF) algorithm.

Chapter I begins by providing an overview about the Syn-RM and its different structures, followed by a review of control strategies. The speed sensorless schemes were briefly summarized, then providing a characteristic analysis by mentioning the pros and cons of each estimation technique. After recalling these techniques, the Extended Kalman Filter (EKF) is chosen for two reasons, firstly EKF is capable of providing real-time speed estimation, secondly it has a simple algorithm implementation compared to other nonlinear estimation techniques.

In Chapter II, the concept of reluctant torque and the electrical and mechanical models of the Syn-RM in the reference frames (a,b,c), (α,β), and (d,q) were recalled. The model that neglects the rotor currents was considered for this thesis. Subsequently, three control strategies, namely DTC, FOC, and DTC-SVM, were presented for comparison. Simulation results have demonstrated the benefits offered by DTC-SVM compared with the two other techniques, with optimized control performance and significantly reduced torque ripple.

A fully sensorless control simulation was presented in Chapter III, where the non-linear version of a Kalman Filter (EKF) was incorporated into the DTC-SVM technique. The discrete full order model of Syn-RM was introduced and written as an extended case of conventional Kalman Filter. Additionally, the observability study confirmed that only the speed parameter can be estimated from the current quantities i_d and i_q provided that these currents are not null. After, three simulation scenarios have been conducted on the given model of Syn-RM, regarding the disturbance rejection, transition to high speed, and sinusoidal setpoint tracking. It is obvious from the obtained results that the EKF estimation technique can be suitable for Syn-RM speed control where no rotor position sensor is needed for coordinates transformation from a, b, c to d, q.

Chapter IV proposed a Model-Free Predictive Current Control (MF-PCC) to deal with Syn-RM system uncertainties. Generally, in most control systems of Syn-RM, controllers are parameter-

dependent, and their performance relies on the knowledge of motor parameters. The fundamental conception of a model free control law was explained, followed by the basic design of the conventional Model Based Predictive Current Control (MB-PCC) .Subsequently, the elaboration of MF-PCC was detailed, by using a simple lumped uncertainties technique called Time Delay Estimation (TDE) . The obtained simulation results of the proposed control scheme represent an adequate performance of the MFC control algorithm compared to thr MB-PCC with mismatched Syn-RM parameters, since the MF-PCC does not depend on the system's parameters. Its tracking performance is more acceptable during load or speed operating point variation.

In conclusion, this thesis has achieved the main objective of finding a high-performance nonlinear control of Syn-RM. It gives an exhaustive description of Syn-RM dynamic model and the control strategies through simulation upon the given model. The sensorless mode control is studied as well and closed loop speed estimation was confirmed with a fully non-linear model of Syn-RM . Finally, this thesis has included a novel model-free control method based on TDE approach using only input and output signals of the Syn-RM system. As the last contribution, the MFC potentials pointed out in this dissertation should stimulate further exploration and study on this type of controller to achieve the familiarity required to transfer the results to practical applications.

The prospects arising from this work should be further explored and investigated in the future to achieve even greater efficiencies. These points, in particular, include:

- For the sake of optimizing sensorless control scheme, the EKF can be incorporated with other estimation techniques where the zero speed (standstill) estimation is possible.
- Regarding the intrinsic independence of the proposed MFC from any information about the model of the studied system, the presented MFC method could be used for different electrical AC drives such as Induction Machine (IM), Permanent Magnet Synchronous Machine (PMSM), Switched Reluctance Machine (SRM), etc.

Appendix

Rated power	2.2 kW
Rated current	5.7 A
Rated speed	1500 rpm
Rated Torque	14 N.m
N° of pole pairs	2
Moment of inertia (J)	0.0137 Kg.m/s
Stator resistance	1.71 Ω

Table A-1: Syn-RM parameters

i_d (A)	L_d (H)
0,21	0,235
0,39	0,246
0,60	0,251
0,79	0,252
0,99	0,252
1,49	0,249
1,98	0,244
2,51	0,236
3,02	0,225
3,51	0,211
4,03	0,196
4,52	0,182
4,98	0,170
5,45	0,159

i_q (A)	L_q (H)
0,39	0,142
0,62	0,112
0,80	0,098
1,06	0,084
1,52	0,069
1,98	0,061
2,53	0,054
2,98	0,050
3,57	0,046
4,03	0,044
4,55	0,042
5,06	0,041
5,58	0,039
6,09	0,038

Table A-2: Syn-RM L_d , L_q parameters.

Parameters	Value
Proportional gain K_P	0.2
Integral gain K_I	0.8
D-axis inductance L_d	0.26H
Q-axis Inductance L_q	0.057H
α_d	4.1
α_q	17.5
β_d	2.6
β_q	22.1
ω_d	167.3rad/s
ω_q	153.8rad/s
PSO swarm set number	10
PSO iteration number	100
Sampling time T_s	$50\mu s$

Table A-3: Simulation settings.

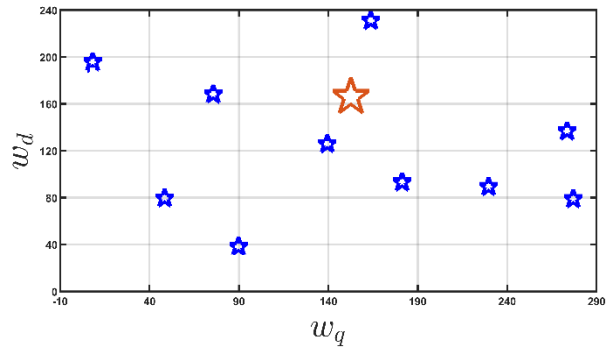

Figure A-1: Last iteration of PSO swarms in the process of $\beta_{d,q}$

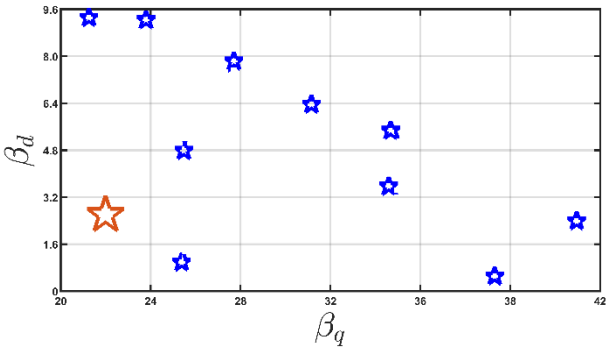

Figure 0-2: Last iteration of PSO swarms in the process of $w_{d,q}$

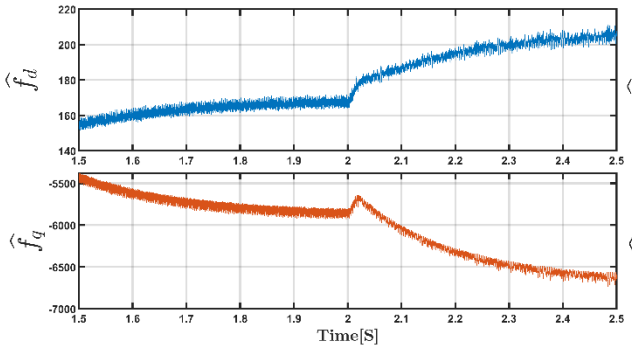

Figure A-3: Estimated lumped uncertainties$\hat{f}_d$ and $\hat{f}_q$ during a load change.

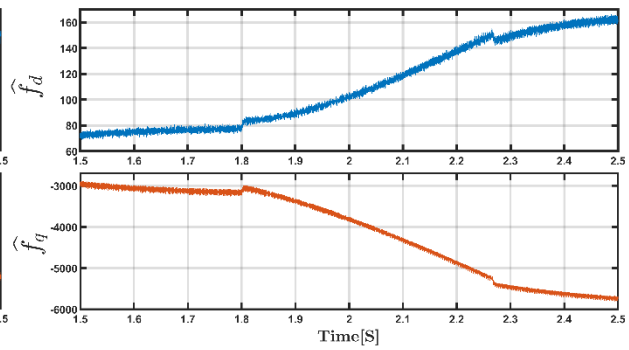

Figure A-4: Estimated lumped uncertainties $\hat{f}_d$ and $\hat{f}_q$ during a load change.

References

[1] Mohand Ouramdane Hamiti, “Réduction des ondulations de couple d’une machine synchrone à réluctance variable : Approches par la structure et par la commande.” *Doctoral dissertation, Nancy I University , France , 2009*

[2] P. J. Lawrenson, J. M. Stephenson, N. N. Fulton, P. T. Blenkinsop, and J. Corda, “Variable-speed switched reluctance motors,” *IEE Proc. B Electr. Power Appl. UK, vol. 127, no. 4, p. 253, 1980.*

[3] I. Boldea, Z. X. Fu, and S. A. Nasar, “Performance evaluation of axially-laminated anisotropic (ALA) rotor reluctance synchronous motors,” in *Conference Record of the 1992 IEEE Industry Applications Society Annual Meeting, Houston, TX, USA: IEEE,pp. 212–218,1992.*

[4] D. A. Staton, T. J. E. Miller, and S. E. Wood, “Maximising the saliency ratio of the synchronous reluctance motor,” *IEE Proc. B Electr. Power Appl. UK*, *vol. 140, no. 4, p. 249, 1993.*

[5] Tsaarady Raminosoa, “Optimisation des performances des machines synchro reluctantes par reseaux de permeances”, *Doctoral dissertation, National Polytechnique Institute of Lorraine, France. 2006.*

[6] K.-J. Joo, I.-G. Kim, J. Lee, and S.-C. Go, “Robust speed sensorless control to estimated error for PMa-SynRM,” *IEEE Trans. Magn.*, *vol. 53, no. 6, pp. 1–4, Jun. 2017*.

[7] P. Sarkar and S. Srinivas, “MTPA based DTC for permanent magnet assisted synchronous reluctance motor for electric vehicle application,” *IEEE Transportation Electrification Conference and Expo, Asia-Pacific (ITEC Asia-Pacific), Seogwipo-si, Korea (South): IEEE, pp. 1–6, May.2019.*

[8] S. Morimoto, M. Sanada, and Y. Takeda, “Performance of PM-assisted synchronous reluctance motor for high-efficiency and wide constant-power operation,” *IEEE Trans. on Ind. Appl., vol. 37, no. 5, pp. 1234–1240, Oct. 2001.*

[9] B. Kerdsup, N. Takorabet, and B. Nahidmobarakeh, “Design of permanent magnet-assisted synchronous reluctance motors with maximum efficiency-power factor and torque per cost,” *XIII International Conference on Electrical Machines (ICEM), Alexandroupoli: IEEE, , pp. 2465–2471, Sep. 2018.*

[10] T. M. Jahns and V. Caliskan, “Uncontrolled generator operation of interior PM synchronous machines following high-speed inverter shutdown,” *IEEE Trans. on Ind. Appl.*, vol. 35, no. 6, pp. 1347–1357*, Dec. 1999*.

[11] P. Niazi, H. A. Toliyat, and A. Goodarzi, “Robust maximum torque per ampere (MTPA) control of PM-assisted SynRM for traction applications,” *IEEE Trans. Veh. Tech.*, *vol. 56, no. 4, pp. 1538–1545, Jul. 2007*.

[12] Jeihoon Baek, M. M. Rahimian, and H. A. Toliyat, “Optimal design of PM assisted synchronous reluctance generators using lumped parameter model and Differential Evolution Strategy,” in *2009 IEEE Energy Conversion Congress and Exposition*, *San Jose, CA: IEEE, pp. 2453–2459, Sep. 2009.*

[13] T. J. E. Miller, "Switched reluctance motors and their control″. in *Monographs in electrical and electronic engineering, no. 31. Hillsboro, OH : Oxford: Magna Physics Pub. ; Clarendon Press, 1993.*

[14] T. J. E. Miller, Ed., "Electronic control of switched reluctance machines". *in Newnes power engineering series. Oxford ; Boston: Newnes, 2001.*
[15] P. Lawrenson, "Switched-reluctance motor drives," *Elec. Power UK*, *vol. 29, no. 2, p. 144, 1983.*
[16] R. E. Betz, R. Lagerquist, M. Jovanovic, T. J. E. Miller, and R. H. Middleton, "Control of synchronous reluctance machines," *IEEE Trans. on Ind. Appl.*, *vol. 29, no. 6, pp. 1110–1122, Dec. 1993.*
[17] T. Lubin, "Modélisation et commande de la machine synchrone à réluctance variable, Prise en compte de la saturation magnétique," *Doctoral dissertation, University of Henri Poincaré, Nancy, France, 2003*.
[18] X.T.Garcia,B.Zigmund,A.Terlizzi,R.Pavlanin and L.Salvatore, "Comparision between FOC and DTC strategy for PMSM," *Adv. in electron. and elec. eng.*, vol. *vol.5, pp. 1–2, Jun. 2006.*
[19] D. Casadei, F. Profumo, G. Serra, and A. Tani, "FOC and DTC: two viable schemes for induction motors torque control," *IEEE Trans. Power Electron.*, *vol. 17, no. 5, pp. 779–787, Sep. 2002.*
[20] Xudong Wang, Risha Na, and Ning Liu, "Simulation of PMSM field-oriented control based on SVPWM," in *2009 IEEE Vehicle Power and Propulsion Conference*, *Dearborn, MI: IEEE, pp. 1465–1469, Sep. 2009.*
[21] S. Bolognani, L. Peretti, and M. Zigliotto, "Online MTPA control strategy for DTC synchronous-reluctance-motor drives," *IEEE Trans. Power Electron.*, *vol. 26, no. 1, pp. 20–28, Jan. 2011.*
[22] V. K. Arun Shankar, S. Umashankar, S. Paramasivam, P. Sanjeevikumar, and K. Venkatesh, "Investigation of direct torque control-based synchronous reluctance motor drive for pumping," in *Advances in Systems, Control and Automation, Springer Singapore vol. 442, pp. 319–327, 2018.*
[23] A. Ammar, A. Bourek, and A. Benakcha, "Nonlinear SVM-DTC for induction motor drive using input-output feedback linearization and high order sliding mode control," *ISA Transactions, vol. 67, pp. 428–442, Mar. 2017.*
[24] A. Ammar, A. Benakcha, and A. Bourek, "Closed loop torque SVM-DTC of induction motor drive with efficiency optimization," *4th European Conference on Renewable Energy Systems , ECRES'16, Istanbul, Turkey, 28-31 August 2016*.
[25] T. Liu, H. S. Haslim, and S. Tseng, "Predictive controller design for a high-frequency injection sensorless synchronous reluctance drive system," *IET Electric Power Applications*, *vol. 11, no. 5, pp. 902–910, May. 2017*.
[26] W. Benjamim, I. Jlassi, and A. J. M. Cardoso, "A Computationally efficient model predictive current control of synchronous reluctance motors based on hysteresis comparators," *Electronics*, *vol. 11, no. 3, p. 379, Jan. 2022.*
[27] N. Aros, V. Mora, and C. Alarcon, "Model predictive control for synchronous reluctance motor drive," in *2017 CHILEAN Conference on Electrical, Electronics Engineering, Information and Communication Technologies (CHILECON)*, *Pucon, Chili : IEEE, pp. 1–6, Oct. 2017.*
[28] A. Yousefi-Talouki, P. Pescetto, and G. Pellegrino, "Sensorless direct flux vector control of synchronous reluctance motors including standstill, MTPA, and flux weakening," *IEEE Trans. on Ind. Appl.*, *vol. 53, no. 4, pp. 3598–3608, Jul. 2017.*
[29] S. Ichikawa, M. Tomita, S. Doki, and S. Okuma, "Sensorless control of synchronous reluctance motors based on extended EMF models considering magnetic saturation with

online parameter identification," *IEEE Trans. on Ind. Appl.*, *vol. 42, no. 5, pp. 1264–1274, Sep. 2006.*
[30] S. Ichikawa, M. Tomita, S. Doki, and S. Okuma, "Sensorless control of synchronous reluctance motors based on extended electromotive force model and inductance measurement," *Elect. Eng. Jpn.*, *vol. 160, no. 4, pp. 70–80, Sep. 2007.*
[31] S. Ichikawa, Zhiqian Chen, M. Tomita, S. Doki, and S. Okuma, "Sensorless control of an interior permanent magnet synchronous motor on the rotating coordinate using an extended electromotive force," in *IECON'01. 27th Annual Conference of the IEEE Industrial Electronics Society (Cat. No.37243)*, *Denver, CO, USA: IEEE, pp. 1667–1672, 2001.*
[32] S.-C. Agarlita, I. Boldea, and F. Blaabjerg, "High-frequency-injection-assisted 'active-flux'-based sensorless vector control of reluctance synchronous motors, with experiments from zero speed," *IEEE Trans. on Ind. Appl.*, *vol. 48, no. 6, pp. 1931–1939, Nov. 2012.*
[33] A. Yousefi-Talouki, P. Pescetto, G. Pellegrino, and I. Boldea, "Combined active flux and high-frequency injection methods for sensorless direct-flux vector control of synchronous reluctance machines," *IEEE Trans. Power Electron.*, *vol. 33, no. 3, pp. 2447–2457, Mar. 2018.*
[34] L. Ortombina, D. Pasqualotto, F. Tinazzi, and M. Zigliotto, "Comprehensive analysis and design of a pulsating signal injection-based position observer for sensorless synchronous motor drives," *IEEE J. Emerg. Sel. Topics Power Electron.*, *vol. 10, no. 2, pp. 1925–1934, Apr. 2022.*
[35] M. Bugsch, A. Held, and B. Piepenbreier, "Sensorless control of SynRMs using an adaptive 2DoF current control including a comparison of two alternating HF signal injection-based methods," in *IECON 2016 - 42nd Annual Conference of the IEEE Industrial Electronics Society*, *Florence, Italy: IEEE, pp. 2910–2916, Oct. 2016.*
[36] P. Pescetto and G. Pellegrino, "Automatic tuning for sensorless commissioning of synchronous reluctance machines augmented with high-frequency voltage injection," *IEEE Trans. on Ind. Appl.*, *vol. 54, no. 5, pp. 4485–4493, Sep. 2018.*
[37] A. Consoli, G. Scarcella, G. Scelba, A. Testa, and D. A. Triolo, "Sensorless rotor position estimation in synchronous reluctance motors exploiting a flux deviation approach," *IEEE Trans. on Ind. Appl.*, *vol. 43, no. 5, pp. 1266–1273, 2007.*
[38] M. Moujahed, B. Touaiti, H. Benazza, M. Jemli, and M. Boussak, "Extended Kalman filter for sensorless fault tolerant control of pmsm with stator resistance estimation," *IJPEDS*, *vol. 9, no. 2, p. 579, Jun. 2018.*
[39] Z. Mynar, P. Vaclavek, and P. Blaha, "Synchronous reluctance motor parameter and state estimation using extended kalman filter and current derivative measurement," *IEEE Trans. Ind. Electron.*, *vol. 68, no. 3, pp. 1972–1981, Mar. 2021.*
[40] Risfendra, Y.-S. Kung, and L.-C. Huang, "Design and digital hardware implementation of a sensorless controller for PMSM drives using LF signal injection and EKF," in *2017 International Conference on Applied System Innovation (ICASI*), *Sapporo, Japan: IEEE, pp. 1281–1284, May. 2017.*
[41] T. Shi, Z. Wang, and C. Xia, "Speed measurement error suppression for pmsm control system using self-adaption Kalman observer," *IEEE Trans. Ind. Electron.*, *vol. 62, no. 5, pp. 2753–2763, May. 2015.*
[42] D. Pasqualotto, S. Rigon, and M. Zigliotto, "Sensorless speed control of synchronous reluctance motor drives based on extended Kalman filter and neural magnetic model," *IEEE Trans. Ind. Electron.*, *vol. 70, no. 2, pp. 1321–1330, Feb. 2023.*

[43] F. Gao, Z. Yin, C. Bai, D. Yuan, and J. Liu, "Speed sensorless control method of synchronous reluctance motor based on resonant Kalman filter," *IEEE Trans. Ind. Electron.*, *vol. 70, no. 8, pp. 7627–7641, Aug. 2023.*

[44] M. Schroedl and P. Weinmeier, "Sensorless control of reluctance machines at arbitrary operating conditions including standstill," *IEEE Trans. Power Electron.*, *vol. 9, no. 2, pp. 225–231, Mar. 1994.*

[45] E. Capecchi, P. Guglielmi, M. Pastorelli, and A. Vagati, "Position-sensorless control of the transverse-laminated synchronous reluctance motor," *IEEE Trans. on Ind. Appl.*, *vol. 37, no. 6, pp. 1768–1776, Nov. 2001.*

[46] A. Consoli, F. Russo, G. Scarcella, and A. Testa, "Low and zero speed sensorless control of synchronous reluctance motors," in *Conference Record of 1998 IEEE Industry Applications Conference. Thirty-Third IAS Annual Meeting (Cat. No.98CH36242)*, *St. Louis, MO, USA: IEEE, pp. 685–692,1998.*

[47] H. W. De Kock, M. J. Kamper, and R. M. Kennel, "Anisotropy comparison of reluctance and PM synchronous machines for position sensorless control using HF carrier injection," *IEEE Trans. Power Electron.*, *vol. 24, no. 8, pp. 1905–1913, Aug. 2009.*

[48] Z. Wang, Q. Guo, J. Xiao, T. Liang, Z. Lin, and W. Chen, "High-frequency square wave injection sensorless control method of IPMSM based on oversampling scheme," *WEVJ*, *vol. 13, no. 11, p. 217, Nov. 2022.*

[49] A.M. Darkawi, "Etude, développement et mise en œuvre de deux observateurs de position pour la commande sans capteurs de la Machine Synchrone à Aimants Permanents (MSAP)," *Mémoire Diplôme des Etudes Supérieures Approfondies (DESA), Universite Cadi Ayyad Marrakech, Maroc, 2007.*

[50] F. P. Scalcon, C. J. Volpato, T. Lazzari, T. S. Gabbi, R. P. Vieira, and H. A. Grundling, "Sensorless Control of a SynRM Drive Based on a Luenberger Observer with an Extended EMF Model," in *IECON 2019 - 45th Annual Conference of the IEEE Industrial Electronics Society*, *Lisbon, Portugal: IEEE, pp. 1333–1338, Oct. 2019.*

[51] Y. Zhang and X.-F. Cheng, "Sensorless control of permanent magnet synchronous motors and EKF parameter tuning research," *Mathematical Problems in Engineering*, *vol. 2016, pp. 1–12, 2016.*

[52] A. Qiu, Bin Wu, and H. Kojori, "Sensorless control of permanent magnet synchronous motor using extended Kalman filter," in *Canadian Conference on Electrical and Computer Engineering 2004 (IEEE Cat. No.04CH37513)*, *Niagara Falls, Ont., Canada: IEEE, pp. 1557–1562, 2004.*

[53] Z. Zheng, Y. Li, and M. Fadel, "Sensorless control of PMSM based on extended kalman filter," in *2007 European Conference on Power Electronics and Applications*, *Aalborg, Denmark: IEEE, , pp. 1–8,2007.*

[54] H. Yang, R. Yang, W. Hu, and Z. Huang, "FPGA-based sensorless speed control of pmsm using enhanced performance controller based on the reduced-order EKF," *IEEE J. Emerg. Sel. Topics Power Electron.*, *vol. 9, no. 1, pp. 289–301, Feb. 2021.*

[55] T. Senjyu, K. Kinjo, N. Urasaki, and K. Uezato, "Sensorless control of synchronous reluctance motors considering the stator iron loss with extended Kalman filter," in *IEEE 34th Annual Conference on Power Electronics Specialist, 2003. PESC '03*, *Acapulco, Mexico: IEEE, pp. 403–408, 2003.*

[56] Y. Shi, K. Sun, L. Huang, and Y. Li, "Online identification of permanent magnet flux based on extended Kalman filter for IPMSM drive with position sensorless control," *IEEE Trans. Ind. Electron., vol. 59, no. 11, pp. 4169–4178, Nov. 2012.*

[57] S. Bolognani, L. Tubiana, and M. Zigliotto, "Extended kalman filter tuning in sensorless PMSM drives," *IEEE Trans. on Ind. Applicat.*, *vol. 39, no. 6, pp. 1741–1747, Nov. 2003.*

[58] Csaba Szabo, "Motor Revolution: Synchronous reluctance motor technology," *Electrical Engineering Institutions Lecture Program ,ABB Australia, Jul. 2014.*

[59] M. Correvon, "Cours Systèmes électromécanique*". lecture, Haute Ecole d'Ingénierie et de Gestion Du canton de Vaud Available: https://www.chireux.fr/mp/cours/electromecanique/Chap03%20%20Systemes%20electrodynamiques.pdf , visited on June .2023*

[60] R. R. Moghaddam, "Synchronous reluctance machine (SynRM) design". *Master Thesis, Royal Institute of Technology, Stockholm, Sweden, 2007.*

[61] T. Matsuo and T. A. Lipo, "Rotor position detection scheme for synchronous reluctance motor based on current measurements," *IEEE Trans. on Ind. Applicat*, *vol. 31, no. 4, pp. 860–868, Aug. 1995.*

[62] T. Hamiti, T. Lubin, L. Baghli, and A. Rezzoug, "Modeling of a synchronous reluctance machine accounting for space harmonics in view of torque ripple minimization," *Mathematics and Computers in Simulation*, *vol. 81, no. 2, pp. 354–366, Oct. 2010.*

[63] T. Lubin, "Modélisation et commande de la machine synchrone à réluctance variable: prise en compte de la saturation magnétique" *Doctoral Dissertation, Nancy university, France ,2003*

[64] K. Yahia, D. Matos, J. O. Estima, and A. J. M. Cardoso, "Modeling synchronous reluctance motors including saturation, iron losses and mechanical losses," in *2014 International Symposium on Power Electronics, Electrical Drives, Automation and Motion*, *Ischia, Italy: IEEE, pp. 601–606, Jun. 2014.*

[65] H. A. Zarchi, R. Arab Markadeh, and J. Soltani, "Direct torque control of synchronous reluctance motor using feedback linearization including saturation and iron losses," *EPE Journal*, *vol. 19, no. 3, pp. 50–62, Sep. 2009.*

[66] M. F. Rahman and S. K. Dwivedi, "Modeling, simulation and control of electrical drives".

[67] J. Holtz, "Pulsewidth modulation-a survey," *IEEE Trans. Ind. Electron.*, *vol. 39, no. 5, pp. 410–420, Oct. 1992.*

[68] D. Ishak, Z. Q. Zhu, and D. Howe, "Comparison of PM brushless motors, having either all teeth or alternate teeth wound," *IEEE Trans. Energy Convers.*, *vol. 21, no. 1, pp. 95–103, Mar. 2006.*

[69] A. M. EL-Refaie, "Fractional-slot concentrated-windings synchronous permanent magnet machines: opportunities and challenges," *IEEE Trans. Ind. Electron.*, *vol. 57, no. 1, pp. 107–121, Jan. 2010.*

[70] X. Zhang, G. H. B. Foo, and M. F. Rahman, "A robust field-weakening approach for direct torque and flux controlled reluctance synchronous motors with extended constant power speed region," *IEEE Trans. Ind. Electron.*, *vol. 67, no. 3, pp. 1813–1823, Mar. 2020.*

[71] H. Wu, D. Depernet, V. Lanfranchi, K. E. K. Benkara, and M. A. H. Rasid, "A novel and simple torque ripple minimization method of synchronous reluctance machine based on torque function method," *IEEE Trans. Ind. Electron.*, *vol. 68, no. 1, pp. 92–102, Jan. 2021.*

[72] G. H. B. Foo and X. Zhang, "Robust direct torque control of synchronous reluctance motor drives in the field-weakening region," *IEEE Trans. Power Electron.*, *vol. 32, no. 2, pp. 1289–1298, Feb. 2017.*
[73] F. Boudjema, "Commande par mode de glissement : Application aux convertisseurs électriques," *Doctoral Dissertation, Toulouse university, France, 1991.*
[74] J. Haataja, "A comparative performance study of four-pole induction motors and synchronous reluctance motors in variable speed drives," *Doctoral Dissertation, Lappeenranta University of Technology, Finland, 2003.*
[75] M. Ghanes, "Observation et commande de la machine asynchrone sans capteur mécanique," *Doctoral Dissertation, Nantes university , France, 2005.*
[76] Z. Zheng, "Commande à haute performance et sans capteur mécanique du moteur synchrone à aimants permanents," *Doctoral Dissertation*, *Toulouse National Polytechnique institut, France, 2008.*
[77] G. Welsh. G. Bishop, "An introduction to the Kalman filter," *Lecture, Chapel Hill: Department of Computer Science, University of North Carolina, USA, pp. 1–16, 2006.*
[78] M. L. Jayaramu, H. N. Suresh, M. S. Bhaskar, D. Almakhles, S. Padmanaban, and U. Subramaniam, "Real-time implementation of extended kalman filter observer with improved speed estimation for sensorless control," *IEEE Access*, *vol. 9, pp. 50452–50465, 2021.*
[79] A. Khemis R., T. Boutabba, and S. Drid, "Discrete time sensorless PMSM control using an extended Kalman filter for electric vehicle traction systems fed by multi level inverter," in *Artificial Intelligence and Renewables Towards an Energy Transition*, *vol. 174, pp. 281–293, 2021.*
[80] P. Cortes, M. P. Kazmierkowski, R. M. Kennel, D. E. Quevedo, and J. Rodriguez, "Predictive control in power electronics and drives," *IEEE Trans. Ind. Electron.*, *vol. 55, no. 12, pp. 4312–4324, Dec. 2008.*
[81] Y. Zhang, J. Jin, and L. Huang, "Model-free predictive current control of PMSM drives based on extended state observer using ultralocal model," *IEEE Trans. Ind. Electron.*, *vol. 68, no. 2, pp. 993–1003, Feb. 2021.*
[82] L. Xu, G. Chen, and Q. Li, "Ultra-local model-free predictive current control based on nonlinear disturbance compensation for permanent magnet synchronous motor," *IEEE Access*, *vol. 8, pp. 127690–127699, 2020.*
[83] C. A. Agustin, J.-T. Yu, C.-K. Lin, J. Jai, and Y.-S. Lai, "Triple-voltage-vector model-free predictive current control for four-switch three-phase inverter-fed SPMSM based on discrete-space-vector modulation," *IEEE Access*, *vol. 9, pp. 60352–60363, 2021.*
[84] R. E. Skelton, "Model error concepts in control design," *International Journal of Control*, *vol. 49, no. 5, pp. 1725–1753, May .1989.*
[85] W.-H. Chen, "Disturbance observer based control for nonlinear systems," *IEEE/ASME Trans. Mechatron.*, *vol. 9, no. 4, pp. 706–710, Dec. 2004.*
[86] J. Yang, W.-H. Chen, S. Li, L. Guo, and Y. Yan, "Disturbance/uncertainty estimation and attenuation techniques in PMSM drives—a survey," *IEEE Trans. Ind. Electron.*, *vol. 64, no. 4, pp. 3273–3285, Apr. 2017.*
[87] HongZhe Jin and JangMyung Lee, "An RMRAC current regulator for permanent-magnet synchronous motor based on statistical model interpretation," *IEEE Trans. Ind. Electron.*, *vol. 56, no. 1, pp. 169–177, Jan. 2009.*

[88] R. Errouissi, M. Ouhrouche, W.-H. Chen, and A. M. Trzynadlowski, "Robust cascaded nonlinear predictive control of a permanent magnet synchronous motor with antiwindup compensator," *IEEE Trans. Ind. Electron.*, *vol. 59, no. 8, pp. 3078–3088, Aug. 2012.*

[89] S.-H. Chang, P.-Y. Chen, Y.-H. Ting, and S.-W. Hung, "Robust current control-based sliding mode control with simple uncertainties estimation in permanent magnet synchronous motor drive systems," *IET Electr. Power Appl.*, *vol. 4, no. 6, p. 441, 2010.*

[90] Y. Guo, B. Tang, J. Gong, and T. Su, "Research on speed control system of PMSM based on active disturbance rejection control," in *2020 7th International Conference on Information Science and Control Engineering (ICISCE)*, *Changsha, China: IEEE, pp. 2141–2145, Dec. 2020.*

[91] M. S. Rahmat, F. Ahmad, A. K. Mat Yamin, V. R. Aparow, and N. Tamaldin, "Modeling and torque tracking control of permanent magnet synchronous motor (PMSM) for hybrid electric vehicle," *Int J Automot Mech Eng*, *vol. 7, pp. 955–967, Jun. 2013.*

[92] M. Fliess and C. Join, "Model-free control," *International Journal of Control*, *vol. 86, no. 12, pp. 2228–2252, Dec. 2013.*

[93] M. Bröcker and L. Herrmann, "Flatness based control and tracking control based on nonlinearity measures," *IFAC-PapersOnLine*, *vol. 50, no. 1, pp. 8250–8255, Jul. 2017.*

[94] Songklod SRIPRANG, "High-performance nonlinear control for permanent magnet assisted synchronous reluctance motor," *Doctoral Dissertation, Lorraine University, Nancy, France, 2021.*

[95] H. Mesai Ahmed, I. Jlassi, A. J. Marques Cardoso, and A. Bentaallah, "Model-free predictive current control of synchronous reluctance motors based on a recurrent neural network," *IEEE Trans. Ind. Electron.*, *vol. 69, no. 11, pp. 10984–10992, Nov. 2022.*

[96] J. Riccio, P. Karamanakos, S. Odhano, M. Tang, M. D. Nardo, and P. Zanchetta, "Direct model predictive control of synchronous reluctance motor drives," *IEEE Trans. on Ind. Applicat.*, *vol. 59, no. 1, pp. 1054–1063, Jan. 2023.*

[97] G. I. Y. Mustafa, H. P. Wang, and Y. Tian, "Vibration control of an active vehicle suspension systems using optimized model-free fuzzy logic controller based on time delay estimation," *Advances in Engineering Software*, *vol. 127, pp. 141–149, Jan. 2019.*

[98] Birame M'hamed " Commande sans capteur de vitesse d'un moteur a reluctance variable par l'utilisation des techniques de l'intelligence artificielle" *Doctoral Dissertation , Mohamed Lakhdher University , Batna , Algeria , Oct .2015 .*

PUBLICATIONS AND COMMUNICATIONS

1. Publications:

[1] Boussouar M. E, Chelihi A, Yahia K, Cardoso A. J. M. "Model-free predictive current control of Syn-RM based on time delay estimation approach";. *Journal of Electrical Engineering, vol. 74, no.5, pp.344-356, Oct. 2023.*
https://doi.org/10.2478/jee-2023-0042

[2] Boussouar M. E, Yahia K, Cardoso A. J. M., Sahraoui M. "Enhanced Direct Torque Control of a Syn-RM, Using Adaptive Flux Observer, Including Magnetic Saturation and Iron Losses"; *Przeglad Elektrotechniczny, vol.44, no 4, pp.255-261, Apr .2023*

https://doi.org/10.15199/48.2023.04.44

2. Communications:

[1] Boussouar M. E, Yahia K, Cardoso A. J. M., Sahraoui M, "Comparative Study of Synchronous Reluctance Motor (SynRM) Control Strategies", in *International Conference on Advances in Communication Technology, Computing and Engineering*, ICACTCE'2021, *Morocco, March 24-26, 2021.*

Journal of Electrical Engineering, Vol. 74, No. 5, 2023, pp. 344-356

sciendo

PAPERS

Model-free predictive current control of Syn-RM based on time delay estimation approach

Mohamed Essalih Boussouar[1, 4], Abdelghani Chelihi[2, 3], Khaled Yahia[4, 5], Antonio J. Marques Cardoso [4]

This paper investigates an optimal model-free control design for a synchronous reluctance motor (Syn-RM) with unknown nonlinear dynamic functions, parameter variations, and disturbances. The idea is to combine a predictive control with a time-delay estimation technique (TDE) in order to successfully deal with the system's uncertainties and make the Syn-RM control scheme easy to implement in real-time. This model-free control strategy comprises two cascade control loops namely outer and inner loops. The outer loop is designed for the mechanical part of Syn-RM to ensure the convergence of the speed dynamics by using a proportional-integral controller while the inner loop is developed to control the uncertain dynamics of currents via an optimal robust controller. In the proposed current loop, the predictive control is enhanced by the inclusion of ultra-local model theory where dynamic functions and disturbances are estimated by instantaneous input-output measurements of the Syn-RM using the TDE approach. Moreover, a particle swarm optimization (PSO) algorithm is also proposed to find the optimal design parameters to improve the dynamic performances of the closed-loop control system. Numerical validation tests of the proposed TDE-based model-free predictive current control (TDE-MFPCC) method are performed in the simulation environment of the Syn-RM system, and the results show the robustness and the effectiveness of the proposed TDE-MFPCC compared to the conventional model-based PCC.

Keywords: synchronous reluctance motor (Syn-RM), model-free control, predictive current control, time-delay estimation.

1 Introduction

The synchronous reluctance motor (Syn-RM) is an alternating current motor that operates on the principle of reluctance torque, as opposed to conventional induction motors that rely on the principle of rotor current induction to generate torque [1]. Syn-RM uses the magnetic reluctance of the rotor to generate torque resulting in increased efficiency, power factor, and dynamic performance [2, 3]. The Syn-RM machine also has a higher starting torque than the traditional induction motor making it excellent for applications requiring high starting torque [4]. Recent advancements in rotor design and high-complexity embedded systems have made this motor an attractive option for various applications [5]. In addition, its sturdy design is further enhanced by a wingless and magnetless rotor.

The promising potential of the control engineering of Syn-RM machines has led to the attraction of many researchers to this field of study. Field-oriented control (FOC) is a widely used technique for regulating the torque and flux of a Syn-RM [6, 7]. By utilizing stator current vectors, FOC allows for precise control of the motor's performance. There are two modes in which FOC can be implemented. The first is direct field-oriented control, which involves directly orienting the current vectors with their corresponding controllers [8]. The second mode is indirect field-oriented control, which includes additional torque and flux control loops to indirectly regulate the current vectors [9]. Direct torque control (DTC) also is a classical method used in AC drives, including Syn-RM, that offers advantages over FOC in terms of response time [10, 11]. DTC enables quick responses to changes in speed and load, making it a preferred approach for torque and flux control [12]. However, the major disadvantage of this approach is the occurrence of high ripples in both flux and electromagnetic torque [13-16]. To overcome the shortcomings of traditional classical methods, the advanced control technique of model predictive control (MPC) has been utilized to drive the Syn-RM machine. MPC approach has gained popularity among researchers for its straightforward design, remarkable dynamic performance, and ease of application [17-22].

The MPC approach has the ability to predict the controlled variables, such as current, torque, and flux, in the subsequent time step before implementing the corresponding control actions. In literature, model

[1] Laboratoire de Modélisation des Systèmes Énergétiques, LMSE. University of Biskra, Biskra, Algeria
[2] Department of Electrical Engineering, LI3CUB Laboratory, University of Biskra, Biskra, Algeria
[3] Department of Electronics, Faculty of Technology, Contantine 1 University, Constantine, Algeria
[4] CISE – Electromechatronic Systems Research Centre, University of Beira Interior, Covilhã, Portugal
[5] Laboratoire de Génie Energétique et Matériaux, LGEM, University of Biskra, Biskra, Algeria
mohamedessalih.boussouar@univ-biskra.dz

https://doi.org/10.2478/jee-2023-0042, Print (till 2015) ISSN 1335-3632, On-line ISSN 1339-309X

1. Mohamed Essalih BOUSSOUAR[1], 2. Khaled YAHIA[1], 3. A.J.M CARDOSO[2], 4. Mohamed SAHRAOUI[1]
University of Mohamed Khaidar, Biskra, Algeria (1), University of Beira Interior, Covilhã, Portugal (2)

doi:10.15199/48.2023.04.44

Enhanced Direct Torque Control of a Syn-RM, Using Adaptive Flux Observer, Including Magnetic Saturation and Iron Losses

Abstract. *An enhanced direct torque control (E-DTC) system of a synchronous reluctance motor (Syn-RM) is presented in this paper. The motor system is modelled by taking into account its non-linear behaviours such as iron losses and magnetic saturation. The proposed method consists of incorporating hysteresis DTC with a model reference adaptive system (MRAS) flux observer. This technique is applied in order to achieve good torque and flux ripples reduction, which ensure a smooth operation of the Syn-RM along all the speed range. Furthermore, the proposed method has simple design and implementation in the overall control system, and can avoid the drawbacks of conventional flux estimators. Simulation results show the effectiveness of the proposed method.*

Streszczenie. *W artykule przedstawiono udoskonalony układ bezpośredniego sterowania momentem obrotowym (E-DTC) synchronicznego silnika reluktancyjnego (Syn-RM). Układ ruchu jest modelowany z uwzględnieniem jego nieliniowych zachowań, takich jak straty żelaza i nasycenie magnetyczne. Proponowana metoda polega na włączeniu histerezy DTC do wzorcowego obserwatora strumienia adaptacyjnego systemu odniesienia (MRAS). Technika ta jest stosowana w celu uzyskania dobrego momentu obrotowego i redukcji tętnień strumienia, które zapewniają płynną pracę Syn-RM w całym zakresie prędkości. Ponadto, zaproponowany sposób ma prostą konstrukcję i implementację w całym systemie sterowania i pozwala uniknąć wad konwencjonalnych estymatorów strumienia. Wyniki symulacji pokazują skuteczność proponowanej metody..(**Ulepszona bezpośrednia kontrola momentu obrotowego Syn-RM, wykorzystująca adaptacyjnego obserwatora strumienia, w tym nasycenie magnetyczne i straty żelaza*)

Keywords: Direct torque control (DTC), Flux estimation, Torque Ripple
Słowa kluczowe: Bezpośrednia kontrola momentu obrotowego , szacowanie strumienia, tętnienie momentu obrotowego

1. Introduction

In recent years, the synchronous reluctance motor (Syn-RM) has attracted the attention of many researchers all over the world. Syn-RM is considered as a very promising motor for future applications because of its high-power density, superior reliability, due to its simple rotor structure, and outstanding efficiency, especially in torque control applications.

Accurate representation of Syn-RM requires detailed knowledge of the magnetic behaviour in both d and q axes along with cross-saturation at different operating conditions. The iron loss is introduced in the Syn-RM
model by adding a shunt resistor in both d and q equivalent circuits. The magnetic saturation is introduced in the motor model using experimentally obtained inductance values in both d and q axes [1].

With the evolution of power electronics and drive systems, the control of such motor has become a big challenge. Advanced field-oriented control has been employed in Syn-RM [2, 3]. Maximum Torque Per Ampere (MTPA) and Flux Weakening (FW) operation modes for Syn-RM have been also proposed [4, 5]. Similar research is dedicated to PM assisted Syn-RM, using estimated load torque [6]. This technique may involve high computational capacity requirements for digital signal processing. In another approach, vector control is applied on PM-assisted Syn-RM parameter uncertain model, by incorporating backstepping current controller [7]. Despite the focus of many researches on the vector control of the synchronous reluctance drive, such motor sufferers from high torque and flux ripples in steady state operation [8, 9]. Direct Torque Control (DTC) is known as one of the most conventional control strategies used for the induction motor (IM) and permanent magnet synchronous motor (PMSM) [10, 11], but rarely used for Syn-RM because of unsatisfying torque and flux response when used in its classic form. An improved duty cycle control method to minimize torque and flux ripples of conventional DTC on IM was then proposed [12].

As it is known, DTC requires instantaneous quantities of the torque and flux that are compared to their reference values within the DTC loop. An improved DTC strategy for a five-phase Interior Permanent Magnet Synchronous Motor (IPMSM) based on a fuzzy controller is also presented in the literature [13]. This control features a simplicity of implementation, but it suffers from sensitivity to parameters variation, such as stator resistance and/or iron losses. Minimization of the torque ripple in induction and permanent magnet synchronous motors have been widely studied, but few investigations have been conducted on Syn-RM. In this regard, feedback linearization was combined with neuron-fuzzy control for IM torque ripple reduction [14]. Predictive control can be a good alternative for PMSM torque control, and a new Predictive Torque Control (PTC) was proposed to determine the optimal voltage switching states, which ensures less torque and flux ripples [15]. Similar research has been dedicated to PMSM where adaptive learning control was incorporated with an adaptive proportional controller (PI)[16]. The major cons of the later strategy is the important computational capacity requirement and implementation complexity. Optimal current calculation is used, including inductance harmonics [17, 18]. By optimization of the motor design, a combination of asymmetrical poles and shifted pole pairs of Syn-RM has been proposed [19] to have less torque ripple compared to the conventional design. Also, an asymmetrical stator is designed for a ferrite-assisted Syn-RM by shifting the slot opening from the center [20]. The optimization of the flux barrier geometry through the Syn-RM rotor is one of the design solutions for torque ripple reduction where asymmetrical barriers were proposed [21]. A current third-harmonic injection-based technique was also proposed [22], but m = 3 phase number machines are excluded from this research, because the torque produced from the current third-harmonic has a zero-average value. In order to have a fast response of Syn-RM operation, the optimal point of flux reference using MTPA has been investigated [23].
DTC-SVM is employed to achieve extended operation conditions from the point of view of torque and speed, and new MTPA and FW control laws were proposed, but torque ripple reduction was not included [24]. In order to compensate the torque harmonics, an optimal current reference is calculated based on the torque function [25]. This later technique offers simple implementation and less computational complexity.

ICACTCE'21
MOROCCO

INTERNATIONAL CONFERENCE ON ADVANCES IN COMMUNICATION TECHNOLOGY, COMPUTING AND ENGINEERING (ICACTCE 2021)

Certificate of Participation

We hereby certify that:

Mohamed Essalih Boussouar

University of Biskra, Algeria

Has participated and presented a paper entitled:

Comparative Study of Synchronous Reluctance Motor (SynRM) Control Strategies

Authored by: Mohamed Essalih Boussouar, Khaled Yahia, Antonio J. Marques Cardoso, Mohamed Sahraoui

During the International Conference on Advances in Communication Technology, Computing and Engineering (ICACTCE'21), which was held virtually from Morocco on March 24-26, 2021.

Dr. Mariya Ouaissa
General Chair

Dr. Zakaria Boulouard
General Co-Chair